THE ENGINEERING OF RADIOLUMINESCENT NANOPARTICLES AS THERAPEUTIC AGENTS FOR MULTIMODAL CANCER TREATMENT

by

Vincenzo J. Pizzuti

A Thesis

Submitted to the Faculty of Purdue University

In Partial Fulfillment of the Requirements for the degree of

Master of Science in Chemical Engineering

Davidson School of Chemical Engineering

West Lafayette, Indiana

August 2019

THE PURDUE UNIVERSITY GRADUATE SCHOOL
STATEMENT OF COMMITTEE APPROVAL

Dr. You-Yeon Won, Chair

Davidson School of Chemical Engineering

Dr. Chongli Yuan

Davidson School of Chemical Engineering

Dr. Bennet D. Elzey

Department of Comparative Pathobiology

Approved by:

Dr. Sangtae Kim

Head of the Graduate Program

To my family and friends, especially Mom, Dad, Antonio, and Bo for their love and support.

ACKNOWLEDGMENTS

In the process of conducting my dissertation research and in writing this thesis, I have been very fortunate to receive significant support and assistance from a number of people. First, I would like to thank my thesis advisor, Dr. Won, for lending his time and expertise in helping to devise research topics and to advise me in fine-tuning the approaches and analyses taken to complete the proposed research projects. I also want to thank him for the time taken to help proofread and edit the manuscripts detailing our work, and for his guidance in writing this thesis.

I would also like to extend my sincere thanks to many colleagues that helped me along the course of completing this work. I want to thank Rahul and Kyle for their instrumental role in helping me to get started with graduate level research and for their friendship, and thanks to Jaewon for taking the time to train me. I also want to thank Joe, Hansol, Kaustabh, and Dhushyanth for all of their assistance on several experiments and in helping to make my time working here at Purdue enjoyable. A great deal of gratitude is also owed to my collaborators Sandra, Mel, and Dr. Elzey for their extensive efforts in helping me to conduct animal experiments and for their advice and guidance along the way. Thank you also to Drs. Langer, Long, and Durm for their mentoring and guidance, and the same thanks is owed to Drs. Rancilio and Childress for their vital role in collaboration for the canine clinical trial and their advice to me.

I also want to thank my family, particularly my mom, dad, and brother for their willingness to listen and their counsel along the way. Thank you for your unwavering support. Lastly, thank you to my friends, who served as an excellent sounding board for ideas and troubleshooting, and for their readiness to distract me when resting from work.

TABLE OF CONTENTS

LIST OF TABLES

LIST OF FIGURES

ABSTRACT

Author: Pizzuti, Vincenzo J. MSCHE
Institution: Purdue University
Degree Received: August 2019
Title: The Engineering of Radioluminescent Nanoparticles as Therapeutic Agents for Multimodal Cancer Treatment
Committee Chair: You-Yeon Won, Ph.D.

Under the guidance of cancer treatment data, this thesis emphasizes the development of radiation-responsive nanomaterials for the effective implementation of localized, multimodal therapy for solid tumors. Evidence from decades of treatment outcomes underscores the benefits provided by employing multiple therapeutic agents in concert to improve prognoses for cancer patients. As a pillar of standard care in oncology, radiation therapy (RT) is a particularly appropriate choice as a component of combination therapies, acting as a localized tool for achieving long-term tumor control. By combing primary RT with radio-sensitizing, polymer-encapsulated formulations of crystalline calcium tungstate nanoparticles (CWO NPs), this work has shown significant improvements in efficacy in *in vitro* and murine xenograft models of primary human head and neck tumors as well as in spontaneous sarcoma in a clinical case study. Under X-ray radiation, CWO NPs emit long-wavelength ultraviolet (UV-A) and visible light, a property referred to as radioluminescence. This work focuses on utilizing these properties in combination with encapsulant functionalization strategies to further improve therapeutic outcomes through specific mechanistic enhancements.

Ordinarily used primarily to improve biocompatibility and colloidal stability, the polymeric materials used to encapsulate the CWO NPs were tailored to serve distinct functions in the overall combination therapy scheme. Approaches explored in this work include surface functionalization of these polymers with a cancer-specific ligand, folic acid, and the incorporation of photo-responsive/sensitizing bilirubin-polymer conjugates as an encapsulant. The predicted outcomes of surface functionalization and photo-active encapsulation were confirmed to significantly enhance radiotherapy efficacy. Finally, exploration of intratumoral NP distribution after dose administration was conducted to preliminarily evaluate strategies for dose homogeneity improvement. Mechanical agitation of the injection site somewhat improves distribution of NPs in tumor xenografts but requires future exploration for improved understanding and implementation.

1. INTRODUCTION

1.1 Motivation for the Enhancement of Radiation Therapy

Ionizing radiation therapy, in the form of X-ray or γ-ray radiation, is administered to over half of all cancer patients in developed countries [1]. For certain cancer types, particularly early stage tumors, radiation therapy is used as a primary agent to treat tumors and has led to many successes for patients. However, this is by no means the case for all tumors; in fact, radiation therapy for many cancers has high rates of recurrence, especially in locally advanced or recurrent cases, leading to reduced quality of life and mortality in their patient populations. Failure rates for radiation therapy in locally advanced cases can be as high as 30% for distant failures in head and neck cancers [2], with equally high rates observed in several other tumor types.

For patients, the radiation therapy they receive is delivered in small dose fractions over the course of several weeks. Therapy is administered in this format because by fractionating the total radiation dose into small, repeated doses, normal tissues surrounding the tumor may be partially spared from off-target toxicities that lead to treatment complications while still achieving significant cell death in the tumor [3]. This normal tissue-sparing strategy does improve patient quality of life significantly, but it also increases the probability of tumor recurrence compared to a single, large dose because the time delay between doses also allows cancer cells to repair and regrow to an extent. As a result, certain cancer types are able to survive the course of radiation therapy and live on to induce local or distant failure through tumor regrowth and/or metastasis.

For the above reasons, there has been substantial interest and research regarding how to improve cancer patient outcomes for those treated with radiation therapy. Data over the course of the last century has shown that, by combining radiation therapy with other treatments, like surgery

and chemotherapy, overall cancer mortality is decreased substantially for many tumor types [4]. This multimodal approach to cancer treatment has become the standard of care for patients. While significant improvements over radiotherapy alone have been observed as a result, there is significant room for improvement that remains, particularly with regard to high-grade adverse events that diminish quality of life during and after treatment.

1.2 Motivation for the Study of Radiosensitizers

In light of the dose limiting toxicities of radiotherapy, a class of compounds called radio-sensitizers has been developed to enhance the effectiveness of radiation tumor cell killing. Many of these agents are small molecule drugs found to interact favorably with radiation therapy, and recent advances have also been made using nanoparticles as radio-sensitizers, including some formulations currently involved in clinical trials. Certain radio-sensitizers, such as chemotherapeutics like paclitaxel, cause increased tumor cellular sensitivity by initiating cell cycle arrest in more radiosensitive phases of the cell cycle (i.e. G_2/M) [5]. While somewhat successful in combination, these small molecule radiosensitizers tend to be systemically administered drugs with significant off-target toxicities.

These results inspired researchers to devise alternative formulations that could potentially mitigate normal tissue side effects, leading to a variety of novel strategies for drug delivery. More recently, approaches have focused on using nanomaterials that interact favorably with incident X-ray photons to emit secondary electrons, longer wavelength photons, or a combination of these to improve tumor cell killing. Many of these nanomaterials rely on high-Z metal components that are potentially hazardous if liberated from the particles. Some crystalline materials, such as high Z element oxides, are less susceptible to this due to their relative chemical stability (highly oxidized forms). One such formulation of hafnium dioxide nanoparticles, which sensitize cells through

secondary electron emission, have even reached phase I/II clinical testing in several cancer types, with some success [6]. This intratumorally administered adjuvant therapy's results provide significant motivation for further study on the development of nanomaterial-based radiosensitizers that can potentially improve upon the progress made to date.

1.3 Research Objectives

The proposed thesis involves two major aspects as well as one minor topic, each focused on developing and fully characterizing potentially translatable nanoparticle-based radiosensitizers. The first topic involved modifying the surface of a formerly developed block copolymer encapsulated calcium tungstate nanoparticle formulation with the intention of improving radiotherapy efficacy. Specifically, alterations were made by conjugating the ends of the hydrophilic block domains with a cell surface receptor ligand, folic acid, whose expression is elevated in many cancers. The impact of this change was examined experimentally to screen for mechanism of action, safety, and efficacy in human cell culture and murine xenograft models of head and neck squamous cell carcinoma (a solid tumor model) treated with primary X-ray therapy. Proposed efficacy enhancement was confirmed *in vitro* and *in vivo*, and mode of action details were successfully elucidated. In addition, translational feasibility was subsequently tested in a canine clinical case study in which a dog with a spontaneous soft tissue sarcoma was treated with the modified nanoparticle formulation; the results of this experiment suggested a favorable safety profile and efficacy improvements over primary radiotherapy may exist, though further clinical testing is needed to validate these results in a larger number of patients.

The second topic focused on the design and evaluation of a new formulation of calcium tungstate nanoparticles encapsulated by a photosensitizing polymer conjugate to facilitate a combination of radiation and photodynamic therapies. This was specifically accomplished via the

synthesis of a bilirubin-conjugated poly(ethylene glycol) that was then used to encapsulate the calcium tungstate nanoparticles. As was the case for the first topic, this new formulation was tested in a variety of experiments *in vitro* and *in vivo* to evaluate its potential utility for radio/photodynamic therapy (RT-PDT). These experiments confirmed the proposed efficacy benefits of combined RT-PDT in models of human head and neck cancers. The combination of bilirubin and calcium tungstate proved essential for the observed improvements, as bilirubin-PEG micelles alone did not provide any additional benefits with X-ray treatment. Further experimentation is needed to examine mode of cell death and confirm the observed efficacy benefits.

The third minor topic was a preliminary study dedicated to examining the dose distribution of the aforementioned nanoparticle radiosensitizers in murine tumor xenografts. Specifically, a pilot study was conducted comparing nanoparticle formulation distribution before and after mechanical agitation of the tumor. The aim of this study was to explore the benefits of tumor agitation post-injection for dose homogeneity improvement. This experiment utilized X-ray computed tomography (CT) scanning for nanoparticle detection. It was found that mechanical agitation of the tumor site after nanoparticle injection changed the local distribution of nanoparticles in the fluid space on the periphery of the tumor. These results further exploration to fully understand the effect of mechanical agitation on dose distribution and its subsequent effects on ultimate *in vivo* anti-tumor efficacy in combination with X-ray therapy.

2. LITERATURE REVIEW

2.1 Radiotherapy Mechanisms and Rationale for Multimodal Treatment Strategies

Electromagnetic radiations (X- and γ-rays) primarily operate by interacting with intracellular water (and other compounds) to produce ion radical and free radical species which subsequently diffuse to damage DNA [3]. These reactive oxygen species (ROS)-induced damages in the DNA include base damage, single-strand breaks (SSBs), and double-strand breaks (DSBs). The most biologically relevant of these for cell death is DSBs [3]. Cells attempt to repair DSBs by two main mechanisms: non-homologous end-joining (NHEJ) and homologous recombination repair (HRR) [7]. HRR is a high-fidelity DNA repair mechanism that uses sister-chromatids as templates for ensured high-fidelity repair and resultant sequence homology [7], whereas NHEJ is more prone to errors in reconnection of DSB ends. Certain error rates exist for each of these repair mechanisms and can lead to lethal chromatin aberrations [3]. These lethal chromatin aberrations induce cell death by a few potential mechanisms, most importantly through mitotic catastrophe [8]. This occurs when cells containing lethal chromatin aberrations attempt to divide during mitosis and are prevented from completing the process due to the presence of the malformed chromosomes.

Sparsely ionizing radiations, like X-rays, act through a mechanism called the indirection action of radiation, which means that most biochemical/biological damage relevant to cell death is induced via ROS generated within a few nanometers of the DNA backbone inside the nucleus [3,9]. Some of the incident X-ray photons may also operate via the direct action of radiation, where the photons ionize an atom within a chemical structure and then eject a fast electron into the target biomolecule (DNA in this case) instead of interacting with the biomolecule through the ROS intermediate (as is the case for indirect action of radiation) [9]. Low linear energy transfer (LET)

radiations like X-rays will favor the indirect action of radiation. Regardless, almost all of the biological effects of consequence for cell death will be caused by DNA damage, primarily in the form of DSBs, that is initiated by ROS within the cell nucleus. The modes of cell death initiated by ionizing radiation are apoptosis, mitotic catastrophe, necrosis, senescence, and autophagy [10].

As previously mentioned, mitotic catastrophe tends to dominate tumor cell death in response to ionizing radiations, and the second most important mechanism is apoptosis. However, the other modes are also present to varying extents, depending on the type of cancer cells. More radio-resistant cancer cells tend to have a diminished capacity for apoptosis (programmed cell death); these types of cells will have significantly increased survival after a given dose of radiation than those cancer cells that have functional apoptotic signaling pathways [3]. Mutations to the protein p53 can lead to diminished apoptotic response to cellular damage, and many cancer cell lines in laboratory use have been examined for their p53 (wild type vs. mutated) status [11]. The survival difference at varying doses of X-ray between cells with a functional apoptotic signaling (p53 wild type) pathway and those without (p53 mutants) is abundantly clear when examined using a clonogenic cell survival assay. These assays are classical radiobiology experiments in which cancer cells are grown at very low densities, irradiated with varying doses of X-ray, and then grown for a period of 2 weeks to determine the number of clonogenic (actively dividing) cell colonies that exist as a fraction of the amount growing in the plate prior to radiation.

Surgery is often combined with radiation therapy, but the role of radiotherapy in these cases is either to be administered after surgery to help kill macroscopic and microscopic residual cancerous tissue that was not resected or before surgery to allow for easier and more successful surgical resection of the bulk tumor tissue [10]. Surgery, unfortunately, is not always a treatment option for patients due to tumor location, potential impact on quality of life, or comorbidities that

prevent the patient from being placed under general anesthesia. As a result, for these cases, non-surgical treatment options will be employed to aid primary radiotherapy in effectively controlling tumors [12-14]. Even in cases where surgery is possible, these other modalities are sometimes administered as adjuvant therapies to further deter recurrence. Recurrent tumors also pose a special treatment challenge to oncologists due to the often-acquired resistance of the cancer cells to the prior treatments used.

Non-surgical modalities often combined with primary radiation therapy include chemotherapeutics and immunotherapies. The purpose of combining these treatments is to increase the probability of tumor control through preventing locoregional recurrence (either initial or subsequent) and metastasis. In cancers with intact apoptotic signaling pathways, certain chemotherapeutics, such as gemcitabine can complement radiation therapy by increasing the apoptosis response to a given dose of radiation [15]. Other chemotherapeutics can act independently of these apoptotic pathways to kill cancer cells through cell cycle arrest, necrosis, or by enhancing the probability of mitotic catastrophe in cancer cells after irradiation [16]. One such example of the latter chemotherapies is paclitaxel, which kills cancer cells on its own via cell cycle arrest; this resultant arrest happens to pause cancer cells in a particularly radio-sensitive phase of the cell cycle, further enhancing the cancer cell death in response to a given dose of radiation [5].

Immunotherapies operate by enhancing inherent anti-tumor immunologic responses present in the human immune system. This response can be a combination front in the form of CD4+/CD8+ T-lymphocytes, B-lymphocytes, NK cells, and macrophages [17]. These systemic changes can help to provide a more specific response to tumor cells [18]. This presumably pairs well with the more localized, bulk tumor eradication provided by radiotherapy. There is also some evidence that radiotherapy can induce a local immune response on its own in some circumstances

[19]. These therapies are relatively new and have recently been introduced to the standard care of oncology practice, so data regarding their use is not as widespread as those for chemotherapeutics.

A third non-surgical intervention that can be used in concert with radiation therapy is photodynamic therapy. Photodynamic therapy (PDT) is also a relatively new cancer treatment that operates via two types of photo-reactions: Type I and Type II [20]. Both reactions occur when a photosensitizer molecule (the molecule responsible for the PDT response) is excited by an appropriate illumination source and undergoes an internal electronic transition to either the short-lived singlet or longer-lived triplet states. In Type I reactions, this excited sensitizer molecule interacts with another chemical substrate (including solvent) to produce free radicals which then proceed to create oxygenated biological products via interaction with molecular oxygen [21]. In Type II reactions, the excited sensitizer molecule directly interacts with molecular oxygen to produce singlet oxygen ($^1O_2$) which can then directly act to oxygenate biological substrates in the cell [21]. Which reaction dominates depends on the photosensitizer used, the concentration of the sensitizer and molecular oxygen, and local solvent conditions. PDT tends to increase dramatically the amount of cell death by apoptosis and necrosis because photosensitizers tend to accumulate in or near cytoplasmic components and the reactive oxygen species generated via these two reaction types reacts readily with certain proteins and unsaturated lipids in the cell membrane and organelle membranes [21,22]. These reactions can disrupt cell membrane/organelle membrane integrity and result in necrotic cell death. Importantly, this mechanism can occur concurrently with ionizing radiation events inside of the cell nucleus and complement the radiotherapy cancer cell response by decreasing cell survival via increased necrosis. In addition, certain excitation sources for photosensitizers that are high energy (e.g. UV-range light) not only excite the sensitizer to mediate PDT but can also increase intracellular DNA damage through the production of pyrimidine dimers

and 6-,4-photoproducts, and can induce crosslinking damage to other components that collectively inhibit cellular mitotic activity [23]. Some of these can even be converted to DSBs in certain circumstances [24].

Taken together, each of these non-surgical adjuvants to radiotherapy can complement primary radiotherapy quite well by their independent mechanisms of action or by sensitizing cells to ionizing radiation through their mechanisms. By carefully pairing these treatments with radiation therapy, researchers can find strategies that significantly improve patient outcomes by decreasing tumor recurrence and metastasis. This proposed thesis details one such attempt at improving primary radiotherapy through the development of nanoparticle radiosensitizers for multi-modal treatment.

2.2 Solid Tumors Studied

A multitude of solid tumor types exist, each with unique challenges for treatment that prevent positive outcomes for patients. One common subtype of solid tumor is collectively referred to as head and neck squamous cell carcinoma (HNSCC). HNSCC tumors include tumors of the larynx, pharynx, oral and nasal cavities, as well as those of the tongue and lips [25]. Together, these tumors represent the 6th most common cancer in the world [26]. Due to the anatomy of the regions afflicted by HNSCCs, complete surgical resection is often difficult or involves severe organ function loss, especially in locally advanced stages [27]. In addition, rates of recurrence for HNSCC after primary radiotherapy can be as high as 60% for local failure [2]. Systemic chemotherapy is often co-administered for chemo-radiotherapy for clear clinical outcome benefits afforded by complementary modes of action (for reasons discussed previously) [28]. However, significant off-target toxicities are common and greatly diminish patient quality of life [29]. Thus, there is clear clinical relevance and motivation in studying HNSCCs in the context of radio-sensitizer

development because patient quality of life and even treatment outcomes could be significantly improved through the implementation of less systemically toxic, effective radio-sensitizers. The proposed thesis emphasizes the development of calcium tungstate nanoparticle-based radiosensitizers to address some of these clinical needs.

Another solid tumor subtype explored in this proposed thesis is soft tissue sarcoma (STS). STSs are often treated with radiotherapy pre- or post-surgery and this additional treatment can help to preserve limb function; thus, STSs are an attractive area of study for nanoparticle radiosensitizer development [6]. STS patients could potentially greatly benefit from the incorporation of effective radiosensitizers into their disease treatment by improving tumor response rates to standard radiotherapy regimens.

2.3 **Combination Radiation and Photodynamic Therapy**

As discussed in section 2.1, photodynamic therapy is a non-surgical modality that utilizes a photosensitizing molecule, oxygen, and light to effectively kill cells. Although radiation therapy and photodynamic therapy both mechanistically operate by creating reactive oxygen species, oftentimes their intracellular targets are distinct, also as discussed previously. Several pre-clinical studies combining radiotherapy and photodynamic therapy have been conducted using a variety of agents [30,31], but very few clinical studies have examined this combination. Most clinical studies involving photodynamic therapy are either single-agent therapy for shallow lesions or in combination with surgery to improve tumor control post-resection in reachable lesions [32], with only a few focused on using photodynamic therapy in concert with radiotherapy [33,34].

The preclinical work conducted to date suggests that combined radio/photodynamic therapy (RT-PDT) is promising for the treatment of cancer since the results have shown significant advantages in combination. From the mechanistic discussion in Section 2.1, the data from these

pre-clinical studies, and the limited clinical data for combined RT-PDT, it stands to reason that this multimodal approach is a potentially successful treatment combination that could significantly improve patient outcomes compared to single-agent primary radiotherapy. In addition, because photodynamic therapy displays very little systemic toxicity (mainly temporary light sensitivity) [35], RT-PDT could provide a potential alternative to chemoradiotherapy, which requires the use of systemic chemotherapies with significant off-target toxicities. For these reasons, a portion of the proposed thesis explores the implementation of RT-PDT using photosensitizer-conjugate encapsulated radio-luminescent nanoparticles with the aim of providing an alternative to primary radiotherapy and chemoradiotherapy for solid tumors.

2.4 **Nanoparticle-based Radiosensitizers**

A large variety of nanoparticle radio-sensitizers/enhancers have been synthesized and characterized in recent history [36,37]. The therapeutic enhancements afforded by these particles are dependent upon the production of secondary emissions from the nanoparticles under ionizing radiation. Some of the nanoparticles create these emissions via high-Z metal dopants in their cores (e.g., $SrAl_2O_4:Eu^{2+}$ (SAO) [38]), while others utilize crystalline oxide forms of these high-Z metals (e.g., Hafnium oxide [39]). Arguably the most successful of these, NBTXR3, is in/has currently completed Phase I/II/III clinical trials in the U.S. and in Europe for several distinct indications [6,40].

Both high-Z-doped and high-Z crystalline particles developed by others have shown pre-clinical and clinical success through a variety of mechanisms. Some utilize the emission of secondary electrons under X-ray radiation to enhance therapeutic response [41]. Others rely on the interaction between secondary photon emissions with photosensitizers that are incorporated into the nanoparticles to mediate X-ray-activated photodynamic therapy [30,38]. While these formulations have shown promise, each has challenges or limitations that can potentially limit their clinical

translation feasibility and utility. High-Z-doped nanoparticles carry inherent toxicity risks due to unavoidable potential liberation of free heavy metal ions, like rare earth elements, in the body after a prolonged period, which can cause detrimental accumulation effects [42]. While crystalline oxides of high-Z elements may be less risky from this perspective, they may be limited from a therapeutic perspective by the short mean-free pathlengths of their emitted secondary electrons [41].

In an attempt to address some of these shortcomings of other nanoparticle radiosensitizers, the proposed thesis develops polymer-encapsulated radio-luminescent calcium tungstate nanoparticles. Calcium tungstate nanocrystals mitigate high-Z element (tungsten) liberation because tungsten is only present in the form of WO_4^{2-}. In addition, these nanoparticles can provide potential enhancement over simpler high-Z crystalline formulations by therapeutic benefits afforded by alterations in the materials used to encapsulate the calcium tungstate cores.

3. FOLIC ACID-CONJUGATED RADIOLUMINESCENT CALCIUM TUNGSTATE NANOPARTICLES AS RADIO-SENSITIZERS FOR CANCER RADIOTHERAPY

Note: Chapter 3 is currently under review in *ACS Biomaterials Science & Engineering*.

Vincenzo J. Pizzuti[†,§], Rahul Misra[†,§], Jaewon Lee[†], Sandra E. Torregrosa-Allen[‡,‖], Melanie P. Currie[‡,‖], Scott R. Clark[†], Anish P. Patel[†], Christopher R. Schorr[†], Yava Jones-Hall[‖], Michael O. Childress[Δ], Jeannie M. Plantenga[Δ], Nicholas J. Rancilio[Δ], Bennett D. Elzey[‡,‖], and You-Yeon Won*[,†,‡]

[†]Davidson School of Chemical Engineering, [‡]Purdue University Center for Cancer Research, [‖]Department of Comparative Pathobiology, [Δ] Department of Veterinary Clinical Sciences, Purdue University, West Lafayette, Indiana 47907, United States
[§]These authors contributed equally to this work.

*Corresponding author

3.1 Abstract

Radiation therapy is a primary treatment modality for many forms of cancer. Normally, the highest tolerable dose of ionizing radiation is used to treat tumors, but limitations imposed by normal tissue complications present challenges for local tumor control. In light of this, a class of compounds called radio-sensitizers have been developed to enhance the effectiveness of radiation. Many of these are small molecule drugs found to interact favorably with radiation therapy, but recent advances have been made using nanoparticles as radio-sensitizers. Herein we report the utilization of radio-luminescent calcium tungstate nanoparticles that emit photoelectrons, UV-A, and visible light during X-ray irradiation, acting as effective radio-sensitizers. In addition, a folic acid-functionalized form of these nanoparticles was shown to enhance radio-sensitization in vitro and in murine models of head and neck cancer. Folic acid-functionalized particles were found to decrease UV-A-induced clonogenic cell survival relative to non-functionalized particles. Several possible mechanisms were explored, and the folic acid-functionalized particles were found to

mediate this increase in efficacy likely by activating pro-proliferative signaling through folate's innate mitogenic activity, leading to decreased repair of UV-A-induced DNA lesions. Finally, a clinical case study of a canine sarcoma patient demonstrated the initial safety and feasibility of translating these folic acid-functionalized particles into the clinic as radio-sensitizers in the treatment of spontaneous tumors.

Keywords: radiation therapy, radio-sensitizer, folic acid, nanoparticle, head and neck cancer, soft tissue sarcoma

TOC Graphic:

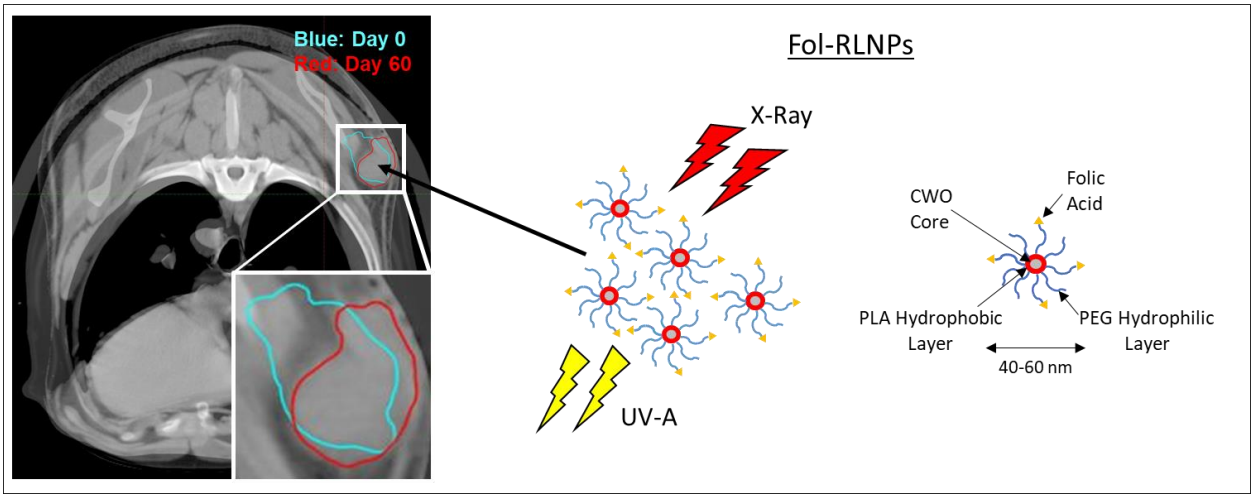

3.2 Introduction

Head and neck squamous cell carcinoma (HNSCC) is the 6th most common cancer worldwide[43], with an overall 5-year survival rate of around 50% for all HNSCC patients[44]. HNSCC has relatively high recurrence post-radiotherapy[2,45], with the rate of recurrence up to 60% for local failure and 30% for distant failure[2]. This is a significant problem considering that radiation therapy is a primary treatment modality for most cases of HNSCC[46], and is especially important for non-resectable or partially resectable tumors. To improve patient outcomes, particularly local tumor

control, the highest tolerable doses of X-ray are administered to patients, but limitations exist due to normal tissue complications that result from off-target dose-deposition[47]. Compounds known as radio-sensitizers are employed to overcome this barrier to improve tumor control by reducing the dose of radiation required to achieve a given tumor cell kill[48]. Many of these radio-sensitizers are chemotherapeutic molecules that were discovered to interact favorably with radiation therapy[16], but in recent years, other systems based upon nanoparticle platforms have been explored as potential radiotherapy enhancers[36,49]. Some of these have reached Phase I and II clinical trials, including NBTXR3 by the French company Nanobiotix[50]. Many of these nanoparticle radio-sensitizers utilize secondary electrons produced by their high-Z element components, which are limited by their short mean free path lengths[41].

As reported previously, our group has developed polymer-encapsulated, radio-luminescent calcium tungstate nanoparticles (RLNPs) that act as radio-sensitizers through their emission of photoelectrons, UV-A, and visible light under X-ray irradiation[51]. UV-A photons differ from secondary electrons in their mean free path length, which is orders of magnitude larger for the photons[51]. UV-A and visible photons can cause cytotoxic effects through the generation of reactive oxygen species (ROS), particularly singlet oxygen ($^1O_2$) from the excitation of endogenous photosensitizers, such as protoporphyrin IX (PPIX) and bilirubin, among others[52]. This mechanism is the basis for photodynamic therapy (PDT), which relies on oxygen, light, and a photosensitizer to function[53]. The combination of these photodynamic effects with other types of damage initiated by UV photons and secondary electrons affords RLNPs favorable radio-sensitization properties. In this study, we examine the effects of an updated formulation of RLNPs with 50 nm effective diameter post-filtration (compared to 170 nm previously) aimed at improving intratumoral nanoparticle transport. The effects of folic acid-functionalization on RLNP radio-sensitization

properties is also explored in detail. The RLNPs examined are comprised of calcium tungstate (CWO) nanoparticles (NPs) encapsulated by the block copolymer PEG-PLA, and a folic acid-functionalized form is used to produce Fol-RLNPs (10% Fol-PEG-PLA w/w).

Folic acid has been studied extensively in cancer research. By far the most frequent use of folic acid has been as a targeting agent in drug delivery applications, following the discovery of the overexpression of the folic acid receptor on some cancerous cells[54,55,56]. In addition to their inherent activity as an internalization facilitator for extracellular folate, folate receptors, particularly folate receptor alpha (FR-α), have been shown to promote intracellular proliferative signaling by upregulating STAT3 and MAPK activity[57,58]. In this study, we report that, at the low levels of functionalization (10%) used herein, folic acid-functionalization induces an enhancement in RLNP radio-sensitization efficacy that is not attributable to enhanced nanoparticle internalization but rather likely to the induction of pro-proliferative signaling leading to reduced repair of lethal UV-A radiation-induced aberrations.

RLNPs and Fol-RLNPs are administered via intratumoral injection. This is unlike the majority of therapeutic drugs used to treat cancers, which are systemically administered and can cause significant off-target toxicities[59,4]. Intratumoral injection is a clinically viable drug delivery method for cancer therapies that helps to overcome this limitation because the drug is only applied to the diseased tissue. This is particularly true in the case of HNSCC because the anatomy of the oropharynx allows for relative ease of access to most head and neck tumors. In the case of RLNP-mediated radio-sensitization, intratumoral injection ensures good localization of treatment because the therapeutic effects of the particles are only activated by the external X-ray source, which is focused on the tumor itself. In this way, the system is specific for diseased tissues and minimizes

off-target toxicity. The viability of this delivery method is demonstrated in the murine xenograft experiments conducted as well as in a canine clinical case study.

The safety and efficacy of RLNPs and Fol-RLNPs as radio-sensitizers for head and neck cancer radiation therapy are evaluated in this study. Fol-RLNPs demonstrated further sensitization enhancements compared with RLNPs, both *in vitro* and *in vivo*. Several mechanisms for this increase in efficacy were examined as well. Pre-exposure of cancer cells to Fol-RLNPs induced significant decrease in clonogenic cell survival after UV-A irradiation and X-ray radiation relative to PBS and RLNP-treated cells. Several mechanisms for this Fol-RLNP-mediated increase in efficacy were explored, including improved uptake efficiency, altered sub-lethal damage repair kinetics, changes in intracellular photosensitizer concentrations, and decreased repair capability in response to folate's induction of pro-proliferative signaling via its innate mitogenic activity. The data suggested that Fol-RLNPs enhanced efficacy relative to RLNPs is likely caused by Fol-RLNP-initiated pro-proliferative signaling that leads to decreased repair of UV-A-induced DNA lesions (i.e. double strand breaks). This potentially leads to diminished repair capacity for DNA lesions and subsequent increases in lethal chromatin aberrations and clonogenic cell death. Additionally, Fol-RLNPs combined with palliative X-ray therapy produced a significant reduction in tumor volume in a canine patient (i.e., pet dog) with naturally-occurring soft tissue sarcoma (STS), an interesting result considering that STS in dogs does not generally respond to X-ray radiation to a significant extent.

3.3 Materials and Methods

Synthesis of Calcium Tungstate Nanoparticles

$CaWO_4$ nanoparticles (CWO NPs) were synthesized via a microemulsion method as previously described, with some modification[60]. Briefly, 10 mL of cyclohexane was mixed with 1 mL of 1-hexanol (Sigma) and 1 mmol of CTAB (Sigma), and subsequently stirred at 70° C until transparent. Then two separate solutions were made: one with 0.2 mmol of Na_2WO_4 dissolved in 0.3 mL of water, and one with 0.2 mmol of $CaCl_2$ in 0.282 mL of water and 0.018 mL of 0.1 M HCl. These aqueous solutions were then immediately added to the first solution and vigorously stirred for 1 minute. The solution was then transferred to a Teflon-lined stainless-steel autoclave and baked in an oven at 160 °C for 24 hr. Afterward, the autoclave was gradually cooled, and the nanoparticles were separated and purified via centrifugation and ethanol/chloroform washes. The final solid was dried overnight in a vacuum oven at room temperature.

Synthesis of PEG-PLA and Fol-PEG-PLA

The block copolymers were synthesized via a ring-opening polymerization of racemic lactide with poly(ethylene glycol) (PEG) precursors, as previously described[61]. For poly(ethylene glycol-block-lactic acid) (PEG-PLA), 0.45 g of monomethoxy PEG (CH_3-PEG-OH, Sigma, M_n = 5,000 Da) and 0.45 g of racemic lactide were added to a round bottom flask, the flask was heated to 70 °C, evacuated under vacuum for 30 minutes, purged with Argon gas, and then 22 mL of anhydrous dichloromethane (DCM, Sigma) were added to dissolve the reactants. The reaction was catalyzed by 1,8-diazobicyclo[5.4.0]unde-7-ene (DBU, 98%, Sigma), with 0.22 mmol dissolved in 2 mL of DCM added directly to the reaction vessel. The reaction was run for 2 h at room temperature and was terminated by adding 15 mg of benzoic acid (>99.5%, Sigma). The PEG-PLA was precipitated by dropwise addition of the reaction solution to 1 L of mixed hexanes (Thermo Fisher). The precipitate was then dried overnight in a vacuum oven.

For the folate-functionalized PEG-PLA (Fol-PEG-PLA), synthesis was conducted as previously described, with some significant modifications (see Supporting Information Scheme S1 for alternate reaction scheme)[62]. 0.45 g of amine-terminated PEG (NH_2-PEG-OH, Laysan Bio, M_n = 5,000 Da) and 0.45 g of racemic lactide were added to a round bottom flask, and the same procedure as above was used to produce NH_2-PEG-PLA. This precursor then underwent conjugation with folic acid (Sigma). In the dark, 0.04 g of folic acid underwent carboxylic acid activation via 0.02 g N,N-dicyclohexylcarbodiimide (DCC, >99%, Sigma) and 0.01 g of N-hydroxysuccinimide (NHS, 98%, Sigma), all dissolved in 1 mL of DMSO (Sigma). After 12 hours of reaction at room temperature, a solution of 0.3 g NH_2-PEG-PLA and 0.003 g of triethylamine (TEA, >99.5%, Sigma) in 2 mL of dimethyl sulfoxide (DMSO) was added to the folic acid reaction mixture and allowed to react in the dark for 24 hours at room temperature. The reaction mixture was then syringe filtered to remove the dicyclohexylurea (DCU) byproduct, and the filtered solution was then dialyzed for 2 days against pure Milli-Q water with a MWCO of 1,000 Da. The final solution was then freeze dried.

Encapsulation of CWO NPs with PEG-PLA/Fol-PEG-PLA

RLNPs and Fol-RLNPs were prepared as follows. For RLNPs, 300 mg of PEG-PLA was dissolved in 3.9 g of N,N-dimethylformamide (DMF, Sigma), and 50 μL of a 10 mg/mL suspension of CWO NPs in DMF was added to the vial. The vial was then sonicated and mechanically stirred with an overhead stirrer at 10,000 rpm, and 2.1 mL of phosphate buffered saline (PBS) was added to the vial and allowed to emulsify for 10 minutes. The resultant emulsion was then centrifuged at 5,000 rpm for 10 min to pellet the encapsulated nanoparticles. The supernatant was discarded, and the pellet was resuspended in PBS to the desired concentration. Fol-RLNPs were prepared in an identical manner, with the following exceptions: the above process

was conducted in the dark, and 10% (30 mg) of the original PEG-PLA in the formulation was replaced with Fol-PEG-PLA. Two types of solutions were used for experiments: unfiltered nanoparticles suspended in sterile PBS, and filtered nanoparticles suspended in sterile PBS. Filtered solutions were passed through a 220 nm PVDF filter. Details on the size difference and distributions of the filtered vs. unfiltered particles can be found in the Supporting Information (SI) (characterized by dynamic light scattering (DLS)). DLS experiments were conducted at 0.025 mg/mL NP concentration.

Characterizations of Block Copolymers and Encapsulated CWO NPs

PEG-PLA and Fol-PEG-PLA structures were confirmed with ^{1}H-NMR (see Supporting Information Figure S1). Encapsulated CWO NPs were measured via dynamic light scattering (DLS, ZetaPALS, Brookhaven Instruments) at a 0.025 mg/mL nanoparticle concentration to find the average hydrodynamic diameter (see Supporting Information). Detailed morphologies were examined with high-resolution TEM using 2% uranyl acetate as a negative staining agent. Absorbance and fluorescence spectroscopy were conducted at 0.08 mg/mL CWO NP in PBS, and PPIX was at 20 μg/mL and 13 μg/mL for the PPIX and PPIX+ PEG-PLA CWO NP solutions, respectively. Spectroscopy was conducted in a quartz cuvette with 1 cm path length.

Cell Culture Maintenance

HN31 cells were thawed from stocks in liquid nitrogen and brought up in T-75 culture flasks. Cell culture media was comprised of DMEM (88% v/v), FBS (9% v/v), and supplemental penicillin/streptomycin and mercaptoethanol (3% v/v). Subculture of cells was conducted at 70-80% confluence.

Cell Viability Assays

For MTT assays, HN31 cells were seeded in 96-well tissue culture plates at a density of 0.5 x 10^4 cells per well and incubated for 24 hours at 37.0 °C in a 5% CO_2 incubator prior to exposure to CWO NPs. Cells were then treated with various concentrations of PEG-PLA-coated and uncoated CWO NPs (0.16, 0.32, 0.63, 1.25, 2.5 and 5.0 mg CWO per mL solution) (N = 5). After 24 hours of incubation, 10 μL of the MTT reagent was added to each well and incubated for additional 4 hours. Resultant formazan crystals were dissolved by adding 150 μL of a 10% w/v SDS solution to each well, and the absorbances at 570 nm were immediately measured using a microplate reader (BIO-RAD Microplate Reader-550). The wells with no cells, i.e., containing only the DMEM growth medium, the nanoparticles, and the MTT reagent were used as the blanks. The wells containing cells (that had not been treated with CWO NPs) in the medium with the MTT reagent were used as positive controls.

Clonogenic Cell Survival Assays

For clonogenic assays, HN31 cells were seeded in 60 mm culture dishes at densities 0.2 x 10^3 (0 Gy), 1.0 x 10^3 (3 Gy), 2.0 x 10^3 (6 Gy), and 5 x 10^3 (9 Gy) cells per plate and allowed to incubate overnight. After 4 h incubation with CWO NPs, cells were exposed to various doses of radiation with a 320 kVp X-Ray irradiator (X-RAD 320, Precision X-ray, North Branford, CT) at a dose rate of 2 Gy/min. Irradiated cells were cultured for 14 days. Colonies were stained with crystal violet, and those of more than 50 daughter cells in culture were counted (N = 4).

Intra/Extra-cellular PPIX Concentration Assays

For the PPIX level experiments, measurements were conducted using a fluorescence spectrophotometer (405 nm ex./630 nm em.) on cell extracts from 2 x 10^5 cells per well grown in 6-well plates. After seeding the cells in the plates, cells were incubated for 24 hours. Then 0.2

mg/mL CWO NP solutions were added (PBS only in the negative control group, 1 mM 5-aminolevulinic acid (5-ALA) for the positive control, 0.2 mM solution for free folic acid group, and empty 10% Fol-PEG-PLA micelles at the same polymer concentration used for RLNP and Fol-RLNP formulations) and incubated in the dark for 4 hours. Cell culture media were then removed and analyzed for extracellular PPIX content. Subsequently, to determine intracellular PPIX concentrations, cells were lysed using 0.1 M NaOH solution, and were then exposed to 3-fold (v/v) excess of DMF/isopropanol (100:1, v/v) at room temperature. Background fluorescence was corrected for by measuring fluorescence intensity from blank solutions created in an analogous fashion to the experimental samples, except exposure to HN31 cells/cell-tainted medium was avoided. Signals were then normalized to total cellular protein measured via the BCA assay on cell extracts (N = 6 per group).

CWO NP Uptake Flow Cytometry Experiments

HN31 cells were seeded into a 6-well plate at 2 x 10^5 cells per well and allowed to incubate in full growth medium for 24 hours. Then cells were exposed to appropriate NP solutions at 0.2 mg/mL for 4 hours and incubated in the dark. NP solutions had PPIX co-encapsulated to act as a fluorescent marker. After the exposure, cells were washed with PBS, removed from the plate, pelleted, and resuspended in cold PBS (4 °C). Analysis of cells was done using a BD Fortessa LSR SORP Cell Analyzer, with a 405 nm Violet Laser excitation and a BV605 (600-630 nm) emission filter.

Confocal Microscopy Experiments for Intracellular NP Tracking

HN31 cells were seeded onto microscope coverslips and allowed to reach 70 – 80% confluence, at which point they were exposed to 0.2 mg/mL NP solutions with co-encapsulated PPIX as a fluorescent marker. After 4 hours of incubation in the dark, cells were washed three

times with PBS and then fixed using cold methanol (4 °C). Cells were then imaged using a Zeiss LSM 880 Upright Confocal Microscope using a 63x oil immersion lens. DIC images were taken using a 488 nm laser, and the fluorescence images were taken using 405 nm excitation with 600 – 650 emission filter. Three images were taken of each sample type, and representative images are displayed in the Results & Discussion section.

Sub-lethal Damage Repair Assay

HN31 cells were seeded into 6-well tissue culture treated plates at a density of 1.0×10^3 cells per well and allowed to incubate overnight. Cells were then exposed to 0.2 mg/mL suspensions of nanoparticle/control samples for 4 hours (PBS, RLNP, Fol-RLNP). After exposure, appropriate plates were irradiated with a split X-ray dose of 2 + 2 = 4 Gy, separated by 0, 1, 2, 3, 4 and 5 hours between doses. As for standard clonogenic cell survival assays, the irradiated samples were cultured for 12 – 14 days and then stained and counted (N = 3).

UV-A Clonogenic Cell Survival Assays

HN31 cells were seeded into 6-well tissue culture treated plates at 2.0×10^2 cells per well and allowed to incubate for 24 hours at 37.0 °C in a 5% CO_2 incubator. Then the culture medium was removed and replaced with suspensions of saline/CWO NPs in cell culture medium. The three treatment groups were: PBS in medium as a control, 0.2 mg/mL unfiltered RLNPs in medium, and 0.2 mg/mL unfiltered Fol-RLNPs in medium. Cells were incubated with NP suspensions for 4 hours, and then these suspensions were removed and replaced with 1.0 mL of fresh culture medium. Subsequent UV-A exposure was conducted using a custom-built rig fit to a UV-A lamp with a peak light output at 365 nm. UV doses of 0, 0.50, 1.5 and 2.0 J/cm^2 was administered to the cells, and the culture plates were then returned to incubate for 10 days. After 10 days, fixation and staining of cell colonies was conducted as described above (N = 3 per group).

γ-H2AX Foci Visualization by Confocal Microscopy

HN31 cells were seeded onto microscope coverslips inside the wells of a 6-well tissue culture dish at a density of 5.0 x 10^4 cells/coverslip and allowed to grow to reach approximately 60% confluence under standard culture conditions. Then, culture media was removed from each well and replaced by culture medium containing 0.2 mg/mL suspensions of RLNPs and Fol-RLNPs (with PBS at the same volume concentration in the negative control), and the plate was incubated in the dark for 4 hours in a cell culture incubator. Afterward, the 6-well plate was irradiated with a dose of 2 Gy of X-rays using the same irradiator conditions as described for clonogenic cell survival assays. The 6-well plate was then placed back into an incubator for 2 hours. At 2 hours post-irradiation, culture media was removed, and the coverslips were individually washed 3 times using cold PBS. Then, cells were fixed using 3.7% (v/v) formaldehyde (Thermo Fisher) in cold PBS and then permeabilized using a 0.1% (v/v) Triton X-100 solution (Sigma) with 3x cold PBS washing steps between each. Coverslips were then subjected to immunofluorescent staining of γ-H2AX foci by subsequent addition of rabbit α-phospho-H2AX and α-rabbit-FITC monoclonal antibodies (ThermoFisher). Coverslips were subsequently mounted onto microscope slides using ProLong™ Diamond Antifade Mountant with DAPI (ThermoFisher) and allowed to set overnight in the dark. The prepared microscope slides were then imaged using a Zeiss LSM 880 Upright Confocal Microscope using a 63x oil immersion lens. Cell nuclei were imaged using a 405 nm laser for detection of DAPI fluorescence, and γ-H2AX foci were imaged using a 488 nm laser for detection of FITC. Approximately 10 μm-thick z-stacked images were taken for at least five separate locations for each sample at approximately 190x zoom (using 200 nm thick slices). Representative 2-dimensional image slices of each were then used for visual comparison of samples, and 3D-stacked reconstructions of each image set were analyzed to count

the number of foci per cell nucleus. At least 20 cell nuclei were counted per group for quantification of foci per cell nucleus. Foci counting was conducted using the ImageJ-based Fiji application 3D Object Counter tool[63].

BALB/C Mouse Tumor Xenograft Models

Male BALB/C nude mice (7 weeks old) were housed in a pathogen-free environment including standard cages with free access to food and water and an automatic 12 h light/dark cycle. The mice were acclimated to the facility for 1 week prior to beginning experiments, and all animals were cared for according to guidelines established by the American Association for Accreditation of Laboratory Animal Care (AAALAC). Subcutaneous HNSCC xenografts were produced by inoculation of 1.5×10^6 HN31 cells in 0.1 mL total volume of a serum free medium containing 50% Matrigel (BD Bioscience). Intratumoral nanoparticle injection at 10 mg/cc tumor of CWO NP in sterile PBS was conducted once tumors reached ~ 100 mm^3, approximately 7 days after inoculation, and split into two injections on consecutive days. For this study, the following treatment groups were used: Fol-RLNP + X-ray, RLNP + X-ray, and PBS + X-ray. Radiation treatments were conducted the day of injection and the subsequent day (2 Gy each) for a total of 4 Gy at a dose rate of 2 Gy/min using a 320 kVp laboratory X-ray irradiator (X-RAD 320, Precision X-ray, North Branford, CT). Tumors were measured with digital calipers in two dimensions: length (L) and width (W). Tumor volumes were calculated using $V = (L \times W^2) \times \pi/6$. N = M6 per group. Euthanasia criteria were > 20% body weight loss or tumor volume > 2000 mm^3. Mice were euthanized via spinal dislocation under anesthesia. Tumors were excised and weighed post-euthanasia.

Canine Clinical Case Study

A 10-year-old pet golden retriever was presented to the Purdue Veterinary Teaching Hospital for the treatment of a peripheral soft tissue sarcoma. The treatment protocol for this dog was approved by the Purdue Animal Care and Use Committee (Protocol # 1511001322). Written informed consent for treatment was obtained from the dog's owners, and it was enrolled in the following treatment regimen: one half of the tumor was treated with X-ray radiation only, and the other half was treated with an injection of Fol-RLNPs with X-ray radiation. X-ray doses were administered to the entire tumor region such that a minimum of 95% of the dose was delivered to 95% of the planning target volume. Planning target volume was developed using computerized radiation treatment planning software (Varian Medical Systems, Palo Alto, CA) to analyze computerized tomography (CT) images of the dog's tumor (GE Light Speed VCT, GE Medical Systems, Milkwaukee, WI). A total dose of 20 Gy in 5 fractions of 4 Gy was delivered at 400 monitor units (MU) per minute on consecutive days using 6 MV photons from a linear accelerator (Varian Clinac 6 MV Linear Accelerator, Varian Medical Systems, Palo Alto, CA). Immediately prior to the first fraction, Fol-RLNPs, suspended in sterile PBS, were injected intratumorally in a total volume of 3.3 mL at 10 mg/mL (Day 1). CT scans were conducted before, during and after treatment, as were hematology, serum biochemistry, and urinalyses and biopsies for histological analysis. Biopsies were taken using a small incision and a 6 mm punch instrument from each half of the tumor pre-treatment (approximately 3 weeks pre-treatment), in-treatment (day 3), and post-treatment and embedded in paraffin. Histology slides were prepared using hematoxylin and eosin (H&E) staining. The treatment schedule is summarized in the table below:

	Pre-treatment	Day 1	Day 2	Day 3	Day 4	Day 5	Day 12
Serum Biochemistry/ Urinalyses	X						X
Biopsy		X		X			X
CT Imaging	X			X			X
Fol-RLNP Injection		X					
4 Gy X-ray Fractions		X	X	X	X	X	

Statistical Analysis

For all p-values reported, p was calculated using either a two-tailed Student's t-test or a one-way ANOVA with the sample sizes listed in each figure caption. A p value of <0.05 was considered significant.

3.4 Results and Discussion

Nanoparticle Characterization

Poly(ethylene glycol-*block*-lactic acid) (PEG-PLA) and its folic acid-functionalized form (Fol-PEG-PLA) were used to encapsulate $CaWO_4$ (CWO) nanoparticles (NPs) to produce radio-luminescent nanoparticles (RLNPs) and folate-functionalized RLNPs (Fol-RLNPs), as described in the Materials & Methods. High-resolution TEM was used to examine the morphologies of the as-synthesized RLNPs. A representative image of filtered, encapsulated nanoparticles is shown in Figure 3.1. The sample was negatively stained with uranyl acetate. The lightly stained, raised regions in the image are the block copolymer domains surrounding the darker CWO nanoparticles. The hydrodynamic diameters of the particles were measured via DLS (see SI Figures 3.S2 and 3.S3 for DLS hydrodynamic diameter measurements and size histograms). Unfiltered particle samples were larger (600 – 800 nm effective diameter) and tended to cluster more than filtered particle samples (40 – 50 nm effective diameter).

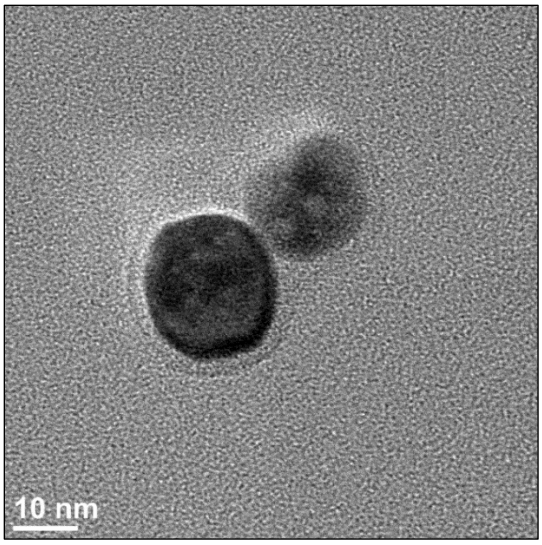

Figure 3.1. *High-Resolution TEM Micrograph of Encapsulated CWO NPs.* High-resolution TEM was conducted on filtered RLNPs and FOL-RLNPs after staining with uranyl acetate, and a representative image of filtered Fol-RLNPs is displayed above. Note: Experiment conducted with filtered particles.

Absorbance and fluorescence spectrophotometry were then used to examine the optical properties of the nanoparticles. Figure 3.2 displays the absorbance and fluorescence spectra of RLNPs as well as those of the photosensitizer PPIX and of RLNPs with co-encapsulated PPIX. The PPIX measurements were conducted to examine if the emission from RLNPs was sufficient to cause excitation of endogenous photosensitizers, such as PPIX, to produce additional reactive oxygen species (ROS) during X-ray treatment. As seen in Figure 3.2, the emission spectrum of RLNPs overlaps well with the absorbance spectrum of PPIX. PPIX has peak absorbance at 405 nm and peak emission at 630 nm. In Figure 3.2 (B), it is evident that a 250-nm excitation does not produce significant fluorescence in PPIX alone but does produce fluorescence when PPIX is co-encapsulated in RLNPs. The photons emitted from the CWO NPs are absorbed by the PPIX and result in PPIX fluorescence emission. This confirms that the nanoparticle system can effectively excite endogenous PPIX.

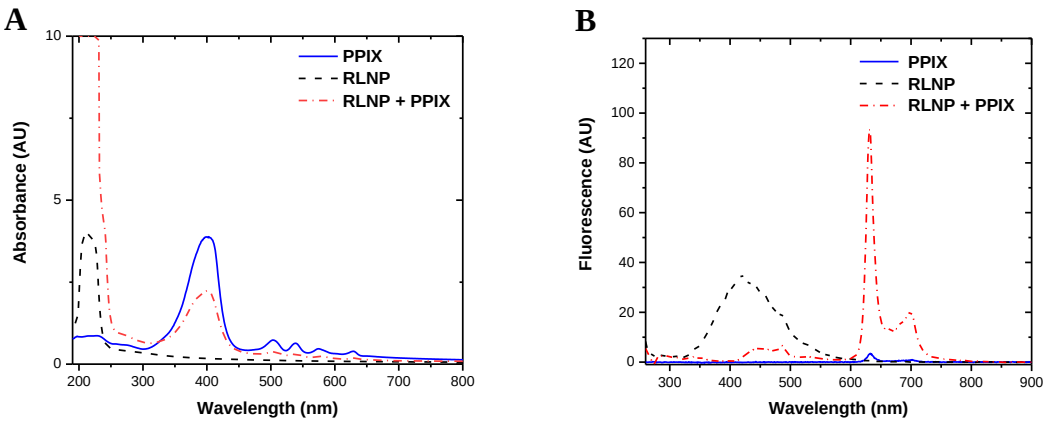

Figure 3.2. *Absorbance and Fluorescence Spectra of RLNPs.* (A) Absorbance Spectra of PPIX, RLNPs, and PPIX + RLNPs. (B) Fluorescence Spectra of PPIX, RLNPs, and PPIX + RLNPs with 250 nm excitation. Readings were taken at 10 nm intervals. Note: Experiment conducted with unfiltered particles.

Because CWO is a scintillating material, exposure to high energy X-rays causes CWO NPs to emit long wavelength ultraviolet (UV-A) and visible light. A measurement of the UV-A fluence emitted from CWO NPs following irradiation was conducted at various doses of X-ray radiation. The UV fluence was estimated by encapsulated-PPIX photobleaching measurements. Figure 3.3 shows that the UV-A fluence from the CWO NPs increases with increasing radiation dose but begins to plateau at higher doses. This experiment confirms that RLNPs/Fol-RLNPs are in fact radio-luminescent and provides an estimate of UV-A dosimetry. Incident UV radiation has a penetration depth of less than 1 mm in tissue[64], and this limits the possibility of delivering any significant dose beyond tissue surfaces using standard illumination sources, preventing its utility in treating solid tumors. RLNPs/Fol-RLNPs can potentially overcome this limitation by providing a more even dose of UV radiation in that the dose distribution is mainly dependent on the nanoparticle distribution within a tissue. With these properties confirmed, subsequent examination of biological safety and efficacy of RLNPs/Fol-RLNPs was conducted.

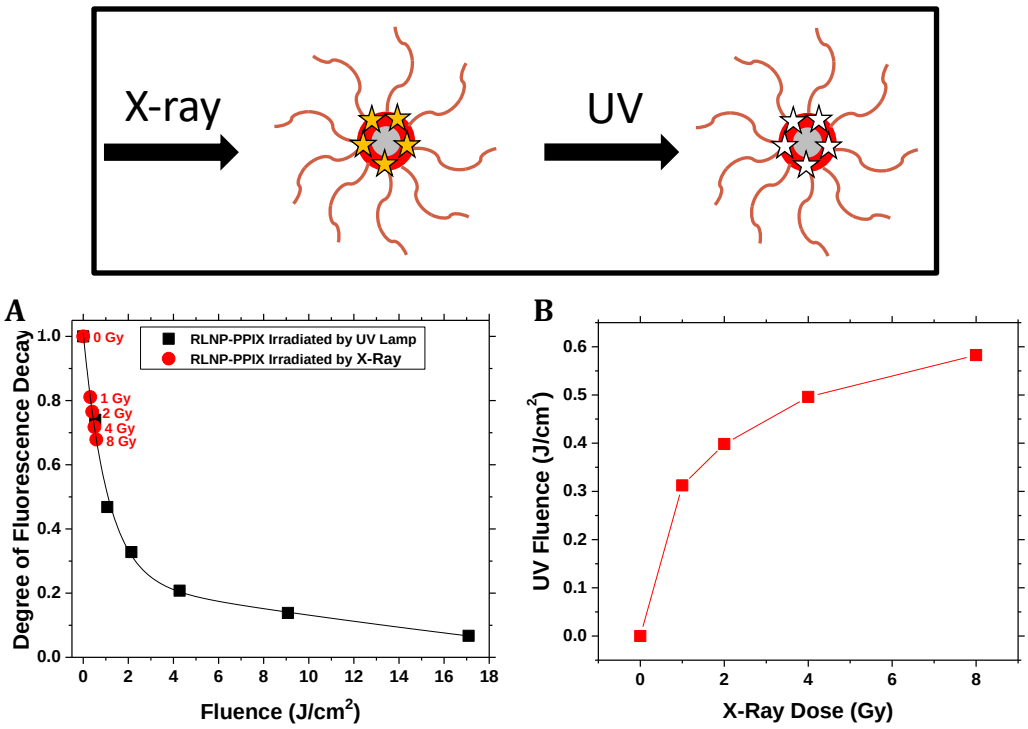

Figure 3.3. *CWO NP Radioluminescent UV-A Fluence Measurements.* Overlay: Schematic diagram of experimental design, with a PEG corona (blue curves) surrounding PLA (red shell) with encapsulated PPIX (stars) around a CWO NP core (gray center). (A) 320 keV X-ray irradiation photobleaching plotted with photobleaching control curve from UV-A lamp irradiation (365 nm). Experimental details can be found in the article by Jo et al[51]. (B) Tabulated UV-A fluence as a function of radiation dose. Note: Experiment conducted with unfiltered particles.

Biological Evaluation of Nanoparticles

RLNPs were designed to exhibit cytotoxic effects when exposed to external X-ray or γ radiation sources, and to be minimally toxic in the absence of such activation. MTT cell viability assays were conducted against HN31 cells (human pharyngeal squamous cell carcinoma) to ensure that pristine CWO NPs ("CWO NPs") as well as PEG-PLA-encapsulated CWO NPs ("RLNPs") and folic acid-functionalized PEG-PLA-encapsulated CWO NPs ("Fol-RLNPs") were minimally toxic in the absence of external ionizing radiation. For this experiment, dilutions of the respective nanoparticle solutions were prepared and incubated with the cells for 24 hours. The results are displayed in Figure 3.4. For reference, in subsequent *in vitro* testing, a therapeutic concentration of 0.2 mg/mL CWO NPs was generally used. Minimal losses in cell viability were observed except at doses much higher than *in vitro* therapeutic levels (2.5 and 5 mg/mL) for bare CWO NPs, RLNPs,

and Fol-RLNPs. The somewhat large standard deviations in this figure are likely attributable to the low cell count used (5000 cells/well).

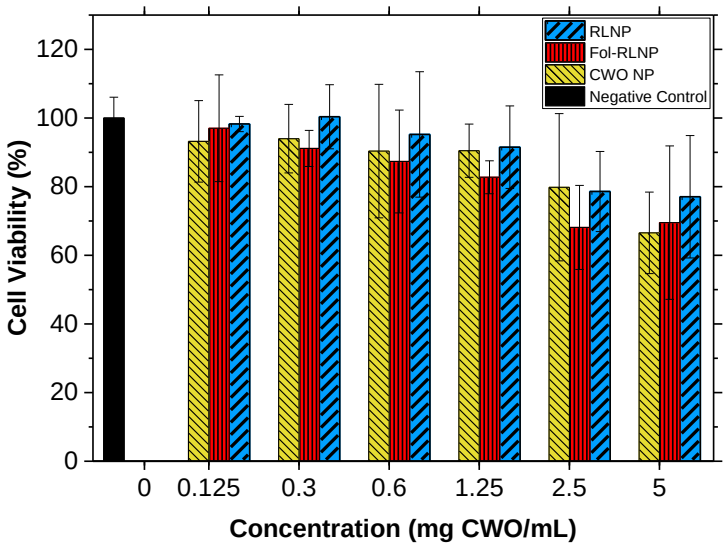

Figure 3.4. *HN31 Cell Viability with Exposure to NPs.* Bare CWO NPs, RLNPs, and Fol-RLNPs exposure in HN31 cells. Viability measured by MTT assay. HN31 cells were seeded in 96-well tissue culture plates at a density of 0.5 x 10^4 cells per well and incubated for 24 hours. MTT cell viability assay was performed at 24 h post treatment. 0 mg/mL represents the negative control for these experiments. All error bars represent standard deviation (N = 3). Note: Experiment conducted using unfiltered particles.

Next, RLNPs and Fol-RLNPs were examined for their ability to induce radio-sensitization/ cytotoxic effects via a clonogenic cell survival assay against HN31 cells. An appropriate number of cells for each dose were plated into 60 mm culture dishes and exposed to either PBS, RLNPs, or Fol-RLNPs for 4 hours prior to 320 kVp X-ray irradiation. The results of this experiment, displayed in Figure 3.5, indicate that both RLNPs and Fol-RLNPs produce a shift in the cell survival curve for HN31 cells, representing enhanced cytotoxic effects. Fol-RLNPs and RLNPs exhibited sensitizer enhancement ratios (SER) of 1.45 and 1.21 at 10% survival fraction, respectively.

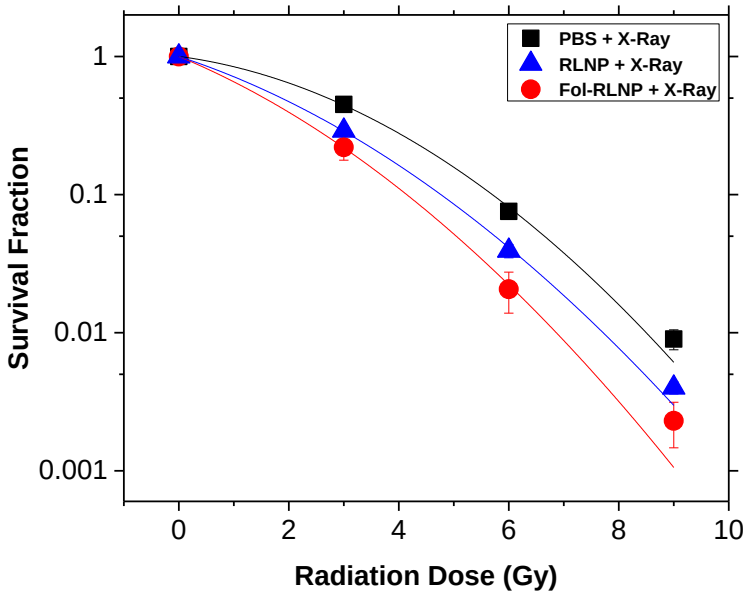

	α	β	α/β	SER
X-ray only	-0.123	-0.049	2.51	-
RLNP + X-ray	-0.300	-0.039	7.69	1.21
Fol-RLNP + X-ray	-0.3805	-0.042	9.06	1.45

Figure 3.5. *Clonogenic HN31 Survival with NP Treatment.* HN31 cells were seeded in 60-mm culture dishes at densities of 0.2 x 10^3 (0 Gy), 1.0 x 10^3 (3 Gy), 2.0 x 10^3 (6 Gy), and 5.0 x 10^3 (9 Gy) cells per plate. After 4-hour incubation with RLNPs or Fol-RLNPs, cells were exposed to various doses of radiation with a 320 keV X-ray irradiator at approximately 2 Gy/min. Irradiated cells were cultured for 14 days. Colonies of more than 50 daughter cells in culture were counted (N = 4 plates per group). Table displays the parameters for the linear quadratic model fits ($S = \exp(\alpha*D + \beta*D^2)$), where S is survival fraction, D is radiation dose, and α and β are fitted parameters) and sensitizer enhancement ratios (SERs) at 10% survival fraction. Error bars represent standard deviations. Note: Experiment conducted using unfiltered particles.

The UV-A light generated from Fol-RLNPs and RLNPs via X-ray excitation causes a radiation sensitization effect in the radio-resistant cell line HN31, as evidenced by the increase in α/β and SER values. Fol-RLNPs exhibited further improvements in radio-sensitization compared to RLNPs.

Several possible explanations for the enhanced efficacy of Fol-RLNPs were proposed and experimentally tested: (1) Fol-RLNPs increase endogenous photosensitizer PPIX levels resulting in increased reactive oxygen species (ROS) production relative to RLNPs, (2) Fol-RLNPs are

internalized by HN31 cells more readily than RLNPs, (3) Fol-RLNPs have different intracellular fates (more favorable for PDT) once internalized compared to RLNPs, (4) Fol-RLNP exposure alters sub-lethal damage repair (SLDR) mechanisms/kinetics and promotes an increased accumulation of lethal chromatin aberrations compared to RLNP exposure, and (5) exposure to Fol-RLNPs increases the effects of UV-A damage in HN31 cells compared to RLNP-treated cells, leading to an increased number of lethal aberrations and subsequent reduction in clonogenic cell survival. Each of these were tested independently, and the experimental results examining proposed mechanisms (1) through (4) displayed no difference between Fol-RLNP and RLNP-treated cells. Information regarding these results can be found in the Supporting Information (Figures 3.S4 – 3.S10).

In the end, mechanism (5) was found to be the driving force for the increase in treatment efficacy observed. Fol-RLNPs decrease clonogenic cell survival after exposure to UV-A radiation relative to RLNP treatment. The results of this UV-A clonogenic cell survival assay are displayed in Figure 3.6.

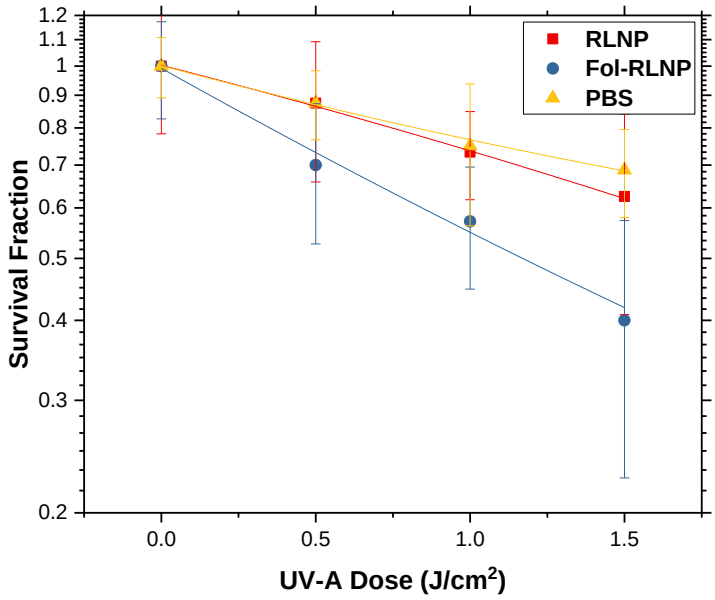

Figure 3.6. UV-A *Clonogenic HN31 Survival with NP Pre-Treatment.* HN31 cells were seeded in 6-well culture plates at a density of 0.2 x 10^3 cells per well. After 4-hour incubation with PBS, RLNPs or Fol-RLNPs, culture media were replaced, and cells were exposed to various doses of UV-A radiation using a UV-A lamp (peak emission at 365 nm). Irradiated cells were cultured for 14 days. Colonies of more than 50 daughter cells in culture were counted (N = 3 per group). Error bars represent standard deviations. Data points were fitted using the linear quadratic model ($S = \exp(\alpha*D + \beta*D^2)$), where S is survival fraction, D is radiation dose, and α and β are fitted parameters, just as for X-ray irradiation experiments. Note: Experiment conducted using unfiltered particles.

The increased UV-A clonogenic cell death under Fol-RLNP exposure explains the majority of the efficacy increases relative to RLNP exposed cells. One can use the relative decrease in survival fraction at a given UV-A dose combined with the X-ray induced UV-A dosimetry data from Figure 3.3 to predict the decrease in survival fraction of Fol-RLNP-treated relative to RLNP-treated cells expected at each X-ray dose (a similar procedure was previously described in detail by Jo et al.[65]). This analysis was completed using the data from Figures 3.3, 3.5, and 3.6 to create a projection for the expected Fol-RLNP-treated survival curve as a function of X-ray dose and was compared to experimental values of these survival fractions from Figure 3.5. The results are displayed in Figure 3.7. As seen in the figure, this predictive method matches the experimentally

observed behavior quite well. Please note that the experimental values displayed are reproduced from Figure 3.5.

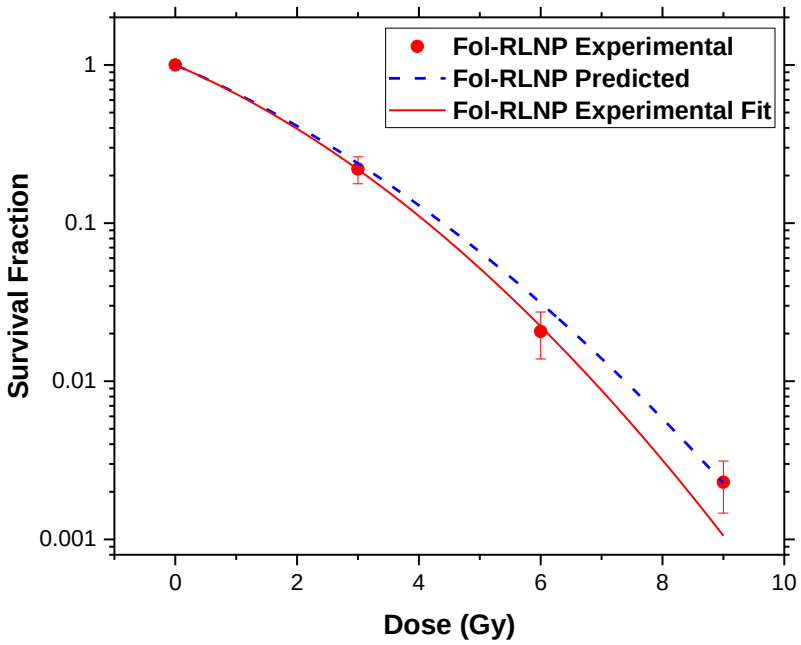

Figure 3.7**.** *Experimental Clonogenic Cell Survival Compared to UV-A Predicted Surival for Fol-RLNP Treated Cells.* Using the fractional reduction in clonogenic cell survival between Fol-RLNP and RLNP-treated cells after UV-A irradiation from Figure 3.6, the expected UV-A dosimetry at each X-ray dose level from Figure 3.3, and the experimentally observed clonogenic cell survival after X-ray irradiation for each group from Figure 3.5, the expected survival fractions for Fol-RLNP treated cells was predicted and compared to experimentally observed values above. This rudimentary prediction matches quite well with the observed survival fraction data. The prediction curve values were calculated by multiplying the survival fraction of RLNP-treated cells under X-ray by the fractional decrease in UV-A induced survival fraction for Fol-RLNPs vs. RLNPs at the UV-A dose expected for each incident X-ray dose. The best fit curves of these predicted survival fractions compared with the experimental values were plotted above. Fol-RLNP experimental values reproduced from Figure 3.5 here for convenience.

Why might Fol-RLNP pre-exposure sensitize cells to UV-A induced clonogenic cell death? We propose that the pro-proliferative signaling induced by folate mitogenic activity leads to this observed effect. UV-induced DNA lesions can be converted into double-strand breaks (DSBs), which can be subsequently converted into lethal chromatin aberrations[66], and signals promoting cell cycle progression and proliferation may inhibit the cell's ability to adequately repair the induced UV damage by forcing it to undertake the repair and cell cycle progression pathways

simultaneously[67]. This then leads to a larger number of lethal chromatin aberrations at the same UV dose for cells exposed to elevated folate levels and provides a reasonable explanation for the Fol-RLNP enhanced efficacy. A diagrammatic summary of this proposed mechanism is displayed in Scheme 3.1.

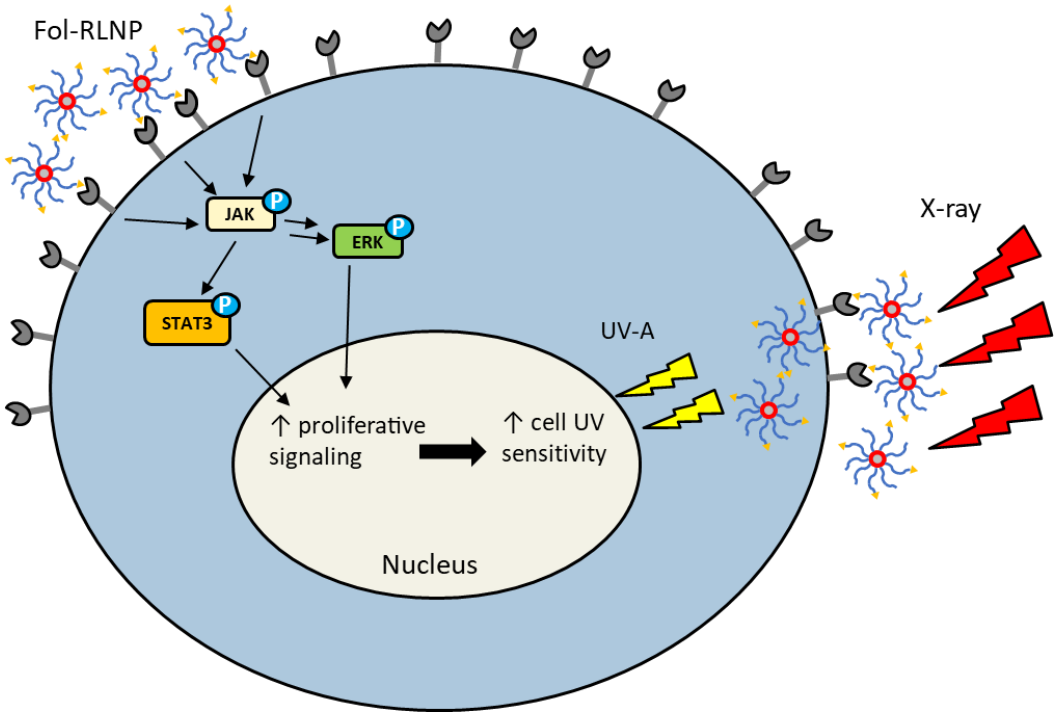

Scheme 3.1. *Proposed Mechanism for Fol-RLNP Mediated Increase in UV-A Sensitivity.* In the proposed mechanistic diagram above, Fol-RLNPs (labeled above) bind via folic acid to folate receptors (gray protrusions) and initiate activation of JAK as described in the text. JAK activation then leads to subsequent activation of STAT3/ERK via phosphorylation, which initiates pro-proliferative signaling in the cancer cell nucleus. This pro-proliferative signaling leads to somewhat diminished repair of UV-A initiated lesions in the cell, ultimately increasing cellular sensitivity to UV-A radiation and subsequently leading to increased clonogenic cell death. This likely explains the discrepancy in UV-A induced clonogenic cell survival between cells treated with RLNPs vs. Fol-RLNPs.

To compare the number of DSBs per cell nucleus after exposure to PBS or NP suspensions at the same X-ray dose, an immunocytochemistry staining experiment specific for γ-H2AX foci (a DSB marker) was conducted. These nuclear foci form as the result of the rapid phosphorylation of the histone H2AX in response to DSB formation near each lesion site[68]. In Figure 3.8, representative 2D images of each treatment group at 2 hours post-radiation (1 Gy X-rays) and counts of foci per cell nucleus are displayed. For the foci counting, a 3D object counter program utilizing the ImageJ-based Fiji application was employed[63]. From these quantification results, PBS

and RLNP-treated cells display similar numbers of foci per nucleus at 2 hours post-irradiation, whereas Fol-RLNP-treated cells have a significantly increased number. Recall that RLNPs and Fol-RLNPs emit the same amount of UV-A and visible light in response to X-ray irradiation, so differences in the number of DSBs between RLNP- and Fol-RLNP-treated cells are more likely due to changes in cell response to X-ray/UV-A rather than alterations in dosimetry. These data support the proposed mechanism of action because the increased number of foci (DNA lesions) at 2 hours post-irradiation indicated that Fol-RLNP-treated cells may not be as efficient in repairing DSBs as compared to PBS or RLNP-treated cells due to the divided efforts for repair and proliferation.

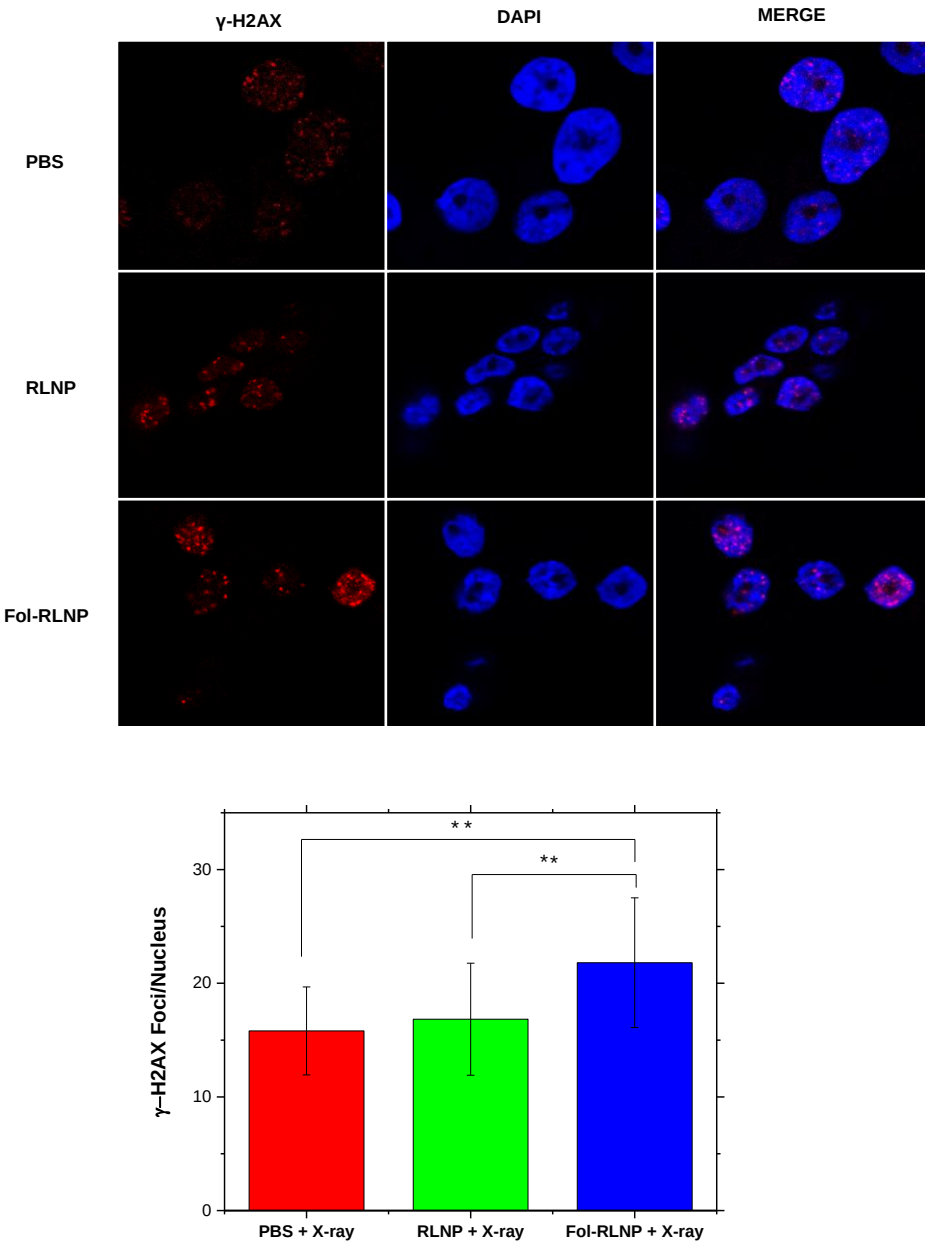

Figure 3.8. *γ-H2AX Foci Visualization and Quantification 2 Hours Post-irradiation.* HN31 cells were seeded in 6-well culture plates onto gelatin-coated microscope coverslips and allowed to grow until about 60% confluence. After 4-hour incubation with PBS, RLNPs or Fol-RLNPs, cell samples were exposed to 1 Gy of X-rays at a dose rate of 2 Gy/min. At 2 hours post-irradiation, cells were fixed and permeabilized, and then immuno-stained for γ-H2AX foci as described in the Materials & Methods. Coverslips were then mounted onto microscope slides using DAPI-containing antifade mountant. Images were taken using a Zeiss upright confocal microscope with a 63x oil-immersion objective lens in a Z-stack at several locations on each slide with 200 nm-thick slices. Representative 2D slices for each sample are displayed at ~ 190x. Quantification was completed using the ImageJ-based Fiji to count the number of 3D foci present per cell nucleus. At least 20 cells were counted for each sample. Error bars represent standard deviations. Double asterisks denote p-values of < 0.001, calculated using two-tailed student's t-test. Notes: Experiment conducted using unfiltered particles and each image was modified to enhance brightness by the same amount for each sample to improve visual clarity in the text.

Once *in vitro* safety, efficacy, and mechanisms were examined, the efficacy of the nanoparticles was then evaluated *in vivo* in an immune-deficient murine xenograft HNSCC model with a sub-therapeutic radiation dose (2 + 2 = 4 Gy). This experiment was conducted in BALB/C Nude mice with HN31 subcutaneous xenografts and was divided into two separate sub-experiments: irradiated groups at one time and un-irradiated groups from a separate time.

Figure 3.9 shows the tumor volume versus time as well as mouse survival curves for both irradiated (top figures) as well as un-irradiated (controls, bottom figures) groups. Please note that because these were conducted at separate times, the un-irradiated tumor growth kinetics and therefore mouse survival may be slightly different due to small variations in tumor doubling time and minute differences in tumor burden from mice from distinct litters. As shown in the figure, Fol-RLNPs significantly enhanced the effect of radiation, while the effect was not significant for non-functionalized RLNPs. Note that because mice in the PBS + X-ray group and in the RLNP + X-ray group had to be euthanized on days 14 and 15, respectively, there is no statistically relevant basis for comparison for the Fol-RLNP group at longer times for tumor volume plot. Of note, tumor volume measurements overestimated tumor volume compared to tumor volumes calculated from final tumor weights, as detailed in supplemental Figure 3.S11.

As shown in the figure, a clear difference in survival time for the groups was apparent for mice treated with Fol-RLNP + X-rays. The difference in survival for the Fol-RLNP group (median survival time: 40.5 days post-implantation) was significantly different from both the PBS + X-ray only group (median survival time: 27.5 days post-implantation) and the RLNP + X-ray group (median survival time: 28.0 days post-implantation). P-values for each combination are displayed in the table included in Figure 9. This result suggests that the Fol-RLNP efficacy effects are also present *in vivo*.

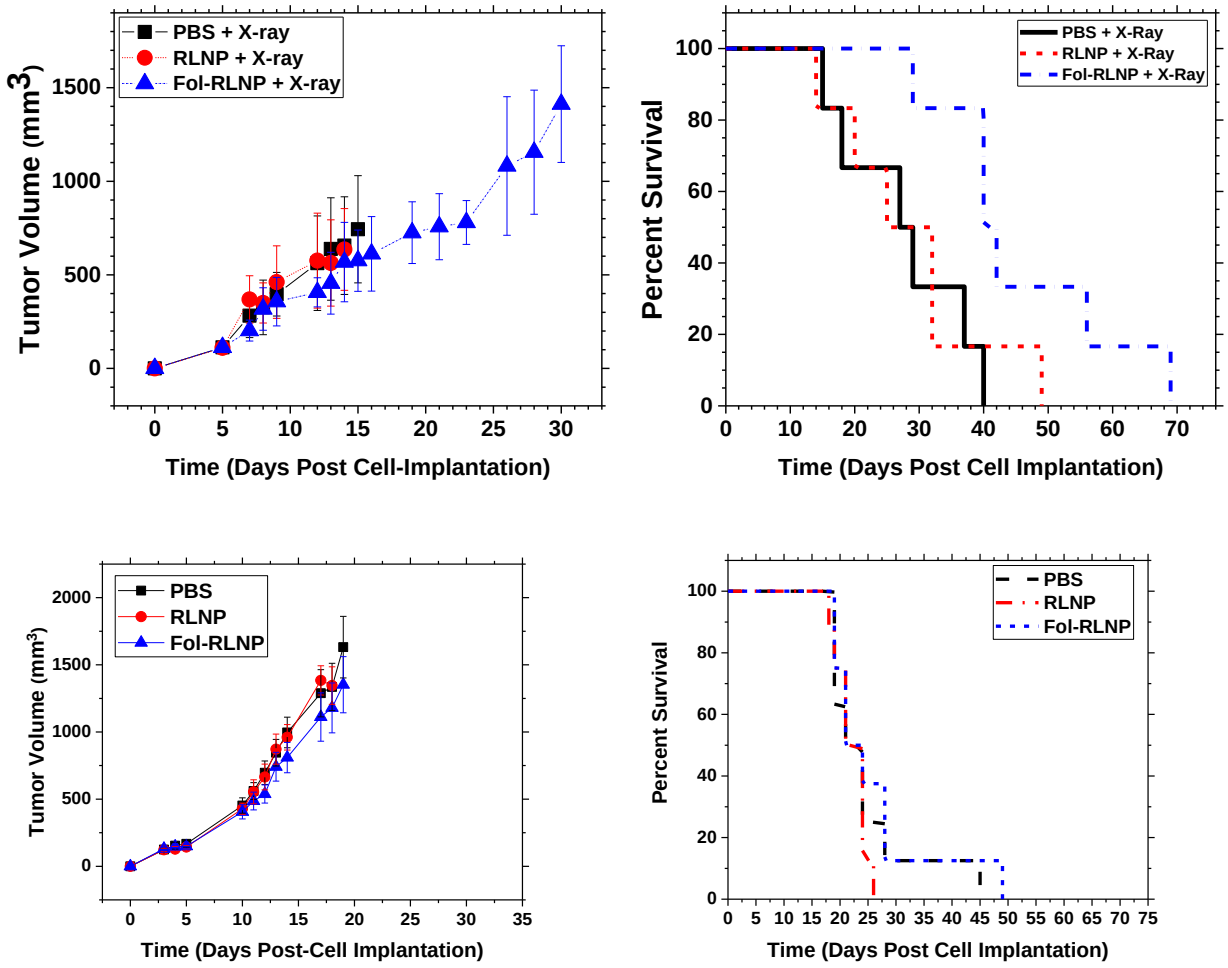

	X-Ray Only	Fol-RLNP + X-Ray
Fol-RLNP + X-ray	3.24E-07	-
RLNP + X-Ray	0.90019	1.46E-05

Figure 3.9. *Murine HNSCC Xenograft with NP Treatment.* Subcutaneous xenografts were produced by inoculation of 1.5 x 10^6 HN31 cells in 0.1 mL total volume in BALB/C nude mice (day 0). Intratumoral nanoparticle injection of 100 μL of 10 mg/mL CWO NPs in sterile PBS was conducted in two portions over two days (days 4 and 5) once tumors reached ~ 100 mm^3; blank PBS was injected in the control (X-ray only) group. "Sub-therapeutic" (i.e., low-dose) radiation treatments with 320 keV X-rays were conducted on the second day of injection (day 5) and the subsequent day (day 6, 2 Gy each) for a total of 4 Gy. Tumors were measured with digital calipers. (TOP LEFT) Tumor volumes for each group are displayed up to the first euthanasia event that occurred in each group. Error bars represent standard error. (TOP RIGHT) Kaplan-Meier survival curves for each group were generated. (BOTTOM LEFT) Tumor volume curves for un-irradiated controls (PBS, RLNP, Fol-RLNP), which are data displayed from a separate sub-cutaneous xenograft experiment from the irradiated samples (experiments were conducted at separate times). (BOTTOM RIGHT) Kaplan-Meier survival curves for un-irradiated controls (again, a distinct experiment from the irradiated groups). Euthanasia criteria were > 20% body weight loss or tumor volume > 2000 mm^3. The Fol-RLNP group survival (blue dot-dashed line, right) was significantly different than the RLNP group (red dashed line) and the X-ray control group (black solid line). P-values of survival data for the irradiated groups (top right plot) are displayed in the table for each combination. P-values determined using one-way ANOVA. N = 6 per group for irradiated groups, N = 8 per groups for un-irradiated controls. Note: Unfiltered particles were used for this experiment.

Next, we examined if the mouse survival results presented in Figure 3.9 could be predicted using in vitro clonogenic survival data shown in Figure 3.5. Using the linear-quadratic model parameters (α and β) obtained from clonogenic assay results shown in Figure 3.5, we can predict values of survival fraction (SF) for HN31 cells irradiated with 4 Gy in 2 fractions. In this situation, survival fraction (SF) can be estimated as follows: SF(D = 4 Gy in 2 fractions) ≈ [SF(D = 2 Gy in single fraction)]^2, assuming the time interval between radiation fractions (1 day) was sufficient for cellular recovery from sub-lethal radiation damage[69]. SFs were then determined for each treatment group: 0.413 for PBS + X-ray, 0.2205 for RLNP + X-ray, and 0.1557 for Fol-RLNP + X-ray. For the in vivo studies presented in Figure 3.9, HN31 xenografts were treated with X-rays when the tumor volume reached 100 mm^3 (V_0) (containing an estimated number of approximately 1.0 × 10^8 cells, assuming a cell density of 10^9 cells per cc of tumor[69]). For the mouse study, the number of clonogenically viable cells within the tumor immediately following the second fraction of 2 Gy radiation were calculated: 4.13 × 10^7 cells for PBS + X-Ray, 2.205 × 10^7 cells for RLNP + X-ray, and 1.557 x 10^7 cells for Fol-RLNP + X-ray. From Misra, et al.[69], the doubling time (t_{double}) of HN31 cells in mouse xenografts is approximately 5.09 days. To determine the median mouse survival values for each treatment group, the post treatment volumes (calculated from the number of cells surviving from above), the doubling time, and a final tumor volume of 2.0 cc (V_{final}) were substituted into the formula:

$$t_{survival} = \ln\left(\frac{V_0}{V_{final}}\right) \times \frac{t_{double}}{\ln(2)} \quad (1)$$

The results of this prediction for median mouse survival in treatment groups were 28.5 days for PBS + X-ray, 33.1 days for RLNP + X-ray, and 35.7 days for Fol-RLNP + X-ray. For comparison, the experimental values in days post-radiation were 21.5 days for PBS + X-ray, 22 days for RLNP + X-ray, and 34.5 days for Fol-RLNP + X-ray. In general, this model predicts a

clear increase in mouse survival for Fol-RLNP-treated mice, which was observed. This simple model does not capture the quantitative behavior for X-ray and RLNP + X-ray treated mice survival but does agree quite well with the predicted value for Fol-RLNP + X-ray treated mice (a difference of 1 day).

Canine Clinical Case Study

A 10-year-old pet golden retriever was presented to the Purdue Veterinary Teaching Hospital for the treatment of a soft tissue sarcoma (STS). A radiation treatment plan was designed to deliver 20 Gy in 5 fractions on consecutive week-days (4 Gy per fraction) using 6 MV photons delivered from a linear accelerator. A 3D conformal treatment plan was developed to deliver at least 95% of the dose to 95% of the planning target volume. The treatment plan was developed using computerized radiation treatment planning software to analyze computerized tomography (CT) images of the dog's tumor. Primary radiation therapy alone for canine STS does not typically result in considerable responses for grossly measurable disease[70]. For this study, one side of the tumor was injected with Fol-RLNPs at a final concentration of 3 mg CWO per cm^3 tumor, and the other side of the tumor received no injection. The radiation doses were then administered to the entire tumor. The caliper measured tumor volume on the day of treatment was 40.7 cm^3, and one month following treatment the caliper measured tumor volume had been reduced to 21.5 cm^3. Clinically significant adverse events in this case were minimal, with only the formation of a sterile abscess with a small amount of exudative drainage. Following oral antibiotics and bandaging, the wound healed spontaneously within 4 weeks. No clinically significant biochemical or hematological changes were detected using standard testing for organ function (complete blood count, serum biochemistry, and urinalysis). Figure 3.10 displays CT scans one-month pre-treatment in (A), immediately post-injection in (B), and one-month post-treatment in (C). Table

3.1 details the CT measurements of the tumor taken at several points during treatment. The volume reduction reported from the CT scans here is consistent with the volume reduction measured with calipers.

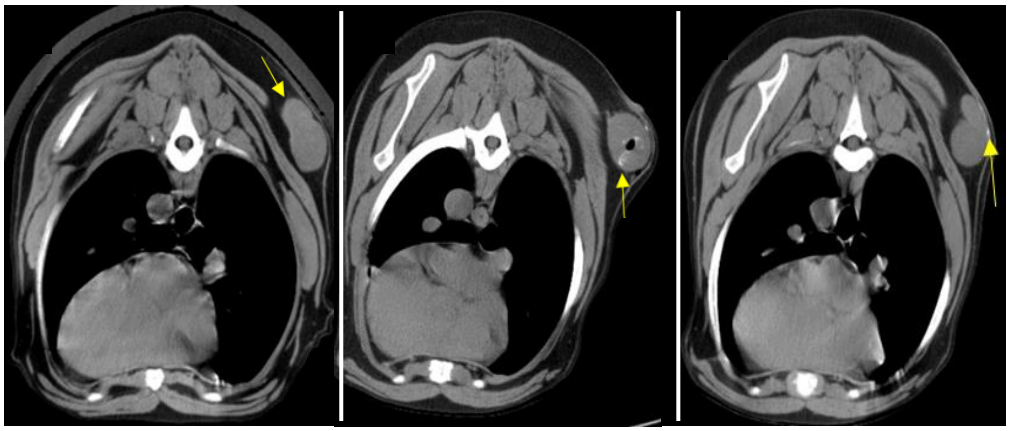

Figure 3.10. *CT Images of Canine Sarcoma* (A) 1-month Pre-treatment CT scan, arrow indicates tumor (B) 30-minute Post-NP Injection CT Scan, arrow indicates Fol-RLNPs (bright, hyperattenuating regions) (C) 1-month Post-treatment CT Scan, arrow indicates Fol-RLNPs (bright, hyperattenuating regions). For this case study, the tumor was injected with 3.3 mL of Fol-RLNPs at 10 mg/mL suspension in PBS. Note: Unfiltered particles were used for this study.

Table 3.1. Computerized Tomography (CT) Tumor Measurements

Date	Cranial-Caudal	Dorsal-Ventral	Medial-Lateral	Sum Diameter	CT Calculated Volume
1 Month Pre-treatment	3.96 cm	4.47 cm	2.13 cm	10.56 cm	22.40 cc
30 Min. Post-injection	5.45 cm	4.00 cm	3.05 cm	12.50 cm	33.31 cc
1 Month Post-treatment	3.50 cm	4.24 cm	2.54 cm	10.28 cm	16.78 cc

Histology slides from the canine tumor were prepared using hematoxylin and eosin (H&E) staining for pre- and post-treatment biopsies. Images taken of these slides were examined and sample images are displayed in Figure 3.11. The pre-treatment biopsy (taken approximately 3 weeks prior to treatment) indicated a soft-tissue sarcoma derived primarily from malignant peripheral nerve sheath tissue. In-treatment biopsies from the Fol-RLNP injection side as well as the un-injected side (taken on day 3 of treatment) displayed no visible neoplasia. These sections exhibited variably sized regions of inflamed adipose tissue, connective tissue, and muscle tissue. In the treatment slides, aggregates of the injected particles created dark regions in the images.

While there was no visible neoplastic tissue, it is likely that this was due to the location from where the biopsy sample was taken. The deeper tissue underlying biopsy tissue likely still contained neoplastic regions. The inflammation in the biopsies consisted primarily of neutrophils, with a smaller number of lymphocytes, plasma cells, and macrophages. The presence of immune cells is indicative that the combination of Fol-RLNPs and X-ray therapy is effective in inducing a significant inflammatory response even with a low-dose, palliative radiation treatment plan. The similarity between the injected and un-injected sides is likely due to the induced immune response producing anti-tumor effects throughout the entire tumor.

The animal patient involved in this study was returned by the owners for euthanasia and subsequent necropsy for humane reasons at approximately 19 months post-treatment.

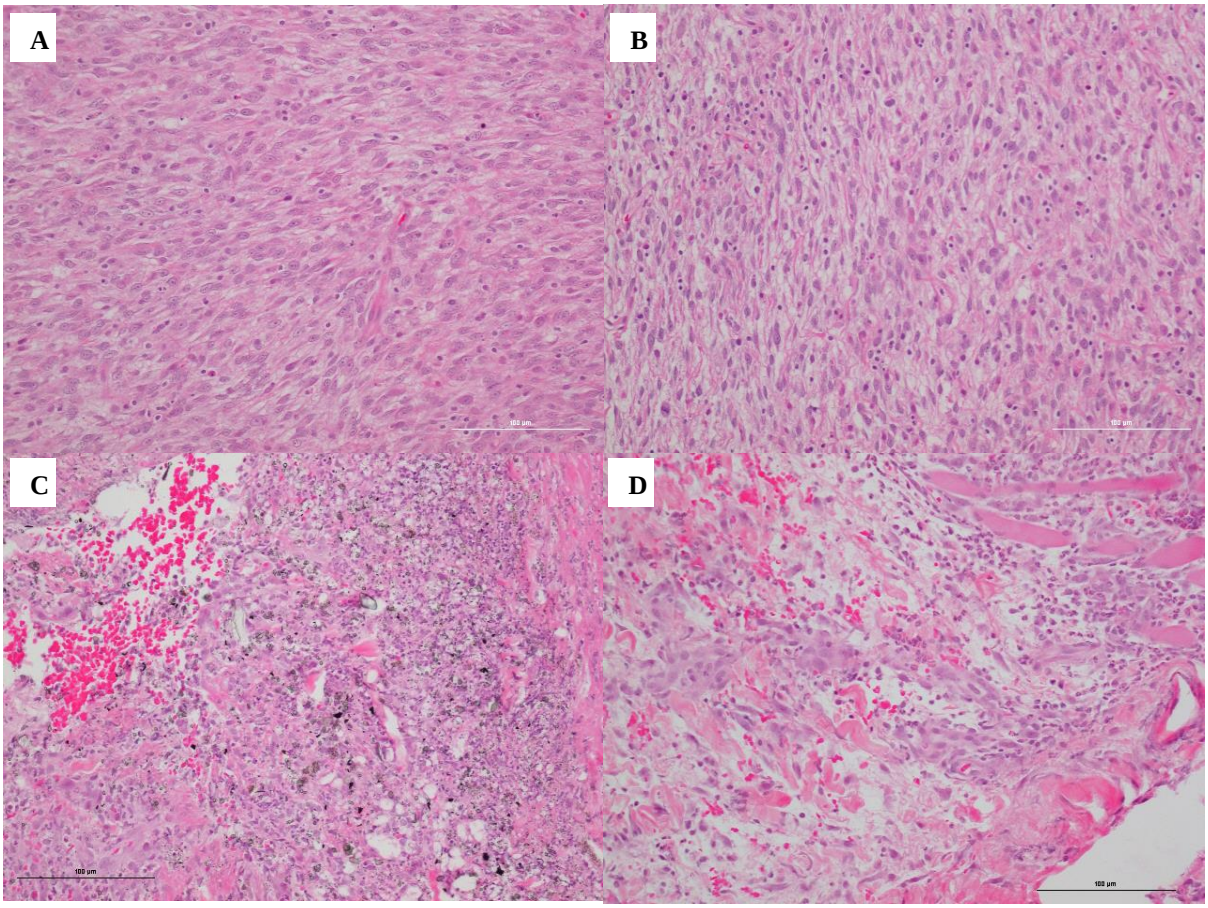

Figure 3.11. *Histopathology of Sarcoma Biopsies Pre-/Post-treatment* (A) Pre-treatment H&E slide. (B) Pre-treatment H&E slide (2nd location). (C) In-treatment (Fol-RLNP injection side). (D) In-treatment (un-injected side). Panels (A) and (B) indicate soft tissue sarcoma of nerve sheath tissue origin. Panels (C) displays mesenchymal tissue judged to be fibrosis. The mesenchymal tissue was markedly inflamed, and variably sized (pinpoint or 8 to 15-micron diameter) black-pigmented material was scattered or clumped within the mesenchymal tissue (likely nanoparticle clusters). Weakly birefringent, irregularly shaped to round, yellow to clear crystals were also scattered or clumped within the tissue. Panel (D) displays a tissue section comprised of markedly inflamed adipose tissue and muscle, infiltrated and dissected by bands of inflamed granulation tissue with no tumor identified. "Inflamed" refers to the presence of neutrophils and/or lymphocytes and plasma cells. Scale bar in each image is 100 µm. Note: Unfiltered particles were used for this study.

Taken together, these experiments demonstrate that RLNPs and Fol-RLNPs exhibit radio-sensitization properties *in vitro*, but Fol-RLNPs significantly outperform both X-ray therapy alone and RLNPs + X-rays in murine cancer models. The cause of the increase in radio-sensitizer efficacy for Fol-RLNPs is likely due to pro-proliferative signaling initiated by folate's inherent mitogenic activity that leads to increased UV-A cell sensitivity, possibly due to decreased repair of UV-A induced DNA lesions like double strand breaks. From the data in these experiments, it is

evident that Fol-RLNPs combined with X-ray radiation can act as effective radio-sensitizers and clearly outperform RLNPs.

Fol-RLNPs exhibit useful radio-sensitizer properties in a variety of contexts, including a spontaneous tumor in a canine patient. The canine clinical case study demonstrated that Fol-RLNPs could play a potential role in the treatment of spontaneous tumors, particularly those which are normally considered radio-resistant. However, because this case study involved only one patient, further examination in a larger patient population is necessary to confirm this observation. Ultimate translation of Fol-RLNPs would require a significantly larger patient population to demonstrate efficacy and safety in a statistically significant manner.

Nonetheless, Fol-RLNPs could possibly be used to sensitize tumors such that they could receive lower total radiation doses or be used to improve tumor control probability at a given radiation dose. Importantly, these radio-sensitization effects are only present in the tumor tissue because of the intra-tumoral delivery of the particles in addition to their propensity to stay within the tumor tissue post-injection. Overall, Fol-RLNPs are effective radio-sensitizers that warrant further investigation into their viability for clinical use. Future studies will include optimization of Fol-RLNPs using murine cancer models and an expanded canine clinical trial in multiple dogs with spontaneous tumors.

3.5 Conclusions

This study demonstrates that RLNPs and Fol-RLNPs function as radio-sensitizers when combined with X-ray radiation therapy of head and neck cancer cells. Fol-RLNPs exhibit enhanced efficacy compared to RLNPs in cell culture and animal models by increasing cancer cell sensitivity to UV-A radiation. Several mechanisms were explored for this Fol-RLNP-mediated increase in efficacy, including improved uptake efficiency, altered sub-lethal damage repair kinetics, changes

in intracellular photosensitizer concentrations, and decreased repair capability in response to folate's induction of pro-proliferative signaling via its innate mitogenic activity. The data suggested that Fol-RLNPs enhanced efficacy relative to RLNPs is likely caused by Fol-RLNP-initiated pro-proliferative signaling that leads to decreased repair of UV-A-induced DNA lesions (i.e. double strand breaks). Fol-RLNP-treated cells must split efforts between DNA lesion repair and amplification of proliferative signaling, potentially leading to diminished repair capacity for DNA lesions and subsequent increases in lethal chromatin aberrations and clonogenic cell death. A mouse head and neck cancer xenograft experiment confirmed that the efficacy improvements of Fol-RLNPs over RLNPs are present in vivo. The canine clinical study described herein suggests that Fol-RLNPs may function as effective radio-sensitizers in spontaneous animal tumors as well, but further clinical study is needed to confirm these observations. Together, these experimental results indicate that Fol-RLNPs have potential to be used as a radio-sensitizer for radiation therapy, but further exploration is required and warranted to optimize their radio-sensitization properties and confirm their safety and efficacy for potential clinical translation.

Acknowledgements

Funding for this research was provided by Purdue Office of the Executive Vice President for Research and Partnerships (OEVPRP) (New NIH R01 Program), Indiana Clinical and Translational Sciences Institute (CTSI) (Collaboration in Translational Research (CTR) Pilot Grant Program), Purdue University Center for Cancer Research (PCCR, P30CA023168) (SIRG Graduate Research Assistantship, Shared Resource Biological Evaluation Project, and Phase I Concept Award), Lodos Theranostics LLC (Gift Grant), and the School of Chemical Engineering at Purdue University. The HN31 cell line was generously provided by Dr. Jeffrey N. Myers at the MD Anderson Cancer Center.

Financial Conflict of Interest

A company, Lodos Theranostics LLC, is currently attempting to commercialize the technology in this manuscript. The corresponding author, You-Yeon Won, has an ownership interest in this company.

4. BILIRUBIN-COATED RADIO-LUMINESCENT PARTICLES AND THEIR USE FOR RADIATION-INDUCED PHOTODYNAMIC THERAPY

Vincenzo J. Pizzuti[†], Dhushyanth Viswanath[†], Sandra E. Torregrosa-Allen[‡,‖], Melanie P. Currie[‡,‖], Bennett D. Elzey[‡,‖], and You-Yeon Won*[,†,‡]

[†]Davidson School of Chemical Engineering, [‡]Purdue University Center for Cancer Research, [‖]Department of Comparative Pathobiology, Purdue University, West Lafayette, Indiana 47907, United States
*Corresponding author

4.1 Abstract

Photodynamic therapy (PDT) has shown potential as a cancer treatment modality, but its clinical application is limited due to its visible light activation since light cannot penetrate tissues well. Additionally, combination therapies utilizing PDT and radiotherapy have shown clinical promise in several cancers but are limited again by light penetration and the need for selective photosensitization of the treatment area. Herein we report the development of bilirubin-photodynamic nanoparticles (BR-PDNPs). BR-PDNPs are a novel formulation of PEGylated bilirubin micelles encapsulating $CaWO_4$ nanoparticles. These particles are capable of activating PDT via X-ray irradiation within deep tissues due to the radio-luminescent properties of their $CaWO_4$ nanoparticle cores. BR-PDNPs facilitate a combination of photodynamic and radiation therapy and represent a new application of previously developed PEG-bilirubin conjugates. When irradiated by X-rays, BR-PDNPs emit UV-A and visible light from their $CaWO_4$ cores which excites bilirubin and leads to the production of singlet oxygen. BR-PDNPs exhibit improvements over X-ray therapy alone in *in vitro* and in murine xenograft models of head and neck cancer. The data presented in this study suggest that BR-PDNPs are a promising agent for facilitating combined radio-photodynamic therapy in deep tissue tumors.

TOC Graphic:

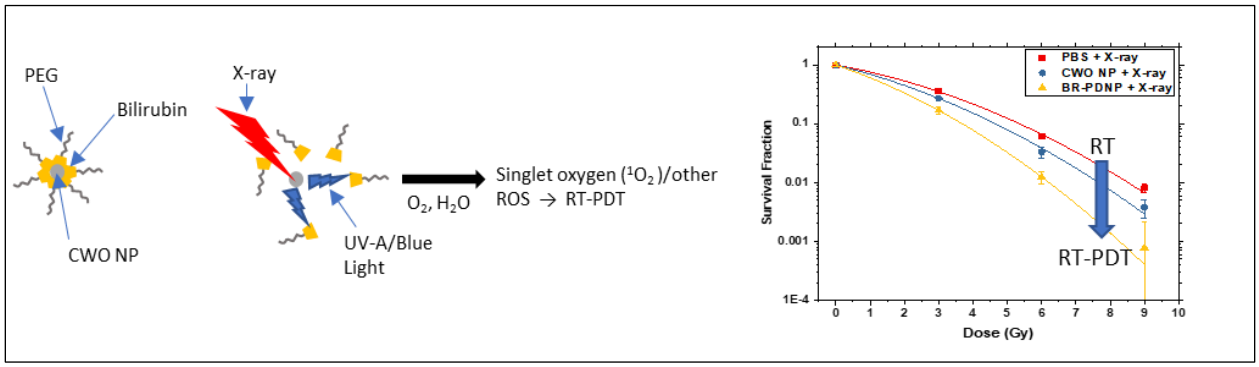

4.2 Introduction

Bilirubin (BR) is a downstream product of heme catabolism in mammals[71]. Free heme groups from degraded hemoglobin are metabolized to remove them from systemic circulation and subsequently are converted into BR. As previously reported, BR is capable of photosensitizing cells to light, making them more susceptible to damage and death from light exposure[72]. This photo-activity is due to the production of reactive oxygen species (ROS) when BR is exposed to UV-A and visible-spectrum wavelengths of light, predominantly singlet oxygen ($^1O_2$)[73]. This singlet oxygen exerts the majority of the therapeutic effects in photodynamic therapy[74].

Photodynamic therapy (PDT) is a relatively new modality for cancer treatment that has clinical potential[75,76]. PDT relies on oxygen, light, and a photosensitizer to function[53]. Photosensitizers are compounds that produce cytotoxic ROS when exposed to specific wavelengths of light, but are otherwise pharmacologically inactive[77]. Because of this activation pathway, PDT typically displays low systemic toxicity and minimal acquired resistance[78]. One major limitation of PDT is that it cannot treat tumors deeper than the surface level because of the short penetration depths of light in tissue[79]. Thus, only tumors of the skin or surface linings of the

esophagus, lung, or bladder can be treated[80,81]. To address this issue, we report a novel bilirubin-PEG encapsulated $CaWO_4$ (CWO) nanoparticle system (bilirubin-photodynamic nanoparticles, BR-PDNPs) that acts as an X-ray inducible PDT platform. Because X-ray photons have much better penetration depths into tissue, they can overcome the limitations of visible light. Thus, this system could be used to treat locally advanced primary or recurrent lesions anywhere within the body. Additionally, because the platform is X-ray activated, the system acts as a combination radiotherapy and photodynamic therapy, a combination that has shown promising results[33,82,83].

One disease that could benefit from radiotherapy and PDT combination is head and neck squamous cell carcinoma (HNSCC). HNSCC is the 6th most common cancer worldwide[43], and the overall 5-year survival rate is around 50% for all HNSCC patients[44]. It has relatively high incidence of recurrence post-radiotherapy[2,45], with the rate of recurrence up to 60% for local failure and 30% for distant failure[2]. This is an issue considering that radiation therapy is a primary treatment modality for most cases of HNSCC[46]. The combination of PDT and radiation therapy could potentially show improved clinical responses in patients with HNSCC since the two therapies operate through separate ROS generation mechanisms[84], but this strategy is still limited in that PDT is only an option for tumors on surfaces of the nose, mouth, and throat. The BR-PDNPs overcome this because their X-ray activation allows the system to be actuated even below the surfaces of tissues, allowing for radiation therapy and PDT combinations in large or deep-seated tumors.

Typically, drugs used to treat cancers are systemically administered, causing off-target toxicities[59,4]. Intratumoral injection is a clinically viable drug delivery method for cancer therapies that helps to overcome this limitation because the drug is only applied to the diseased tissue. In the case of BR-PDNPs, intratumoral injection ensures good localization of treatment since the

therapeutic effects are only activated by the external X-ray source, which is focused on the tumor itself. In this way, this system is specific for diseased tissues and minimizes off-target toxicity.

The novel BR-PDNP system described in this report consists of a $CaWO_4$ nanoparticle (CWO NP) core encapsulated by a poly(ethylene glycol)-bilirubin conjugate micelles (PEG-BR micelles). When conjugated to PEG, bilirubin can intramolecularly hydrogen bond, creating a hydrophobic domain that drives the assembly of micelles in aqueous medium[85]. When exposed to UV-A/blue wavelengths of light, bilirubin undergoes rearrangement that disrupts the extensive intramolecular hydrogen bonding network, thus eliminating its hydrophobicity. This loss of hydrophobic character ultimately causes the PEG-BR micelles to dissociate[85]. Previous work has been conducted by Jon and coworkers using PEG-BR micelles, taking advantage of these photo-activatable properties, with a focus on their use for controlled release of drugs and diagnostic use potential[86,87]. In BR-PDNPs, we have devised a new application for PEG-BR when combined with the radio-luminescent properties of CWO NPs. BR-PDNPs employ the previously described dissociation of PEG-BR micelles in addition to bilirubin's innate photo-sensitizing capabilities to facilitate the activation of combined PDT and radiation therapy. In vitro efficacy testing demonstrated clear therapeutic enhancements in combining BR-PDNPs with X-ray radiotherapy. Furthermore, a head and neck cancer xenograft experiment in mice suggested that these combined radio/photodynamic therapy enhancements are present *in vivo*, but further study is needed to confirm these results. BR-PDNPs represent a novel tool for combining radiation and photodynamic therapies for solid tumors, and further optimization of the formulation and efficacy validation in other tumor models are warranted to examine their ultimate translational viability.

4.3 Materials and Methods

Synthesis and Characterization of PEGylated bilirubin (PEG-BR)

The poly(ethylene glycol)-bilirubin (PEG-BR) polymer-conjugate was synthesized as previously described, with some modification[85]. Briefly, 0.5 mmol of bilirubin (BR) and 0.5 mmol of N,N'-dicyclohexylcarbodiimide (DCC) with 0.5 mmol of N-hyrdoxysuccinimide (NHS) were dissolved in 5 mL of dimethyl sulfoxide (DMSO) and allowed to stir for 10 minutes at room temperature. Then, 0.2 mmol of HO-PEG2000-NH_2 (Laysan Bio) and 150 μL of triethylamine (TEA) was added to the mixture and allowed to stir for 4 hours at room temperature under a nitrogen or argon atmosphere (synthesis vessel covered to protect it from light). Then 45 mL of methanol was added to the reaction vessel to precipitate free bilirubin (unconjugated BR). The mixture was then centrifuged at 5,000 rpm for 10 minutes, and the supernatant was removed for processing while the precipitate was discarded. The supernatant was then syringe filtered using a 450 nm PTFE filter to remove residual free BR and was then placed under vacuum to concentrate the mixture. The mixture was then dialyzed against Milli-Q filtered water for 2 days using a regenerated cellulose membrane with a MWCO of 1 kDa. The resultant suspension was then lyophilized, and the powder analyzed using ^{1}H-NMR. For NMR characterization, 5 mg of as-synthesized PEG-BR was dissolved in deuterated DMSO (DMSO-d6) and the spectrum acquired on a Bruker DRX-500 machine.

Formulation of PEG-BR Micelles and PEG-BR Photodynamic Nanoparticles (BR-PDNPs)

For PEG-BR micelles, 10 mg of PEG-BR was dissolved in chloroform and subsequently dried under argon or nitrogen gas and then allowed to dry under vacuum for 4 hours. Then, 10 mL of phosphate buffered saline (PBS) was added to the dried PEG-BR and then sonicated for 5 minutes.

For PEG-BR photodynamic nanoparticles (BR-PDNPs), 30 mg of PEG-BR was dissolved in 3.9 g of N,N-dimethylformamide (DMF). Then 50 μL of 10 mg/mL calcium tungstate nanoparticles (synthesized as described previously[88]) was added to the solution, the vial was placed in a sonication bath and an overhead disperser was placed into the mixture and set to rotate at 10,000 rpm. After the initiation of stirring, 2.1 mL of PBS was added to the suspension and allowed to mix for 5 minutes. The resultant solution was removed from the setup and centrifuged for 10 minutes at 5,000 rpm. The supernatant was removed, and the pellet resuspended in PBS with an amount corresponding to the desired final concentration. This mixture was then vortexed for 30 seconds to complete the resuspension. These particles were then filtered using a 450 nm PTFE syringe filter.

NP Size Characterizations

Transmission electron microscopy (TEM) was conducted on BR-PDNPs to visualize the as formulated particles. Images were taken using a Tecnai T20 instrument using 2% uranyl formate as a negative staining agent.

Hydrodynamic size measurements were conducted using dynamic light scattering (DLS). For DLS preparation, BR-PDNPs were diluted to a concentration of 0.25 mg/mL (based on $CaWO_4$, CWO) and filtered as described above. N = 3 separate batches were prepared and measured.

UV Dissociation Characterization of PEG-BR PDNPs

A UV-A lamp (peak emission at 365 nm) was used to illuminate BR-PDNPs formulated as described above at a final concentration of 0.1 mg/mL (based on CWO) for a total UV fluence of 0.56 J/cm^2 (or 1.12 J/cm^2 for the sample exposed to two subsequent doses). DLS size measurements were conducted immediately after formulation, after one UV dose, and after two UV doses (N = 2 separate experiments).

Singlet Oxygen Production Quantification

Singlet Oxygen Sensor Green (SOSG, ThermoFisher) was dissolved into a methanol stock solution at a concentration of 5 mM. Then, aqueous dilutions of SOSG to a concentration of 10 μM and CWO NPs/BR-PDNPs to a concentration of 0.1 mg/mL (based on CWO NP concentration) were loaded into the wells of a 96 well plate. Two separate sets of samples were prepared for irradiated groups (to measure singlet oxygen production under X-ray) and unirradiated groups (to measure background fluorescence signals as negative controls). Irradiated samples were dosed with 2, 3, or 6 Gy of X-ray at a dose rate of 2 Gy/min (320 kV XRAD-320, Precision X-ray). Both sets of samples were kept protected from all other illumination sources until time of fluorescence measurement. Sample wells in irradiated and unirradiated plates were read using a Bio-RAD Microplate Reader-550 using 500 nm excitation and 525 nm emission endpoints. N = 4 per group.

MTT Cell Viability Assay

HN31 cells were seeded in a 96-well tissue culture plate at a density of 0.5×10^4 cells per well and incubated for 24 hours at 37.0 °C in a 5% CO_2 incubator prior to exposure to CWO NPs. Cells were then treated with various concentrations of PEG-BR<??>-coated and uncoated CWO NPs (0.1, 0.2, 0.5, 1.0 and 2.0 mg CWO per mL solution) (N = 4). After 24 hours of incubation, 10 μL of the MTT reagent (Sigma) was added to each well and incubated for additional 4 hours. Resultant formazan crystals were dissolved by first removing all liquid in each well and then adding 150 μL of DMSO (Sigma) to each well. The absorbances at 570 nm and 630 nm (for background subtraction) were immediately measured using a microplate reader (BIO-RAD Microplate Reader-550). The wells containing cells (that had not been treated with CWO NPs) in the medium with the MTT reagent were used as controls for 100% viability reference.

Clonogenic Cell Survival Assays

The clonogenic cell survival assay was conducted as previously described[89]. Briefly, HN31 cells (courtesy of Dr. Jeffrey N. Myers at MD Anderson Cancer Center) were used as a cellular model for head and neck squamous cell carcinoma. HN31 cells were cultured in Dulbecco's Modified Eagle Medium (DMEM) supplemented with 10% (v/v) fetal bovine serum (FBS) and 0.1% L-glutamine (Gibco Life Technologies) (as recommended by American Type Culture Collection (ATCC)) in a humidified incubator with 5% CO_2 at 37.0 °C. HN31 cells were grown in a T-25 cell culture flask until they reached ~ 80% confluence. After this, the growth medium was removed, and the adherent cells were washed with PBS (Gibco Life Technologies). Cells were then detached from the plates by treatment with TrypLE™ Express (1×) solution for 4 – 6 minutes at 37.0 °C. Detached cells, suspended in growth medium/TrypLE Express mixture, were centrifuged at 300× g for 5 minutes at room temperature. The cell pellet was resuspended in a minimal amount of growth medium (2 – 3 mL), and the cells were counted using a hemocytometer.

Cells were then seeded into 6-well plates at densities varying with planned radiation dose, as follows: 0.2×10^3 cells/well for 0 Gy, 0.8×10^3 cells/well for 3 Gy, 1.6×10^3 cells/well for 6 Gy, and 5.0×10^3 cells/well for 9 Gy. Three experimental groups were tested with N = 3 wells/group: PBS-treated + X-ray, PEG-BR Micelles + X-ray, and BR-PDNPs + X-ray. PEG-BR micelles were diluted in growth medium to a concentration of 0.2 mg/mL (based on polymer concentration), BR-PDNPs were diluted in growth medium to 0.2 mg/mL (based on CWO concentration), and PBS was added to an equivalent volume fraction as the experimental groups in growth medium. These prepared doses were added to their respective wells and allowed to incubate at 37.0 °C with the cells for 4 hours and the plates were then exposed to the appropriate dose of X-ray radiation at a dose rate of 2 Gy/minute (320 kV XRAD-320, Precision X-ray).

Irradiated cells were cultured for 14 days. Colonies resulting from radio-resistant cells were stained with Crystal Violet. Colonies of more than 50 daughter cells in culture were counted (N = 3). Results were compared with un-irradiated controls to calculate survival fraction.

Murine HN31 Xenograft Efficacy Evaluation

Female Nod rag gamma (NRG) mice (8 weeks old) were housed in a pathogen-free environment including standard cages with free access to food and water and an automatic 12 h light/dark cycle. The mice were acclimated to the facility for 1 week prior to beginning experiments, and all animals were cared for according to guidelines established by the American Association for Accreditation of Laboratory Animal Care (AAALAC). Subcutaneous HNSCC xenografts were produced by inoculation of 1.5 x 10^6 HN31 cells in 0.1 mL total volume of a serum free medium containing 50% Matrigel (BD Bioscience). Intratumoral nanoparticle injection at 10 mg/cc tumor of CWO NP in sterile PBS was conducted once tumors reached ~ 100 mm^3, approximately 6 days after inoculation, and split into two equal injections on consecutive days. For this study, the following treatment groups were used: BR-PDNP + X-ray, CWO NP + X-ray, and PBS + X-ray; BR-PDNP, CWO NP, and PBS. Radiation treatments were conducted the second day of injection and the subsequent day (2 Gy each) for a total of 4 Gy at a dose rate of 2 Gy/min using a 320 kVp laboratory X-ray irradiator (X-RAD 320, Precision X-ray, North Branford, CT). Tumors were measured with digital calipers in three dimensions: length (L), width (W), and height (H). Tumor volumes were calculated using $V = (L \times W \times H) \times \pi/6$. N = 8 per group. Euthanasia criteria were > 20% body weight loss or tumor volume > 2000 mm^3. Mice were euthanized via spinal dislocation under anesthesia. Tumors were excised and weighed post euthanasia. All major organs (brain, heart, lungs, kidneys, spleen, liver) and tumors were excised and placed in 10% neutral-buffered formalin phosphate. Representative animal organs from each treated group were

then embedded in paraffin, sectioned, stained with standard H&E staining, and digitized with a brightfield digital microscope camera at a zoom of 20x.

4.4 Results and Discussion

Bilirubin photodynamic nanoparticles (BR-PDNPs) are thought to potentiate photodynamic therapy under X-ray irradiation through distinct steps. X-ray exposure causes $CaWO_4$ (CWO) nanoparticles at the core of the BR-PDNPs to emit UV-A and blue light, as described previously[88]. This UV-A/blue light is absorbed by the bilirubin in PEG-BR, and the absorption disrupts intramolecular hydrogen bonds that cause bilirubin to act as a hydrophobic molecule. The disruption of this network causes the PEG-BR micelles encapsulating the CWO nanoparticle to dissociate, leading to free BR-PEG chains and bare CWO nanoparticles in suspension. After this dissociation, CWO will continue emitting UV-A/blue light, which will interact with the bilirubin in the liberated PEG-BR chains. Excited bilirubin in the liberated chains can interact with intracellular molecular oxygen, and reactive oxygen species (ROS) are produced, predominantly singlet oxygen ($^1O_2$). Singlet oxygen effects combined with X-ray cellular damage can potentially improve the efficacy of X-ray treatments for cancers. This mechanism is outlined below in Figure 4.1.

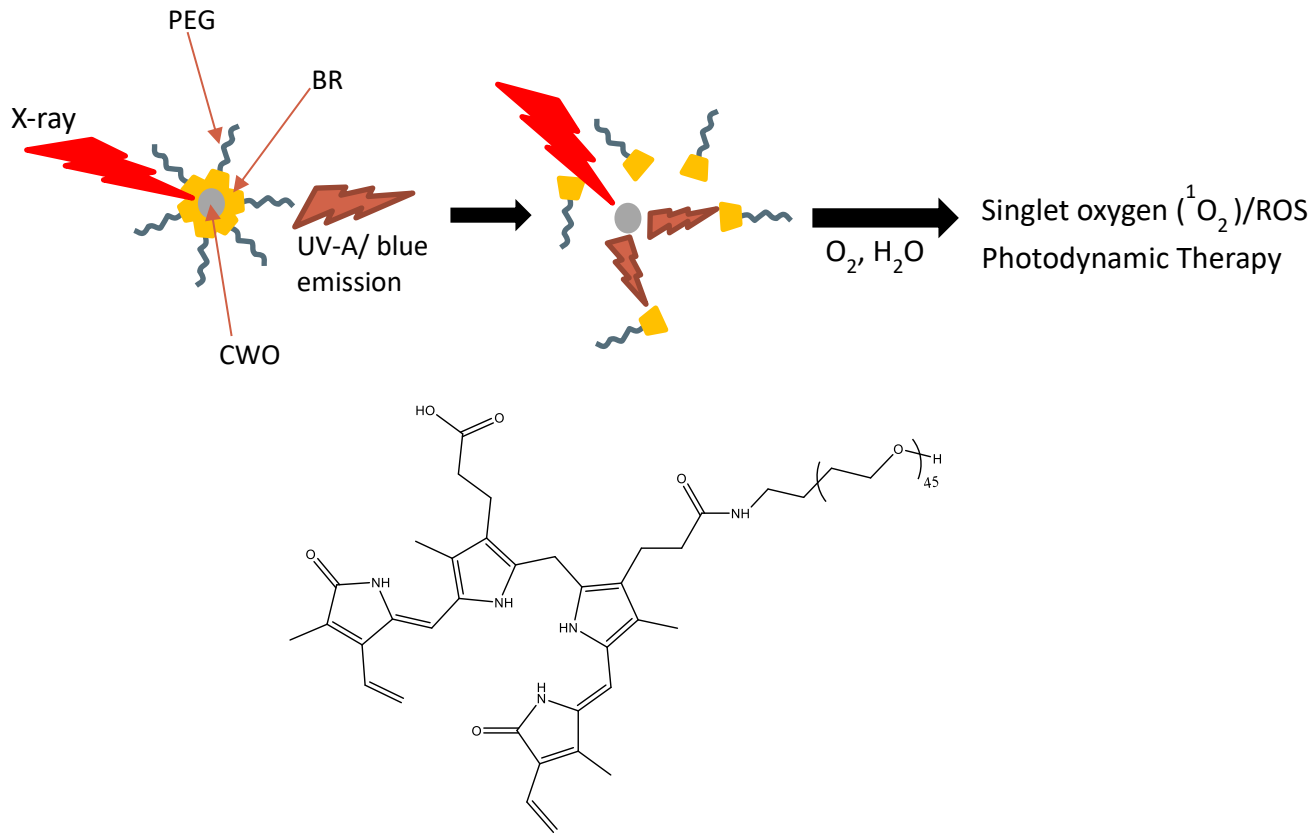

Figure 4.1 *Schematic Overview of BR-PDNP Mechanism of Action.* The top of the figure is a schematic diagram for the mechanism of BR-PDNPs. The structure of the PEG-BR conjugate is displayed on the lower portion of the figure.

Synthesis and Characterization of BR-PDNPs

PEG-BR was synthesized from an amine-PEG precursor. The product was then purified, and the resultant compound was characterized via ^{1}H-NMR to confirm the structure of the product. The ^{1}H-NMR spectrum of the as-synthesized PEG-BR product is displayed in Supplemental Material in Figure 4.S1. PEG-BR was then used to encapsulate $CaWO_4$ nanoparticles (CWO NPs) as described in the Materials and Methods. PEG-BR-encapsulated CWO NPs (BR-PDNPs) were then visualized using TEM with 2% uranyl formate as a negative stain. A representative image of filtered BR-PDNPs is shown in Figure 4.2.

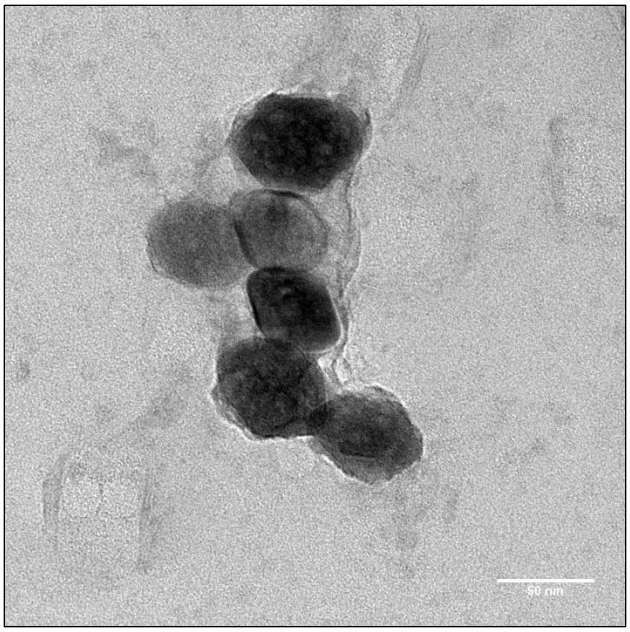

Figure 4.2. *TEM Micrograph of BR-PDNPs.* Filtered BR-PDNPs in PBS suspension were air-dried onto a TEM grid and negatively stained with 2% uranyl formate. Several images of the particles were taken, and a representative image is displayed above. As is visible in the micrograph, filtered BR-PDNPs are predominantly comprised of small clusters of CWO NPs (dark particles) encapsulated by PEG-BR (lighter gray region surrounding particle cluster). Scale bar = 50 nm.

The sizes of PEG-BR micelles and BR-PDNPs were characterized via dynamic light scattering (DLS). These results are consistent with the idea that PEG-BR micelles effectively encapsulate CWO nanoparticles. Note that the unfiltered BR-PDNPs effective diameter was larger likely due to large agglomerates of un-encapsulated CWO that may have been present in the sample before filtration. The results of the DLS size measurements are shown in Figure 4.3.

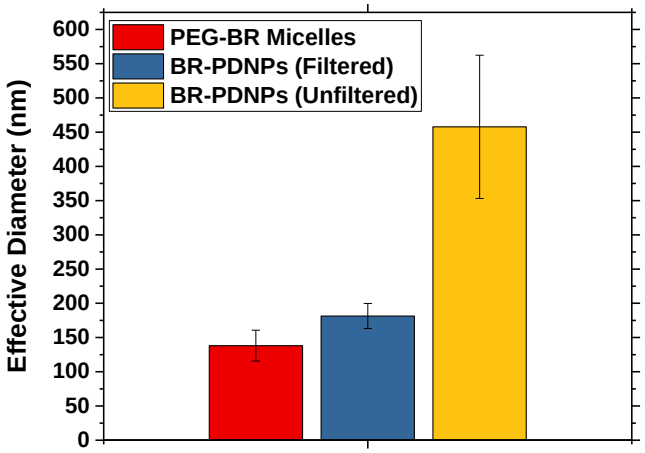

Figure 4.3. *DLS Size Data for PEG-BR Micelles and BR-PDNPs.* PEG-BR micelles and BR-PDNPs were suspended at 0.2 mg/mL concentration in PBS (mass of polymer and CWO for micelles and PDNPs, respectively) and analyzed using DLS at room temperature. Filtered sample passed through 450 nm PTFE syringe filter, as described in the methods. Effective diameters represent average values and error bars represent standard deviation (N = 3).

DLS size measurements of filtered BR-PDNPs were conducted before and after exposure to UV-A radiation from a lamp to confirm that UV-A exposure can cause dissociation of the PEG-BR micelles encapsulating the CWO nanoparticles. As seen in Figure 4.4, UV-A exposure leads to an increase in effective diameter for the BR-PDNP sample, and the size increased again after a subsequent UV-A dose. The increase in the effective diameter in this sample is caused by the agglomeration of bare CWO nanoparticles that are exposed when the PEG-BR micelles dissociate. This data supports the proposed mechanism of action of BR-PDNPs.

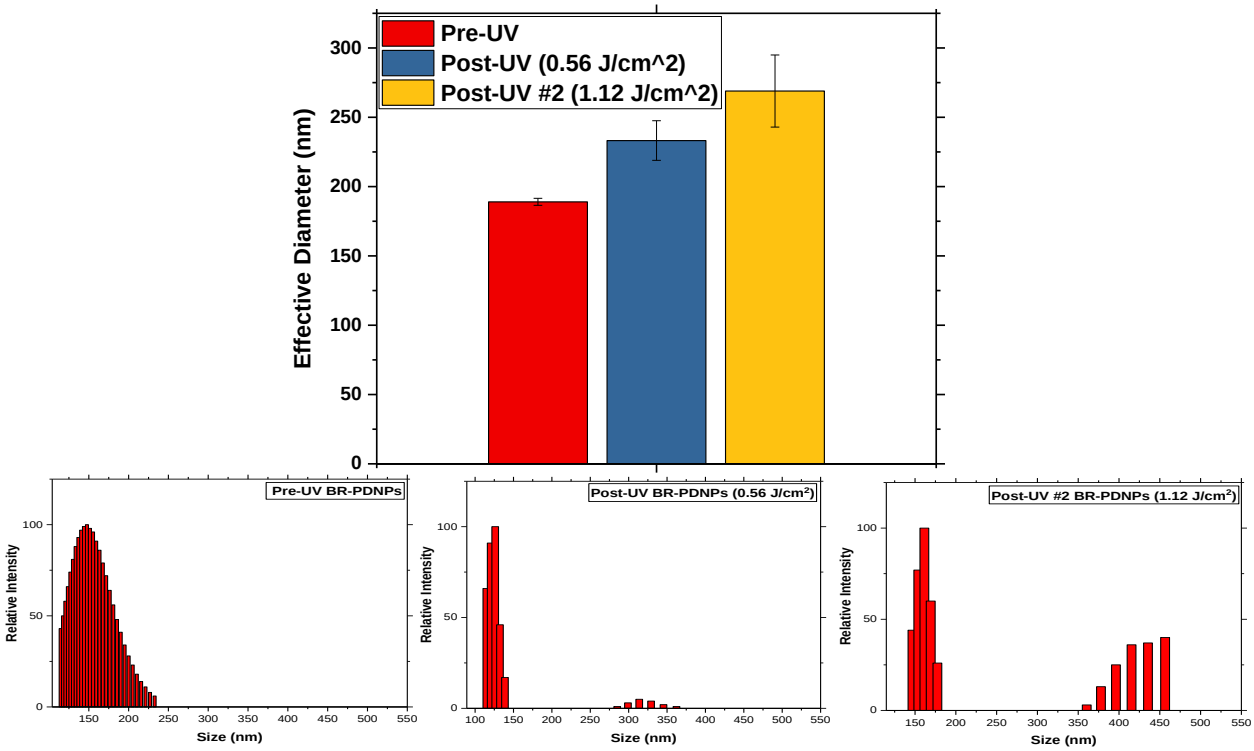

Figure 4.4. *DLS Size Data for UV-exposed BR-PDNPs.* A UV-A lamp (peak emission at 365 nm) was used to illuminate BR-PDNPs at a concentration of 0.1 mg/mL (based on CWO) for a UV fluence of 0.56 J/cm^2 or 1.12 J/cm^2. DLS size measurements were conducted immediately after formulation, after one UV dose, and after two UV doses. (Top) The increase in effective diameter is indicative of PEG-BR micelle dissociation and release of bare CWO NPs, which then aggregate in suspension to increase the number of large particles and thus increase the effective diameter of all particles in the sample. Error bars represent standard deviation (from N = 2 separate batches). (Bottom) This trend can be seen in the representative histograms presented. As UV exposure dose increases, an increasing number of larger aggregates are observed via DLS number-weighted size histogram output. Note: Experiment conducted using filtered particles.

To further explore the mechanism of BR-PDNPs, an experiment was conducted to quantify and compare the generation of singlet oxygen ($^1O_2$), a specific type of reactive oxygen species produced via a type II photosensitizer reaction with molecular oxygen[20]. Relative amounts of Singlet Oxygen Sensor Green (SOSG) fluorescence were compared for PBS, CWO NPs, and BR-PDNPs after X-ray radiation at several doses. The results of this experiment are displayed in Figure 4.5. The data from the plot suggest that BR-PDNPs efficiently generate singlet oxygen in response to X-ray irradiation and do so at an elevated level when compared to PBS or CWO NPs in combination with X-rays.

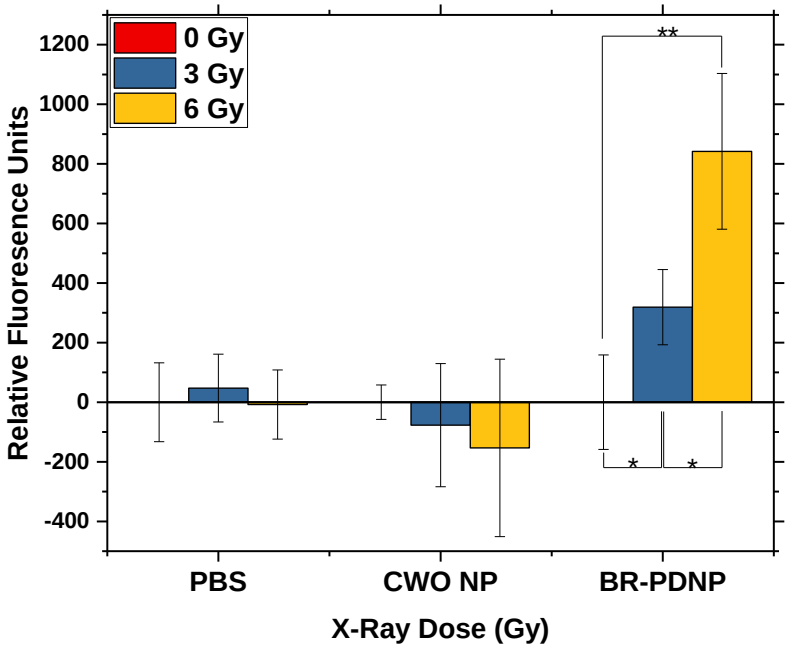

Figure 4.5. *Singlet Oxygen Production Quantification.* Singlet Oxygen Sensor Green (SOSG) was diluted in MilliQ water to a concentration of 10 μM in the wells of a 96-well plate containing suspensions of PBS, CWO NPs, and BR-PDNPs at a concentration of 0.2 mg/mL (based on saline or CWO NP concentration). Two separate sets of samples were prepared for irradiated groups (to measure singlet oxygen production under X-ray) and unirradiated groups (to measure background fluorescence signals as negative controls). Irradiated samples were dosed with 0, 3, or 6 Gy of X-ray at a dose rate of 2 Gy/min. Both sets of samples were kept protected from all other illumination sources until time of fluorescence measurement. Sample wells in irradiated and unirradiated plates were read using 500 nm excitation and 525 nm emission endpoints. N = 4 per group for irradiated samples and N=3 per group for unirradiated samples. Single asterisks denote $p < 0.05$ and double asterisks denote $p < 0.01$ as calculated using student's t-test. Note: Experiment conducted with unfiltered nanoparticles.

Biological Evaluation of BR-PDNPs

The proposed mechanism for BR-PDNPs relies on the idea that the nanoparticles are only activated when illuminated. It then follows that once BR-PDNPs are intratumorally injected, only X-ray radiation should be capable of activating the therapeutic effects of the particles. By preventing unwanted activation of NPs, this system is designed to mitigate off-target toxicity. To examine the extent to which BR-PDNPs are cytotoxic in the "dark" (i.e., un-irradiated), an MTT cell viability assay was conducted at various concentrations and compared to un-encapsulated CWO NPs. The results of this experiment are displayed in Figure 4.6. As seen in the figure, cell

viability remains high until reaching a concentration about an order of magnitude higher than used for therapeutic cell culture treatments (0.1 – 0.2 mg/mL vs. 1.0 mg/mL). This supports the idea that BR-PDNPs are minimally toxic at standard treatment concentrations.

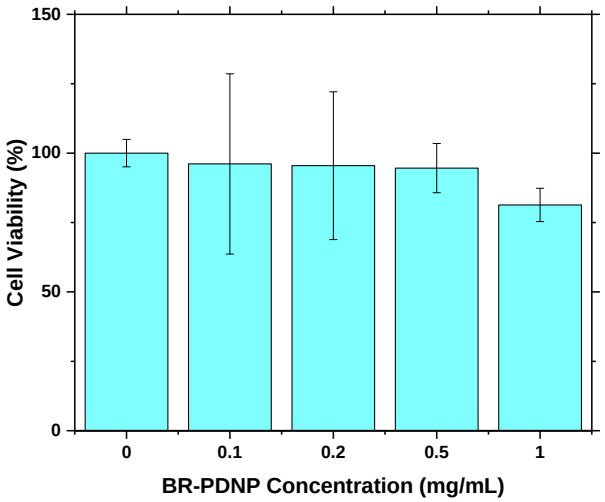

Figure 4.6. *Cell Viability with Exposure to BR-PDNPs.* Cell viability measured by MTT assay with exposure to BR-PDNPs at displayed concentrations (based on CWO NP). HN31 cells were seeded in 96-well tissue culture plates at a density of 1.0 x 10^4 cells per well and incubated for 24 hours. MTT cell viability assay was performed at 24 h post treatment. 0 mg/mL represents the negative control for these experiments. All error bars represent standard deviation (N = 4). Note: Experiment conducted using unfiltered particles.

Next, a series of clonogenic cell survival assays were conducted to examine and compare the efficacy of X-ray radiation alone versus X-ray radiation in combination with PEG-BR micelles, CWO NPs, and BR-PDNPs. As shown in Figures 4.7 and 4.8, a clear increase in cell killing efficacy was observed with BR-PDNPs + X-ray relative to all other treatment groups. PEG-BR micelles + X-ray did not produce any increased efficacy compared to X-ray alone, and CWO NPs + X-ray did show enhanced efficacy, as previously observed[90], but this improvement was not as large as that for BR-PDNPs. The sensitizer enhancement ratio (SER) values at 10% cell survival for CWO NPs and BR-PDNPs were 1.15 and 1.40, respectively. In addition, the α/β value increased for CWO NPs and BR-PDNPs, but this value was also higher for BR-PDNPs (please

note that the exact value of α/β in each experiment will fluctuate naturally, but in general the relative changes in values between treatment groups in each experiment should hold consistent from study to study). These results indicate that CWO NPs alone do not photosensitize cells as significantly as BR-PDNPs, and BR-PEG-encapsulation is essential for CWO NPs to mediate photodynamic therapy. These results support the proposed mechanism of action of BR-PDNPs and provided motivation for further study *in vivo*.

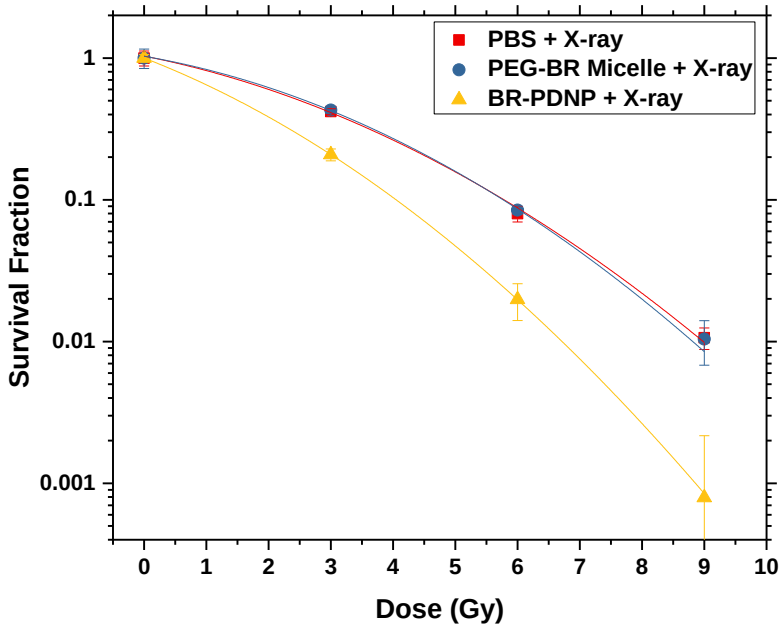

	SER	α	β	α/β
PBS + X-ray	1	-0.200	-0.035	5.7
PEG-BR Micelles + X-ray	1.00	-0.175	-0.040	4.4
BR-PDNP + X-ray	1.39	-0.391	-0.044	8.9

Figure 4.7. *BR-PDNP Initial Clonogenic Cell Survival Assay.* HN31 cells were seeded in 6 well plates at 0.2 x 10^3 (0 Gy), 0.8 x 10^3 (3 Gy), 1.6 x 10^3 (6 Gy), and 5.0 x 10^3 (9 Gy) in triplicate for each treatment group. Cells were incubated with PBS, PEG-BR micelles (0.2 mg/mL PEG-BR), and BR-PDNPs (0.2 mg/mL CWO nanoparticle) for 4 hours prior to X-ray irradiation. Irradiations were performed at 2 Gy/min using a 320 kV X-ray irradiator. Colonies of greater than 50 cells were counted to calculate survival fraction (N = 3). Error bars represent standard deviations. Table displays the parameters for the linear quadratic model fits ($S = \exp(\alpha*D + \beta*D^2)$), where S is survival fraction, D is radiation dose, and α and β are fitted parameters) and sensitizer enhancement ratios (SERs) at 10% survival fraction. Note: Experiment conducted using unfiltered particles.

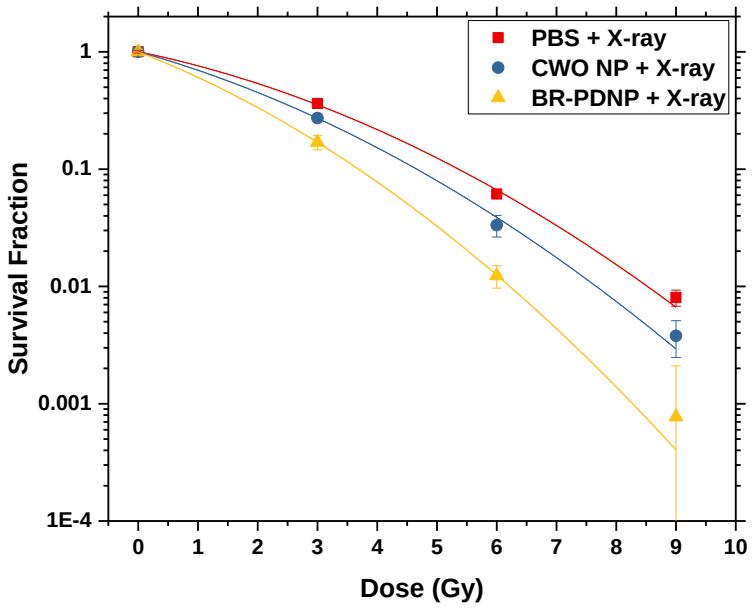

	SER	α	β	α/β
PBS + X-ray	1	-0.243	-0.035	6.9
CWO NP + X-ray	1.15	-0.330	-0.035	9.4
BR-RLNP + X-ray	1.40	-0.455	-0.046	9.9

Figure 4.8. *CWO NP Comparison Clonogenic Cell Survival Assay.* HN31 cells were seeded in 6 well plates at 0.2 x 10^3 (0 Gy), 0.8 x 10^3 (3 Gy), 1.6 x 10^3 (6 Gy), and 5.0 x 10^3 (9 Gy) in triplicate for each treatment group. Cells were incubated with PBS, CWO NPs (0.2 mg/mL CWO nanoparticle), and BR-PDNPs (0.2 mg/mL CWO nanoparticle) for 4 hours prior to X-ray irradiation. Irradiations were performed at 2 Gy/min using a 320 kV X-ray irradiator. Colonies of greater than 50 cells were counted to calculate survival fraction (N = 3). Error bars represent standard deviations. Table displays the parameters for the linear quadratic model fits ($S = \exp(\alpha*D + \beta*D^2)$), where S is survival fraction, D is radiation dose, and α and β are fitted parameters) and sensitizer enhancement ratios (SERs) at 10% survival fraction. Note: Experiment conducted using unfiltered particles.

Cell culture experiments screening for safety and efficacy of BR-PDNPs provided ample motivation for further study in animal models of head and neck cancer, as mentioned previously. To explore if BR-PDNPs exhibited similar efficacy enhancement *in vivo*, an HN31 xenograft study in Nod rag gamma (NRG) mice was conducted. For this experiment, 8 mice per treatment group had subcutaneous xenografts of HN31 cells generated, with 6 total treatment groups examined: PBS, CWO NPs, and BR-PDNPs ± X-ray. Mice received intratumoral injections of 10 mg/mL

(based on CWO NP concentration) or PBS split into two equal doses on days 6 and 7 of the study. Total X-ray dose used was 4 Gy split over two consecutive fractions (2 + 2 Gy on days 7 and 8). Mouse tumor volumes for each treatment group over time are displayed in Figure 4.9, plotted up to the first euthanasia event for each treatment group. On day 20, the PBS + X-ray and BR-PDNP + X-ray groups were sufficiently separated to reach statistical significance ($p < 0.1$).

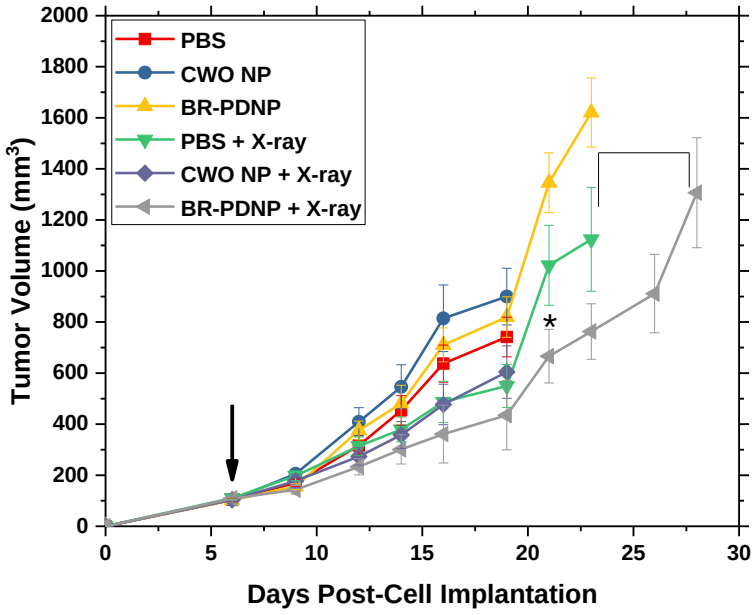

Figure 4.9. *Murine HNSCC Xenograft with NP Treatment.* Subcutaneous xenografts were produced by inoculation of 1.5 x 10^6 HN31 cells in 0.1 mL total volume in Nod rag gamma (NRG) mice (day 0). Intratumoral nanoparticle injection of 100 µL of 10 mg/mL CWO NPs in sterile PBS was conducted in two portions over two days (days 6 and 7, see arrow on graph for first injection) once tumors reached ~ 100 mm^3; blank PBS was injected in the control (PBS ± X-ray only) group. "Sub-therapeutic" (i.e., low-dose) radiation treatments with 320 keV X-rays were conducted on the second day of injection (day 7) and the subsequent day (day 8, 2 Gy each) for a total dose of 4 Gy. Tumors were measured with digital calipers. Tumor volumes for each group are displayed up to the first euthanasia event that occurred in each group. Error bars represent standard error. Asterisk denotes $p < 0.1$ using two-tailed student's t-test between PBS X-ray and BR-PDNP + X-ray groups on day 21 (the only point of significant difference, brackets highlight groups being compared). Euthanasia criteria were > 20% body weight loss or tumor volume > 2000 mm^3. N = 8 per treatment group. Note: Unfiltered particles were used for this experiment.

Figure 4.10 displays the mouse survival over time for each treatment group. As seen in Figure 4.10, the median survival times for BR-PDNP + X-ray, CWO NP + X-ray, and PBS + X-ray groups were 35, 33, and 33 days post-cell implantation, respectively. One-way ANOVA testing

was conducted to determine if a significant difference in group survival existed. Each irradiated treatment group (the + X-ray groups) was independently tested against its respective un-irradiated controls, and each was found to be significantly different within their pair except for CWO NP ± X-ray. However, when the irradiated groups were compared with each other, none of the groups were significantly different from each other, though BR-PDNPs + X-ray was somewhat close to reaching a p-value of less than 0.1 (p = 0.186). The results of ANOVA testing are displayed in the table below Figure 4.10.

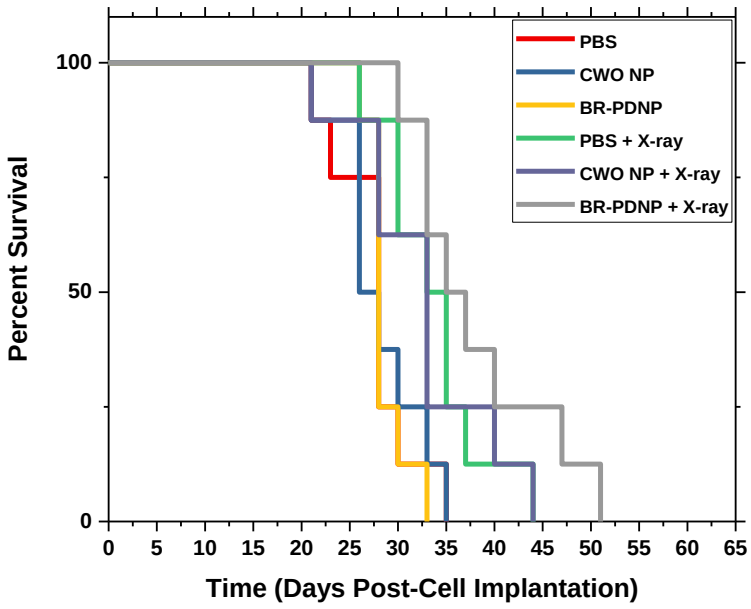

	PBS	CWO NP	BR-PDNP	PBS + X-ray	CWO NP + X-ray	BR-PDNP + X-ray
PBS	-	0.82145	0.55834	0.02496	0.12085	0.00324
CWO NP	-	-	0.77754	0.04015	0.16559	0.00492
BR-PDNP	-	-	-	0.02600	0.16506	0.00309
PBS + X-ray	-	-	-	-	0.70098	0.18556
CWO NP + X-ray	-	-	-	-	-	0.13590

Figure 4.10. *Murine HNSCC Xenograft with NP Treatment.* Kaplan-Meier survival curves were generated for the mice from the study detailed in Figure 7. Euthanasia criteria were > 20% body weight loss or tumor volume > 2000 mm^3. N = 8 per treatment group. Table displays p-values for pairs of treatment groups calculated using one-way ANOVA. Note: Unfiltered particles were used for this experiment.

We hypothesize that the lack of significant difference between irradiated group survival times (and of most of the irradiated tumor volumes, for that matter) is due to the limited number of radiation fractions administered to treat the mice (2 fractions of 2 Gy = 4 Gy total). At low doses of radiation (i.e., 2 Gy), the difference in survival fraction between PBS, CWO NP, and BR-PDNP-treated cells is small (see Figure 4.8). Thus, over the course of a typical radiotherapy prescription of 25 – 30 fractions of 2 Gy, a clear difference in tumor cell death would presumably emerge. In this mouse study, however, with only 2 fractions of radiation, the difference in cell death in vivo may not have been large enough to manifest in significant survival benefits. In addition, nanoparticle dose distribution was likely not perfectly homogenous throughout the tumor, leading to enhanced cell killing in some but not all of the tumor volume. Nonetheless, the tumor growth suppression and increased median survival time for BR-PDNP-treated mice relative to other treatment groups are encouraging results. These data suggest that the radio-sensitization effects afforded by the combination of PDT with primary RT observed *in vitro* are also present *in vivo*. Further study is warranted to confirm BR-PDNP-mediated RT-PDT efficacy in animal models.

4.5 Conclusions

Taken together, this study provides ample data that suggest BR-PDNPs are a novel formulation that can mediate combined radio/photodynamic therapy in solid tumors. The results demonstrate the new use of PEG-BR micelles as an encapsulant for $CaWO_4$ nanoparticles. BR-PDNPs emit UV-A and visible light under X-ray that causes dissociation of their bilirubin-PEG encapsulant, allowing for the continued excitation of the now-free bilirubin by the UV-A/visible light. This key step initiates the photodynamic therapy response by producing reactive oxygen species like singlet oxygen which complement the lethal effects of X-rays to enhance cancer cell death. In vitro efficacy testing demonstrated clear therapeutic enhancements in combining BR-

PDNPs with X-ray radiotherapy. Furthermore, a head and neck cancer xenograft experiment in mice suggested that these combined radio/photodynamic therapy enhancements are present *in vivo,* but further study is needed to confirm these results. BR-PDNPs represent a novel tool for combining radiation and photodynamic therapies for solid tumors, and further optimization and efficacy validation are warranted to examine their ultimate translational viability.

Acknowledgements

The HN31 cell line was generously provided by Dr. Jeffrey N. Myers at the MD Anderson Cancer Center.

Financial Conflict of Interest

A company, Lodos Theranostics LLC, is currently attempting to commercialize the technology in this manuscript. The corresponding author, You-Yeon Won, has an ownership interest in this company.

5. VISUALIZING INTRATUMORAL NANOPARTICLE DISTRUBTION USING COMPUTED TOMOGRAPHY (CT) UNDER MECHANICAL AGITATION: A PILOT STUDY

Vincenzo J. Pizzuti[†], Sandra E. Torregrosa-Allen[‡,ǁ], Melanie P. Currie[‡,ǁ], Bennett D. Elzey[‡,ǁ], and You-Yeon Won*[,†,‡]

[†]Davidson School of Chemical Engineering, [‡]Purdue University Center for Cancer Research, [ǁ]Department of Comparative Pathobiology, Purdue University, West Lafayette, Indiana 47907, United States

5.1 Abstract

Nanoparticle radiosensitizers are increasingly being investigated for their potential role as an adjuvant to primary radiotherapy of solid tumors. Promising efficacy results in a variety of animal models of cancer have been observed with these formulations, some of which are administered via intratumoral injection. This injection strategy improves localization of the administered dose within the tumor compartment, but little study has been conducted to examine methods to improve nanoparticle distributions within solid tumors after direct injection. In attempt to gain some insight, we conducted a pilot study on a mouse bearing a head and neck cancer xenograft to explore the effects of mechanical agitation on nanoparticle dose homogeneity using computed tomography (CT) scanning. Preliminary results indicate small improvements in dose distribution near the injection site after agitation, but global nanoparticle distribution is not markedly improved on the timescale observed. Further study is needed to clarify the mechanisms underlying nanoparticle transport and to optimize intratumoral administration protocols for better dose homogeneity that could potentially improve the ultimate therapeutic efficacy.

5.2 Introduction

Recently, nanoparticle-based radiosensitizers have been studied increasingly for incorporation into standard of care radiation therapy as an adjuvant treatment for cancer patients [91,92]. Several unique and promising formulations have shown positive results in cell culture and animal cancer models [36,49]. One such formulation has reached Phase II/III clinical trials, the hafnium oxide formulation (NBTXR3) by the French nanomedicine company Nanobiotix [6].

An important route of administration for these formulations is intratumoral injection. This technique can help to ensure localization of formulations within the tumor compartment and represents a viable delivery strategy for some solid tumors. However, little study has been dedicated to studying nanoparticle dose homogeneity after intratumoral injection. Several prior studies have examined tumoral transport and dose distribution of nanoparticles that have been systemically administered intravenously [93-95]. This prior work has found nanoparticle physicochemical properties and administration strategies that improve dose accumulation in the tumor compartment from systemic circulation, but such attention has been lacking for the intratumoral administration route (likely due to its less widespread use).

In an attempt to examine strategies for improving dose distribution of nanoparticle radiosensitizers in solid tumors, we conducted a pilot study exploring the potential role of mechanical agitation of the tumor after injection to improve nanoparticle homogeneity. Utilizing radio-luminescent calcium tungstate nanoparticles (RLNPs) previously developed in our laboratory [65], the role of sonic frequency mechanical agitation of the tumor after nanoparticle injection was explored. Nanoparticles were detected using X-ray computed tomography (CT) scanning and were scanned at various time points before and after mechanical agitation of the tumor.

At the end of this pilot study, it was found that mechanical agitation of the tumor near the site of nanoparticle injection leads to locally slightly improved dose distribution within the peripheral fluid compartment surrounding the solid tumor lobes. This improvement seems to be driven by the movement of nanoparticles suspended in the excess liquid introduced from the injection in response to the agitation. Only marginal improvements in homogeneity near the injection site were observed, and minimal improvements in bulk tumor tissue penetration were found over the brief timescales observed in this study. More investigation is warranted under a variety of non-agitated and agitated conditions at various agitation "doses," as well as comparison with ultrasonic tumor agitation to better understand the behavior observed and to devise optimized strategies for intratumoral administration of nanoparticle radiosensitizers.

5.3 Materials and Methods

Calcium Tungstate Nanoparticle Formulation and Characterization

Nanocrystalline calcium tungstate were synthesize via a microemulsion autoclave reaction as previously described [88]. The block copolymers used for encapsulation were synthesized via a ring-opening polymerization of racemic lactide with poly(ethylene glycol) (PEG) precursors, as previously described24. For poly(ethylene glycol-block-lactic acid) (PEG-PLA), 0.45 g of monomethoxy PEG (CH3-PEG-OH, Sigma, Mn = 5,000 Da) and 0.45 g of racemic lactide were added to a round bottom flask, the flask was heated to 70 °C, evacuated under vacuum for 30 minutes, purged with Argon gas, and then 22 mL of anhydrous dichloromethane (DCM, Sigma) were added to dissolve the reactants. The reaction was catalyzed by 1,8-diazobicyclo[5.4.0]unde-7-ene (DBU, 98%, Sigma), with 0.22 mmol dissolved in 2 mL of DCM added directly to the reaction vessel. The reaction was run for 2 h at room temperature and was terminated by adding 15 mg of benzoic acid (>99.5%, Sigma). The PEG-PLA was precipitated by dropwise addition of

the reaction solution to 1 L of mixed hexanes (Thermo Fisher). The precipitate was then dried overnight in a vacuum oven.

Encapsulated RLNPs were prepared as follows. 300 mg of PEG-PLA was dissolved in 3.9 g of N,N-dimethylformamide (DMF, Sigma), and 50 μL of a 10 mg/mL suspension of CWO NPs in DMF was added to the vial. The vial was then sonicated and mechanically stirred with an overhead stirrer at 10,000 rpm, and 2.1 mL of phosphate buffered saline (PBS) was added to the vial and allowed to emulsify for 10 minutes. The resultant emulsion was then centrifuged at 5,000 rpm for 10 min to pellet the encapsulated nanoparticles. The supernatant was discarded, and the pellet was resuspended in PBS to the desired concentration. Filtered solutions were passed through a 220 nm PVDF filter. Details on the size difference and distributions of the filtered vs. unfiltered particles can be found in the Supporting Information (SI) (characterized by dynamic light scattering (DLS)). DLS experiments were conducted at 0.025 mg/mL NP concentration.

Mouse HN31 Xenograft Experiment

HN31 cells were implanted subcutaneously into the right flank of a male Rag 1 knockout mouse at a cell density of 1.2×10^6 cells in a 50%/50% mixture of Matrigel and PBS (v/v). Tumor volume was measured three times per week using digital calipers. Tumor volume was allowed to reach 300 mm^3, at which point a 100 μL injection of 10 mg/mL RLNPs (PEG-PLA encapsulated calcium tungstate nanoparticles) was administered intratumorally. Immediately following injection, the mouse was placed under isoflurane anesthesia and aligned inside of a micro-computed tomography (CT) scanner (Perkin Elmer Quantum GX microCT, Waltham, MA). A CT scan was then taken with a voxel size of approximately 90 μm on edge. After scan completion, the mouse was kept under anesthetic and a custom-built mechanical agitator head was used to repeatedly agitate the surface of the tumor near the site of injection for a period of 1 minute. The mechanical agitator

was constructed from a retrofitted electric toothbrush motor, in which a stainless-steel plate was attached to the toothbrush rotor head using an epoxy glue (a schematic and image of the device can be found in the Results and Discussion section). The mouse was then immediately re-aligned in the CT scanner and re-scanned. This process was then repeated once more. After this initial set of injection/scans (Day 1), a follow up scan was taken on Day 3 without any additional administration of mechanical agitation. The mouse was then sacrificed due to humane criteria.

5.4 **Results and Discussion**

As described in the Materials and Methods section, a mouse bearing a human head and neck cancer tumor xenograft was injected with PEG-PLA encapsulated radio-luminescent calcium tungstate nanoparticles (RLNPs). The mouse was subsequently scanned using X-ray computed tomography (CT) to track the distribution of the RLNPs (which act as CT contrast agents) at various time points before and after mechanical agitation using a custom-built mechanical agitation device. This device was created by retrofitting an electric toothbrush rotor head with a small stainless-steel plate attached via an epoxy glue. In Figure 5.1, a schematic view and actual image of the device are displayed for convenience.

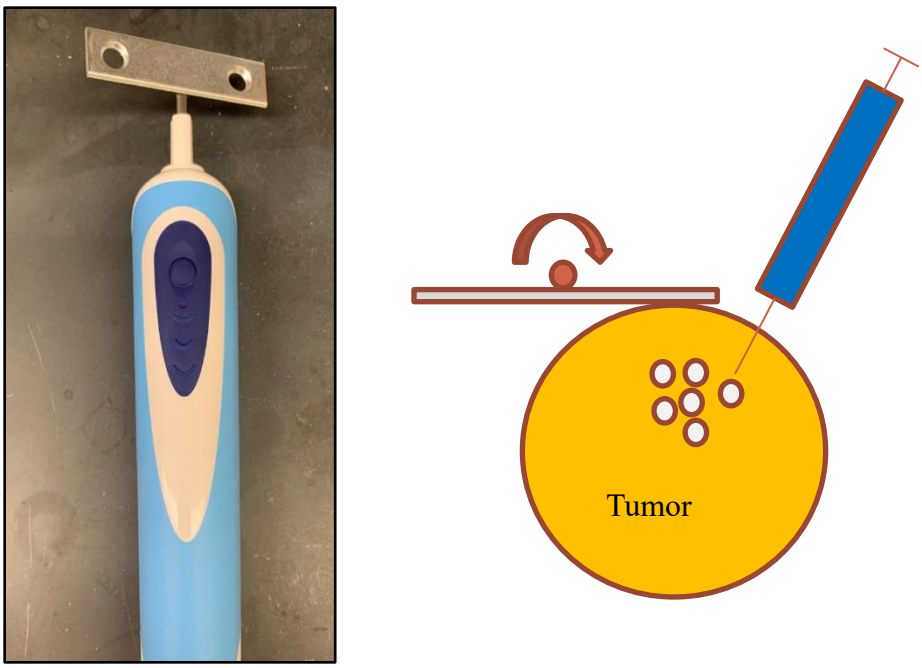

Figure 5.1. *Mechanical Agitation Device and Schematic of Implementation*. The image on the left of the figure features the modified electric toothbrush rotor with stainless steel plate attached. In the schematic on the right, a simple diagram lays out the experimental implementation of mechanical agitation, in which nanoparticles (RLNPs, small gray circles) are administered via intratumoral injection and later agitated by the device such that the metal plate just makes contact with the surface of the tumor.

CT scans of the mouse tumor were conducted at three distinct time points: immediate post-RLNP injection, post-agitation (two "doses" of one-minute agitation), and two days post-agitation. Some representative 2D images at the same axial location are displayed in Figure 5.2. As seen in this figure, there is a difference in RLNP distribution at the same axial (spinal) depth for each of the time points. Between pre- and post-agitated samples (Figures 5.2 (A) and (B)), a noticeable difference in contrast pattern is observed, but this change is minor when compared with the two-day post-agitation (Figure 5.2 (C)). The main reason for this large discrepancy is the appreciable change in tumor volume that occurred in the two day period, which significantly shifted the distribution of RLNPs surrounding the tumor.

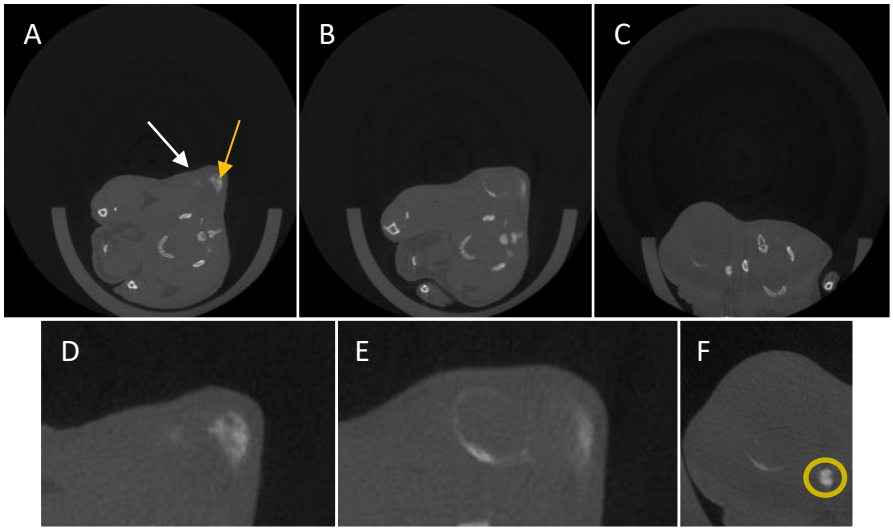

Figure 5.2. *CT Images of RLNP-injected Xenografts*. Axial slices of acquired CT scans are displayed at approximately the same axial (spinal) location. White arrow is pointing at the bulk tumor mass and orange arrow is highlighting an area of high nanoparticle (RLNP) concentration. (A) Immediate post-injection scan. (B) Immediate post-agitation scan. (C) Two-days post-agitation scan. High-zoom version of the (A) - (C) are displayed in (D) - (F), respectively. Orange circle in (F) is surrounding contrast from a bone structure, not RLNPs. Tumor xenograft was at approximately 300 mm^3 at time of injection, and mechanical agitation was completed using the described apparatus for two "doses" of one minute in duration.

Next, 3D reconstructions and heat-maps of RLNP concentrations within the tumor at each time point were examined in order to determine if the noticeable changes resulting from agitation seen in the 2D images in Figure 5.2 were also different in three dimensions. This reconstruction was accomplished using ImageJ's 3D reconstruction tool for image stacks. The resultant 3D figures and heatmaps are displayed in Figure 5.3.

As seen in the figure, the changes in RLNP distribution occurred after agitation in the 3D images and occurred to a greater extent in the two-day post-agitation case. From these reconstructions, it seems that the bulk of the RLNPs remain in the interstitial fluid compartment surrounding each lobe of the tumor and do not penetrate the dense tumor tissue to an easily visualized level of contrast (which is proportional to concentration). What this implies is that, during agitation, the changes in distribution may be attributable to the excess fluid in the tumor compartment from the injection volume itself. RLNPs injected in this fluid medium that are still

suspended at the time of mechanical agitation will be redistributed in this fluid compartment. In the two-days post-agitation case, the particles may diffuse readily within this fluid compartment to surround the lobes of the tumor more evenly but may have difficulty entering the dense tissue at the core of the lobes because of strong intracellular connections creating a more tortuous path and a positive pressure gradient that must be overcome.

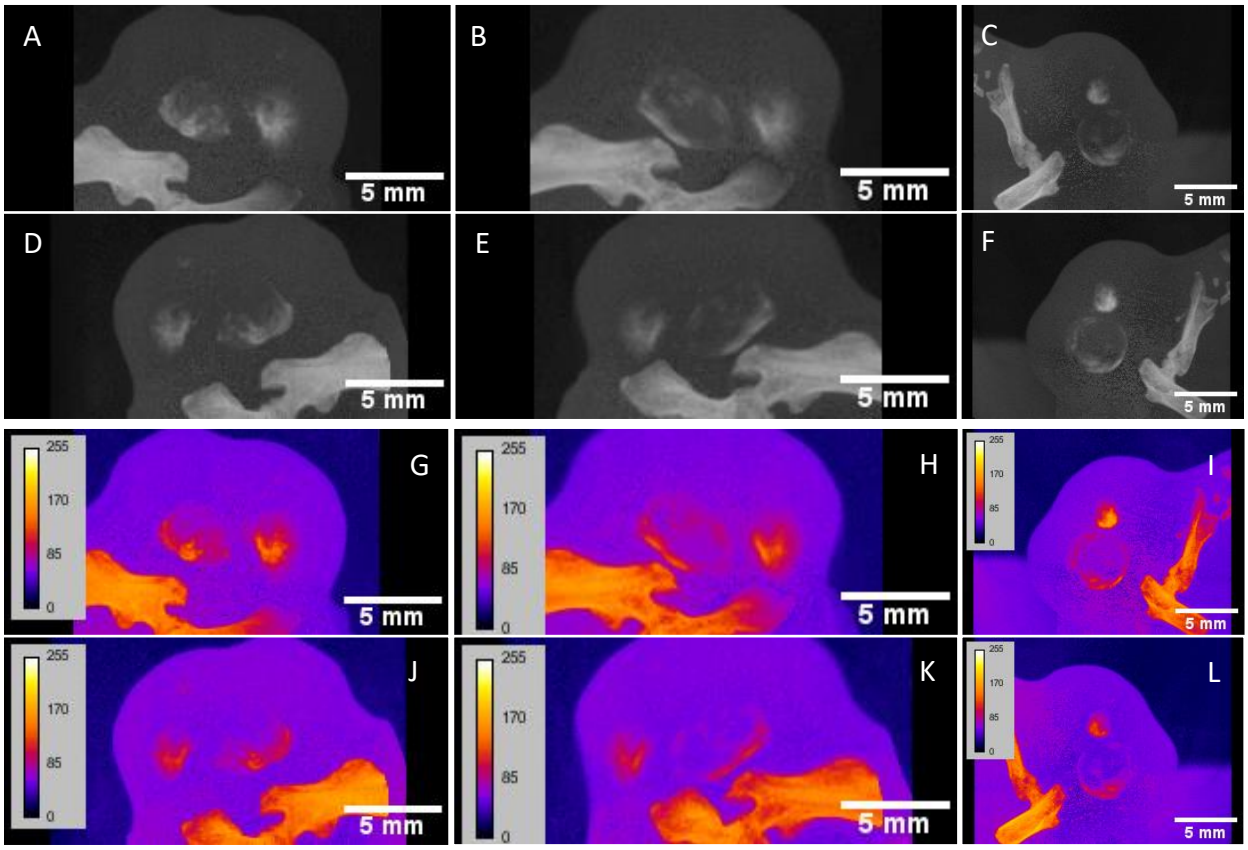

Figure 5.3. *3D Reconstructed CT Images of RLNP-injected Xenografts*. 2D CT image stacks were reconstructed using ImageJ to create representative images above. (A) Zero-degree view of 3D reconstruction for immediate post-injection. (B) Zero-degree view of 3D reconstruction for immediate post-agitation. (C) Zero-degree view of 3D reconstruction for two-day post-agitation. (D) - (F) display the views from 180-degree vantage point of the reconstructions displayed in (A) – (C). Images (G) – (L) display heat maps generated from 3D reconstructions in (A) – (F), respectively. Embedded within each image is a calibration bar for heat map intensities displayed within.

From these data, it was confirmed that mechanical agitation of the tumor near the injection site improved RLNP-distribution, but mainly in the fluid compartment surrounding the lobes of the tumor. For subsequent analysis, only pre- and post-agitation scans (and not two-day post-

agitation scans) were included because of the large change in tumor volume between those time points. Subsequent study should include an un-agitated control for comparison at these later time points. To analyze the visual information a little further, zoomed 3D reconstructions of the tumor volume were created for pre- and post-agitation scans, and a 2D cross section near the injection site was extracted and analyzed to produce a histograms of each image's gray value intensities. This mean was a y-value average that was plotted as a function of x-axis distance for the images seen in Figures 5.4 (C) and (D). The resultant histograms are displayed in Figure 5.4 (E), and the mean values and standard deviations are included in the table in Figure 5.4 (F). From these data, a clear drop in standard deviation of gray value intensities occurs in the post-agitation case, suggesting that the maxima and minima in concentration are somewhat reduced to provide a more evenly distributed concentration in the fluid compartment near the site of injection. Final, tumor-wide radial distribution functions were calculated for gray intensity values in each voxel of the tumor volume for pre- and post-agitation samples. These results are plotted in Figure 5.4 (G). As seen in the plots, small differences do exist between the pre- and post-agitation samples, but the differences are not large enough to claim any significant changes on a global (tumor-wide) scale in RLNP distribution in 3D. What this suggests is that the changes in distribution near the injection site are localized effects that occur within the interstitial fluid compartment surrounding the tumor during agitation, but minimal changes occur on a tumor-wide scale due to lack of RLNP-penetration into the bulk dense tumor tissue lobe cores.

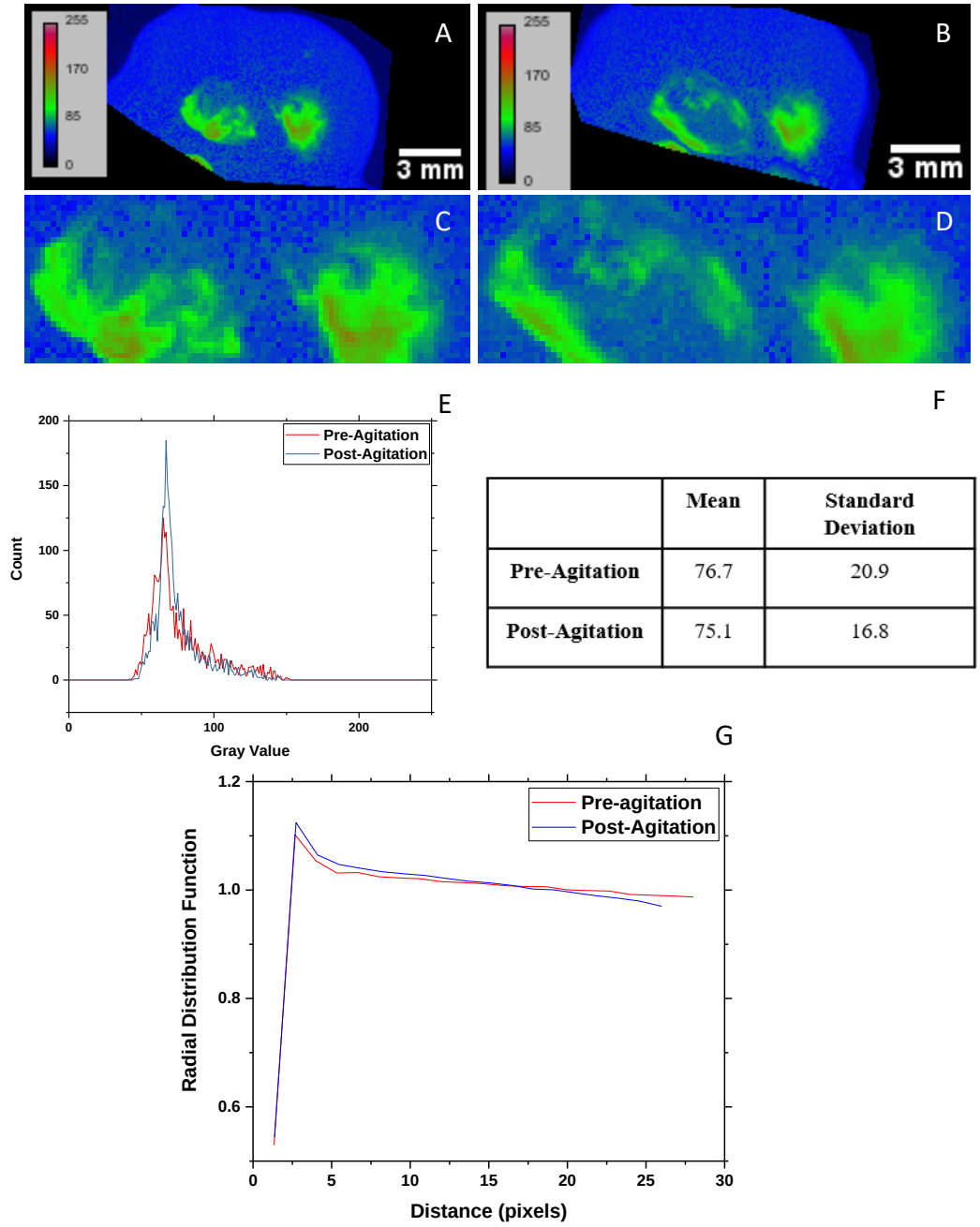

	Mean	Standard Deviation
Pre-Agitation	76.7	20.9
Post-Agitation	75.1	16.8

Figure 5.4. *Analyzing 3D Reconstructed CT Images of RLNP-injected Xenografts*. (A) High-zoom heat map of zero-degree 3D reconstruction (viewed from left to right) for immediate post-injection timepoint (pre-agitation). (B) High-zoom heat map of zero-degree 3D reconstruction (viewed from left to right) for immediate post-agitation. (C) and (D) are 2D cross-sections zoomed around the major nanoparticle clusters displayed in (A) and (B). (E) is a histogram of mean gray values as a function of distance along the x-axis of the images in (C) and (D), averaged over all y-axis values for each x-axis point. The mean and standard deviation of each of these is presented in the table in (F). In plot (G), the tumor-wide radial distribution function was calculated for pre- and post-agitated CT image stacks. The two-day post-agitation scan was not included because the tumor volume changed appreciably during that time and could not be directly compared to the other samples.

Taken together, these data suggest that mechanical agitation of the tumor site after nanoparticle administration can provide small improvements in the nanoparticle dose distribution in the fluid compartment surrounding the tumor lobes. However, significant transport limitations exist in the form of positive pressure gradients and minimal inter-cellular space in the high-density tumor tissue that prevent nanoparticles from entering deeper into the tumor core on short time scales. Given the relative ease of agitation "dose" administration, it may be worthwhile to examine the effects of larger numbers of repeated agitation on ultimate nanoparticle distribution (both within the periphery of the tumor near the injection site and globally). Further experimentation under various other treatment conditions, including ultrasonic agitation and increased mechanical agitation "doses" should be conducted to provide a better understanding of the results within this study and to optimize the dose administration protocol for nanoparticle-based radiosensitizers in future efficacy studies.

5.5 Conclusions

Preliminary data from this CT scan pilot study suggest that mechanical agitation of the tumor site post-injections helps to improve dose distribution of encapsulated nanoparticles within the tumor periphery near the site of injection, but these effects are mainly local in nature. Overall tumor penetration is not improved on the short time scale between pre- and post-mechanical agitation CT scans; however, longer term behavior is not known at this time. The implications of this experiment are important because dose homogeneity of the nanoparticle radiosensitizers studied herein likely affects their ultimate biological efficacy. These data are very preliminary in nature, and thus similar, controlled experiments with a larger number of animals should be conducted in order to further understand the observed effects of mechanical agitation and optimize nanoparticle dose administration protocols. In addition, further testing should be conducted

comparing the biological efficacy of the nanoparticles under X-ray radiotherapy under different agitation conditions to determine definitively to what extent nanoparticle homogeneity affects cancer treatment outcomes.

6. CONCLUSIONS

The proposed thesis had three distinct research goals set out for experimentation. First, this work explored the effects of folic acid-surface functionalization on block copolymer encapsulated radio-luminescent calcium tungstate nanoparticles. As detailed in Chapter 3 of this document, these surface functionalized nanoparticles were found to significantly increase therapeutic efficacy when compared to X-ray radiotherapy alone or in combination with non-functionalized nanoparticles in cell culture and murine xenograft models of human head and neck cancer solid tumors. Initial translational feasibility and safety was also explored in a canine clinical case study (a soft tissue sarcoma patient) combining the folic acid-functionalized nanoparticles with palliative radiotherapy, and overall results were promising. In addition, folic acid-functionalization of the nanoparticles was found to enhance efficacy by increasing cellular sensitivity to ultraviolet radiation emissions from the nanoparticles.

The second goal of this work was to explore the combination of the radio-luminescent calcium tungstate nanoparticles with photo-responsive bilirubin-polymer conjugates as an encapsulant, described in Chapter 4. These bilirubin-encapsulated nanoparticles enhanced the efficacy of X-ray radiotherapy alone and in combination with bare calcium tungstate nanoparticles by facilitating a combination of radiation and photodynamic therapies. These results were observed in cell culture and murine xenograft models of human head and neck cancer.

The third, minor aim of this thesis was to preliminarily examine the effects of mechanical agitation on radio-luminescent nanoparticle distribution in solid tumors, tracked using X-ray computed tomography and described in Chapter 5. Sonic frequency mechanical agitation was found to provide small improvements in nanoparticle homogeneity in the fluid compartment surrounding the lobes of the tumor but had limited effect on tumor penetration in the dense lobes.

Overall, this work emphasizes two advances in the development of nanoparticle-based radiosensitizers, each operating through separate modes of action. Both strategies offer promising efficacy enhancements when combined with primary radiotherapy and represent potential candidates for adjuvant modalities to be used in treating primary or recurrent solid tumors.

APPENDIX A. SUPPLEMENTARY INFORMATION FOR CHAPTER 3

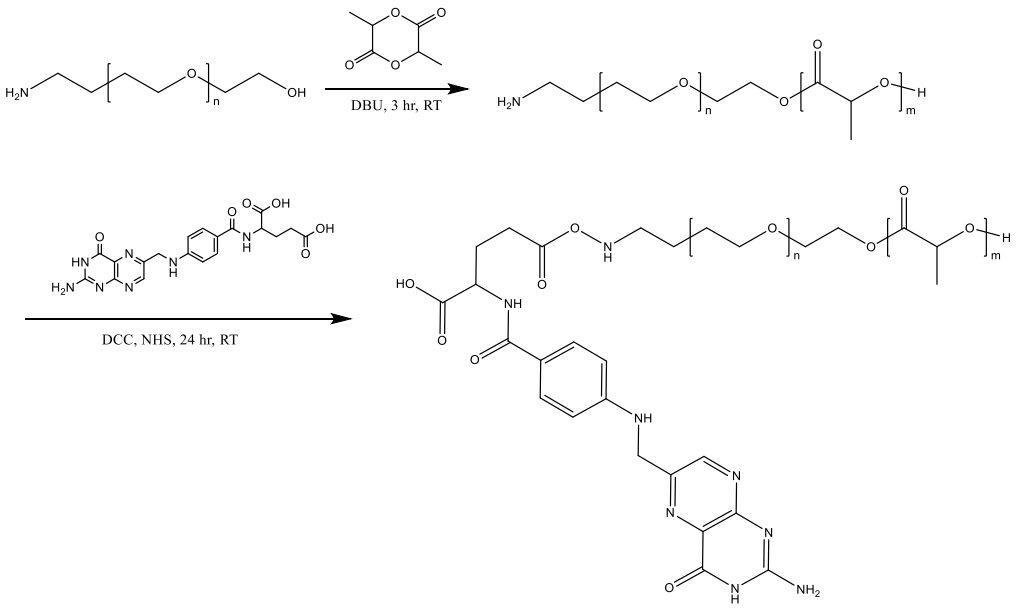

Scheme 3.S 1. Synthetic Pathway for Fol-PEG-PLA from NH_2-PEG-OH. This novel pathway eliminated one reaction and one purification step from the original protocol[65], allowing for easier synthesis and reduced cost and losses.

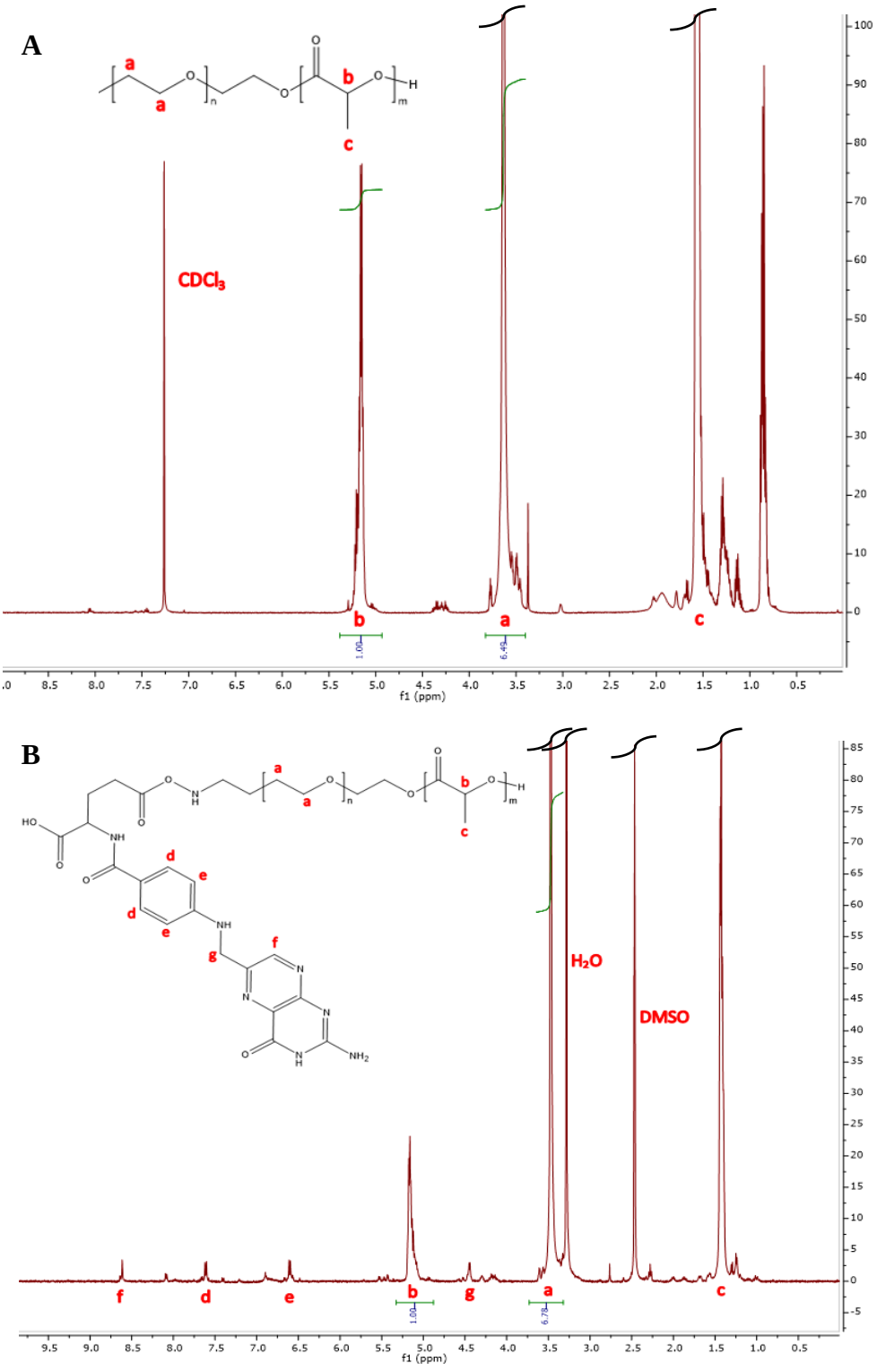

Figure 3.S 1. *^{1}H-NMR Spectrum of Synthesized Polymers.* (A) Structure of PEG-PLA was confirmed via proton NMR, and the M_n of the polymerized PLA chain was estimated from integration to be 5,040 Da. (B) Structure of Fol-PEG-PLA was confirmed via proton NMR, and the M_n of the polymerized PLA chain was estimated from integration to be 4,850 Da. GPC results (not displayed) found that the polydispersity of PEG-PLA was 1.14 and Fol-PEG-PLA was 1.21.

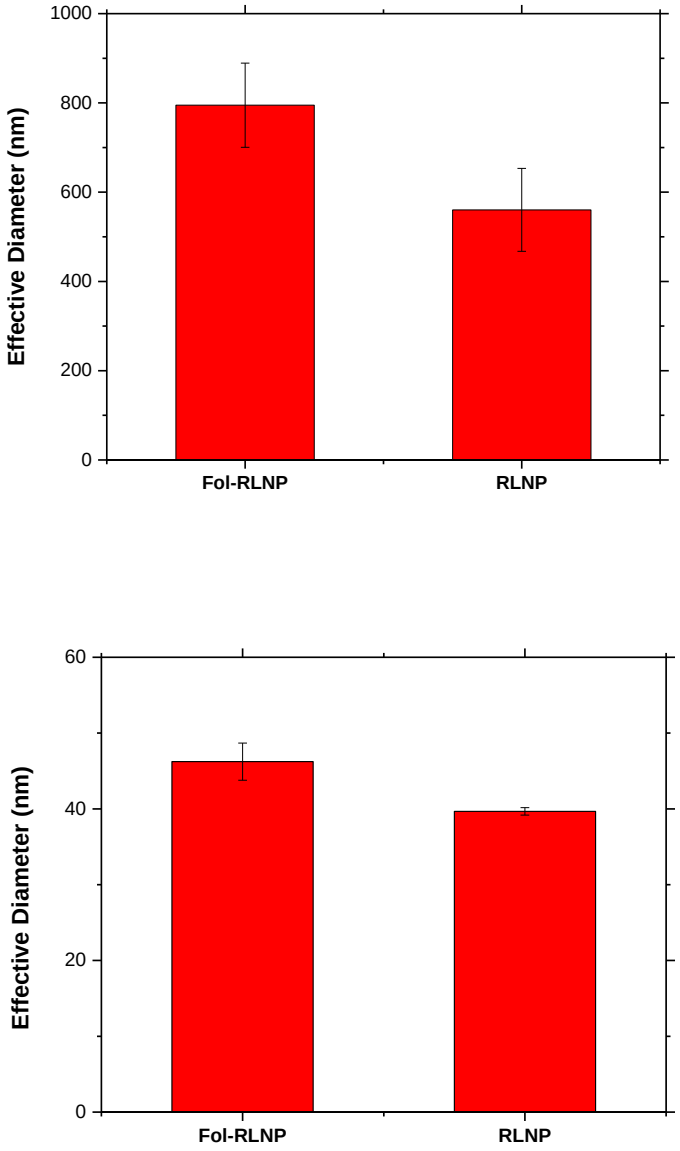

	Unfiltered	Filtered
RLNP	0.416 ± 0.014	0.078 ± 0.007
Fol-RLNP	0.410 ± 0.007	0.172 ± 0.030

Figure 3.S 2. *DLS Measurements of RLNPs and Fol-RLNPs.* (Top) Unfiltered nanoparticle DLS results. (Bottom) Filtered nanoparticle DLS results. Mean effective diameters for RLNPs and Fol-RLNPs, produced as described in the Materials & Methods. Error bars represent standard deviation. Unfiltered samples were left as prepared, and filtered samples were passed through a 200 nm PVDF syringe filter before analysis by DLS. For DLS runs, unfiltered particles were diluted ten-fold in PBS, and filtered particles were analyzed immediately after filtration without dilution. Table summarizes polydispersity values reported by DLS analysis (with standard deviations). N = 3.

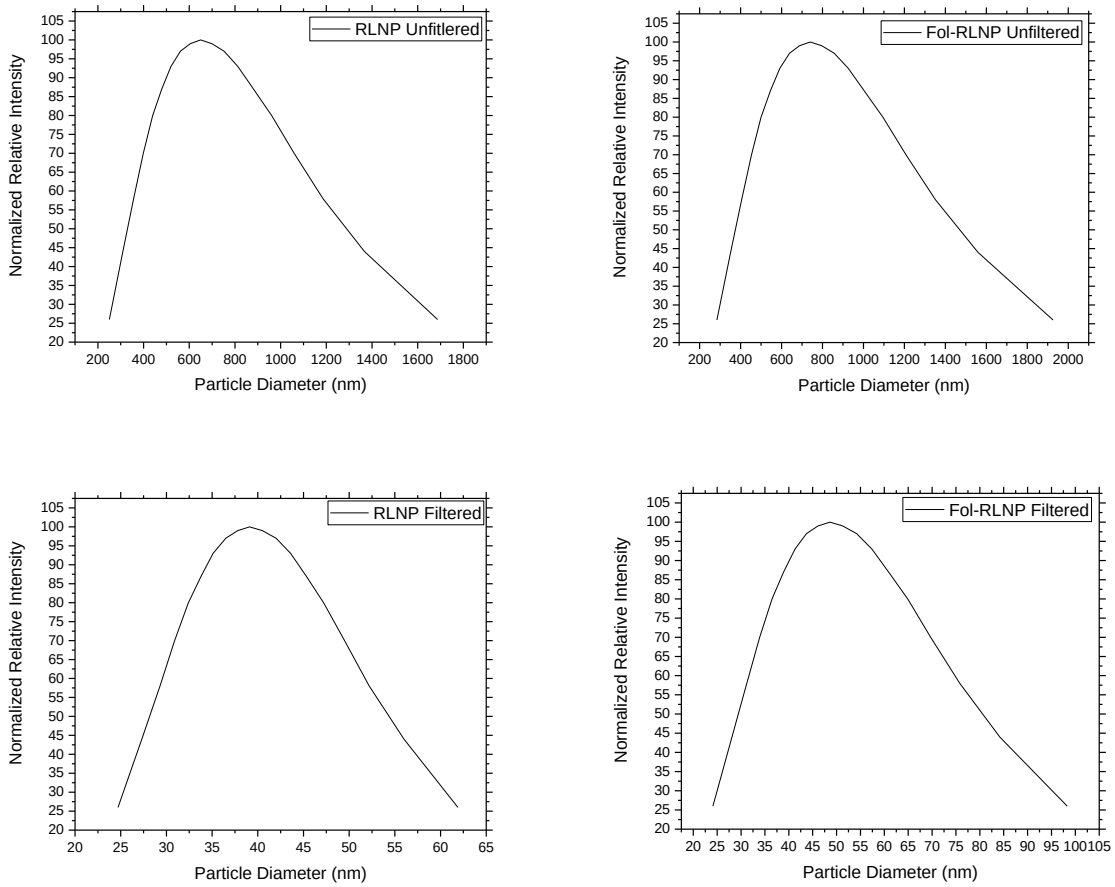

Figure 3.S 3. *Representative Lognormal DLS Size Distributions of RLNPs and Fol-RLNPs.* (Top Left) Unfiltered RLNP DLS lognormal particle size distribution. (Top Right) Unfiltered Fol-RLNP DLS lognormal particle size distribution. (Bottom Left) Filtered RLNP DLS lognormal particle size distribution. (Bottom Right) Filtered Fol-RLNP DLS lognormal particle size distribution. Filtered samples were passed through a 200 nm PVDF syringe filter before analysis by DLS. Unfiltered particles were diluted ten-fold in PBS, and filtered particles were analyzed immediately after filtration without dilution. Each plot is a representative example taken from one of the N = 3 samples displayed in Figure 3.S2.

Supplemental Material for Mechanism of Action Examintation

Hypothesis (1) from the main text was tested by exposing HN31 cells to Fol-RLNPs with varying folate densities, RLNPs, free folic acid, and negative and positive controls (PBS and 5-aminolevulinic acid, respectively) for 4 hours and subsequently measuring intracellular and extracellular PPIX levels. PPIX was chosen as a target molecule because, as mentioned in the main text, it is an endogenous photosensitizer with the ability to produce ROS upon excitation from a

UV/blue light source. Although folic acid is not known to induce photosensitization of cancer cells, the haem/iron metabolic pathways do interact with the folic acid pathway via two proteins: SLC46A1 and ferritin[96]. Folic acid competes with exogenous iron sources for transcellular transport via SLC46A1[97]. High levels of ferritin upregulate folate-specific enzymes[98,99], so the converse relationship with high folic acid levels could potentially increase ferritin levels, leading to reduced free iron and decreased conversion of PPIX to haem. Examination to determine if folic acid functionalization would induce changes in PPIX levels in the cells was warranted since PPIX is the immediate metabolic precursor to haem[100,101].

The resultant PPIX levels are displayed in Figure 3.S4. Only the positive control (5-ALA) showed significant enhancement in PPIX levels compared to the negative control. These data suggested that the increase in efficacy from Fol-RLNPs compared to RLNPs was not due to increases in PPIX levels initiated by Fol-RLNPs.

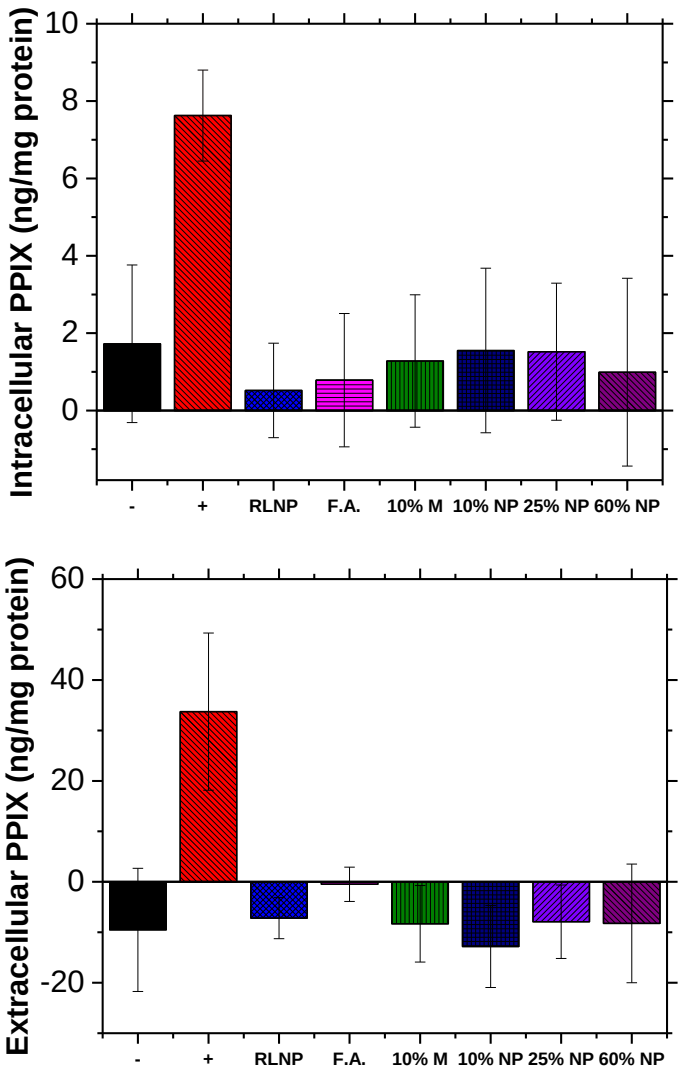

Figure 3.S 4. *Intracellular PPIX Levels in Response to NP Exposure.* Intracellular and extracellular PPIX levels in HN31 cells with exposure to PBS ("-" neg. control), 5-ALA ("+" pos. control,1 mM), RLNPs ("RLNP"), free folic acid ("F.A.", 0.2 mM), 10% Fol-PEG-PLA Micelles ("10% M", empty micelles without CWO NPs and 10% of PEG chains by weight functionalized with folic acid), 10% Fol-RLNP ("10% NP", standard Fol-RLNPs with 10% by weight of PEG chains functionalized with folic acid), 25% Fol-RLNP ("25% NP", 25% by weight of PEG chains functionalized with folic acid), and 60% Fol-RLNPs ("60% NP", 60% by weight of PEG chains functionalized with folic acid) (all CWO samples were at a concentration of 0.2 mg/mL) for 4 hours. Measurements were conducted using a fluorescence spectrophotometer (405 nm ex./630 nm em.) on cell extracts (intracellular) or used cell culture media (extracellular) from 2.0 x 10^5 cells per well. Signals were normalized to total cellular protein measured via the BCA assay. Raw measurement values of fluorescence for extracellular samples were corrected for background fluorescence from materials present in the culture medium, and these measurements are displayed in supplemental Figure S5. All error bars represent standard deviations. *Only the positive control was significantly different compared to negative control in each case, indicated by $p < 0.05$ compared with the negative control within each run using two-tailed Student's t-test (N = 6). Note: Experiment conducted with unfiltered particles.

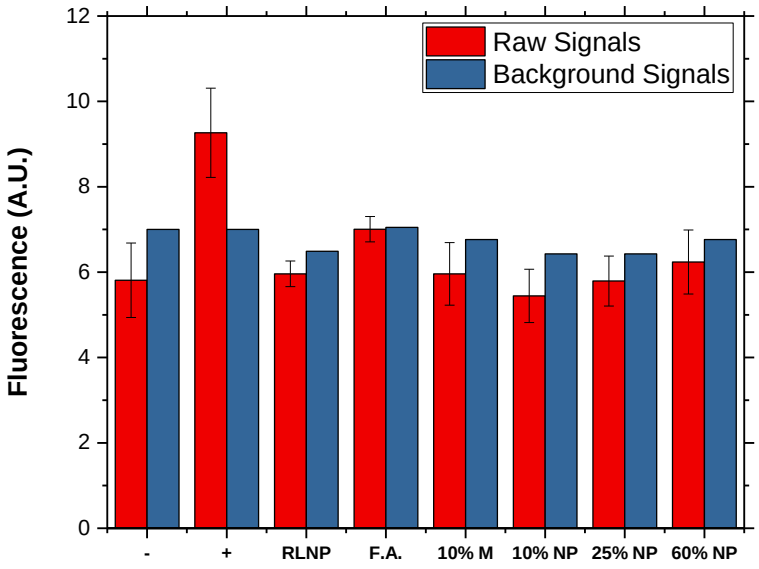

Figure 3.S 5. *Raw PPIX Measurements for Extracellular PPIX Data*. Displayed are the raw signals for the extracellular PPIX measurements alongside their background signals for fluorescence at 630 nm with 405 nm excitation. Error bars represent standard deviations. Note that the background signals are within error of the measurements for all except the positive control, which is why Fig. 3.S4 displays extracellular PPIX levels that are slightly below zero. N = 6.

Hypothesis (2) was tested using flow cytometry experiments that were conducted with HN31 cells exposed to Fol-RLNPs and RLNPs loaded with co-encapsulated PPIX as a fluorescent marker. After a 4-hour incubation with the NPs, cells were analyzed for fluorescence at 630 nm (using 405 nm excitation). Figure 3.S6 displays the histogram results of this experiment. The calculated uptake efficiencies were 84.6% and 81.3% for RLNPs and Fol-RLNPs, respectively. This indicates that RLNPs and Fol-RLNPs are taken up equally well and suggests that the increases in efficacy in the Fol-RLNP treatment group compared to the RLNP treated group is not due to increased cell uptake/internalization.

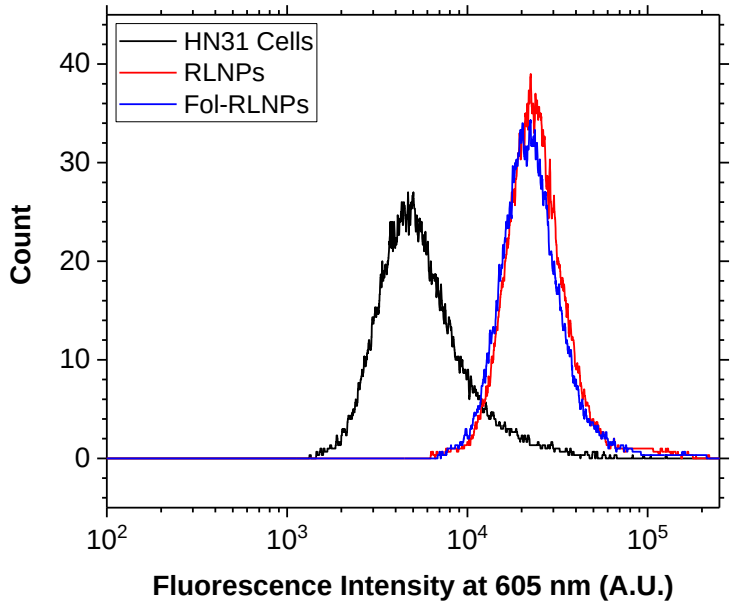

Figure 3.S 6. *Uptake of Nanoparticles by HN31 Cells.* HN31 Cells were exposed to RLNPs and Fol-RLNPs with co-encapsulated PPIX as a fluorophore for uptake measurement at a CWO concentration of 0.2 mg/mL. Cells were incubated with NPs for 4 hours, washed, and removed from the wells. Cells were then analyzed using flow cytometry using standard techniques with 405 nm excitation and 630 nm emission measurements. The resultant histogram of cell count versus fluorescence intensity is displayed above. Overall uptake efficiencies were 84.6% and 81.3% for RLNPs and Fol-RLNPs, respectively. Note: Experiment conducted with filtered particles.

To test hypothesis (3), a confocal imaging experiment was conducted in HN31 cells. Here, the cells were cultured directly on microscope cover slips until they reached around 70 – 80% confluence, at which point they were exposed to Fol-RLNPs and RLNPs loaded with co-encapsulated PPIX (as a fluorescent tracker of the NPs) for 4 hours. Afterward, the cells were washed 3 times with PBS and fixed using cold methanol. The cover slips were then mounted onto slides and imaged using DIC with a 488 nm laser and for fluorescence at 630 nm using 405 nm laser excitation. The images obtained are displayed in Figure 3.S7. Inspection of the images reveals no immediate discernable difference between Fol-RLNP and RLNP treated groups. FFT transformations were performed and analyzed for average intensities, and the groups were not significantly different (see Figure 3.S8). Additionally, an average pixel intensity measurement for the cell nuclei in each group was conducted and found that there was no difference in the pixel intensities found within the nuclei of each cell (see Figure 3.S9). From this analysis, it is reasonable

to state that there was no difference observed in the intracellular trafficking of Fol-RLNPs compared to RLNPs, and therefore is likely not the reason for the increase in efficacy observed for Fol-RLNPs.

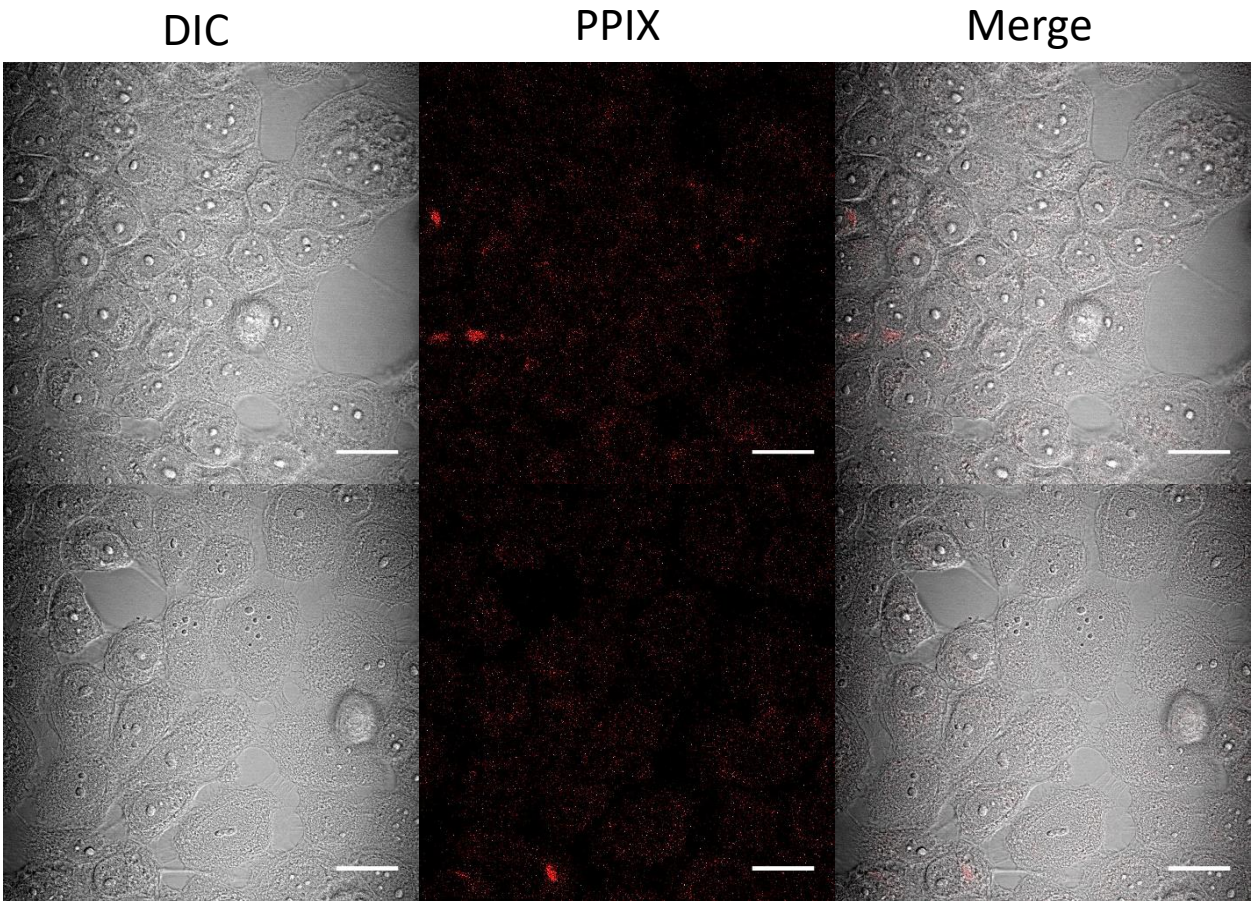

Figure 3.S 7. *Confocal Images of Labeled RLNPs and Fol-RLNPs in HN31 Cells.* (Top) HN31 cells exposed to PPIX-labeled Fol-RLNPs. (Bottom) HN31 cells exposed to PPIX-labelled RLNPs. Scale bars = 20 μm. Cells were cultured directly on microscope coverslips until reaching approximately 80% confluence. Cells were then incubated with labelled nanoparticle solutions at a CWO concentration of 0.2 mg/mL for 4 hours in the dark. Cells were washed three times with PBS and fixed with cold methanol and then mounted onto microscope slides and imaged using a Zeiss LSM 880 Upright Confocal at 63x using an oil immersion lens. DIC images were taken using a 488 nm laser, and PPIX images were taken using a 405 nm laser with a 600 – 650 nm emission filter. For PPIX images for both samples, contrast was enhanced by the same amount to improve visibility. Note: Filtered particles were used for this experiment.

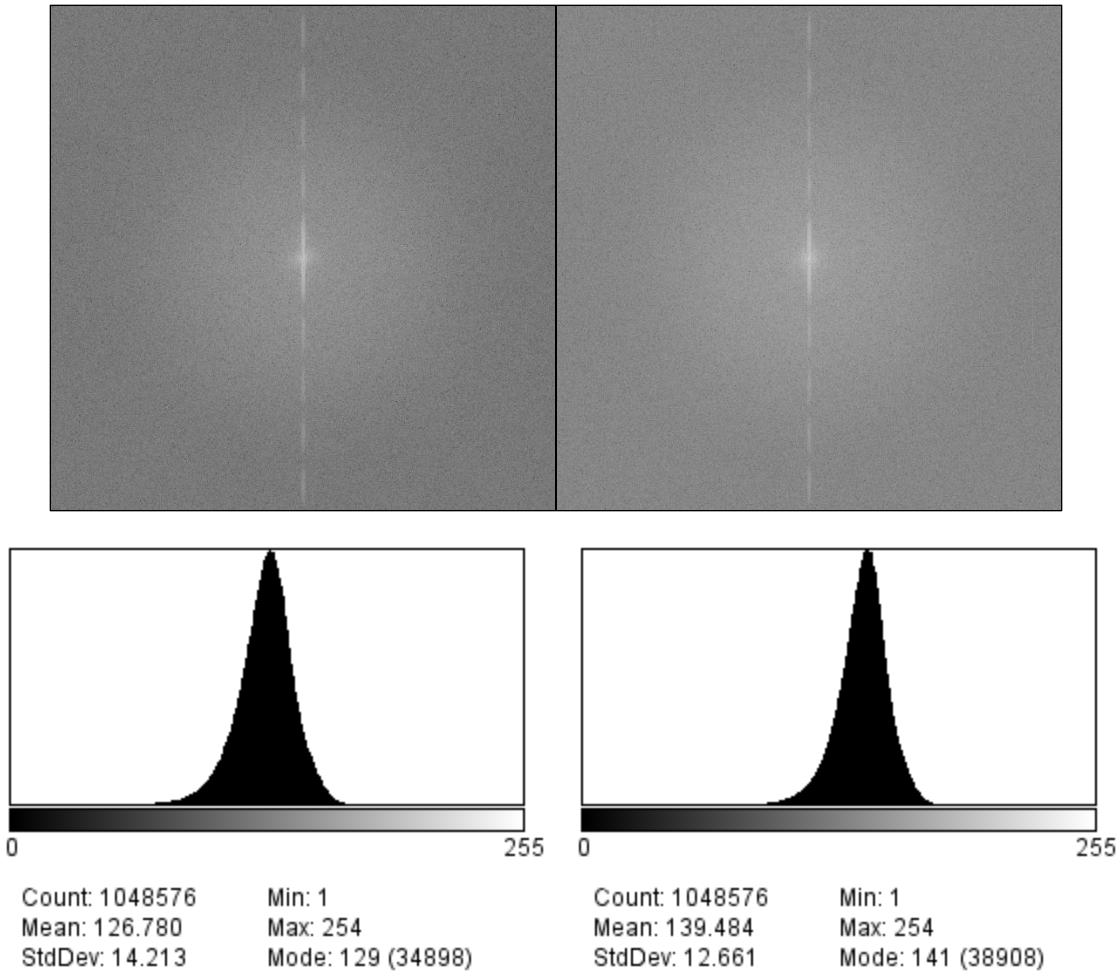

Figure 3.S 8. *FFT of Confocal PPIX Channel Images from Figure 3.S 7.* (Upper Left) FFT of RLNP confocal PPIX channel image. (Upper Right) FFT of Fol-RLNP confocal PPIX channel image. (Lower Left) Histogram results of FFT of RLNP sample. (Lower Right) Histogram results of FFT of Fol-RLNP sample. ImageJ was used to conduct FFT of each image. Then histograms were generated for each sample. No significant difference is apparent from the FFT histograms.

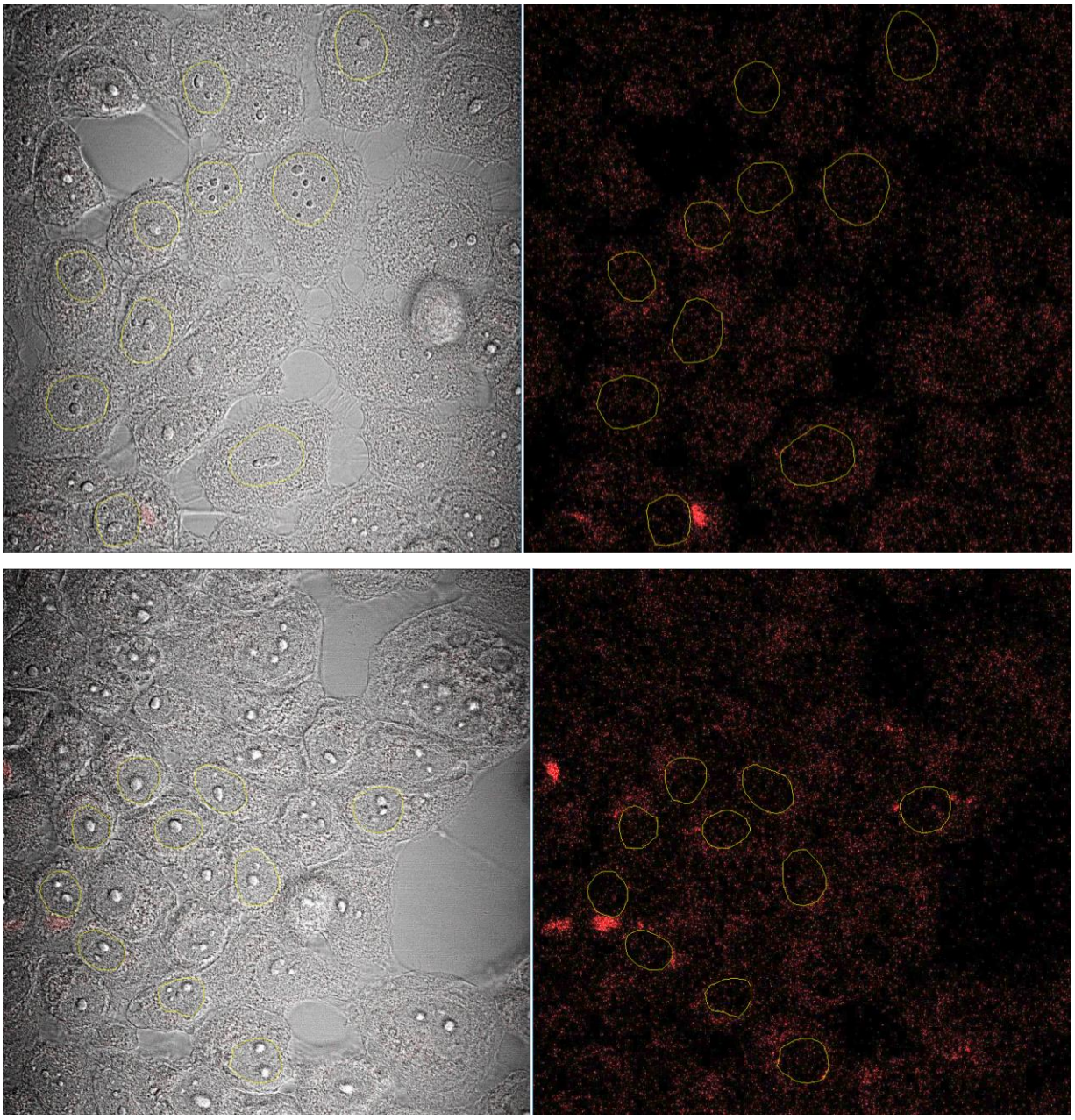

	Area (pixels^2)	Mean (A.U.)	Std. Dev. (A.U.)
RLNP	83099	11.822	22.304
Fol-RLNP	54803	12.796	21.722

Figure 3.S 9. *Intra-nuclear PPIX Intensities.* (Top) RLNP sample (Bottom) Fol-RLNP sample. In ImageJ, boundaries were manually drawn and mean pixel intensities were measured. The values are displayed in the table below the images above. Areas represent total area of all 10 nuclei analyzed for each sample and are measured in square pixels. The mean and standard deviation values are measured in arbitrary units of pixel intensity. No clear difference in intra-nuclear intensities were observed.

Hypothesis (4) was examined by performing a classical radiobiological assay comparing sub-lethal damage repair (SLDR) in HN31 cells treated with Fol-RLNPs, RLNPs, and PBS and subsequently irradiated with a split X-ray dose at various time intervals. The goal of this experiment was to determine if there was a substantial difference in SLDR kinetics or maximal repair for cells in each of the treatment groups, indicated by clonogenic survival of HN31 cells in each treatment category. The results are displayed in Figure 3.S10. As seen in the figure, the curve for each of the treatment groups is shifted from the others, consistent with the initial clonogenic efficacy data found in Figure 3.5 in the main text. However, the shapes of the curves (SLDR kinetics) and increase in survival (SLD maximal repair) observed indicated that there is little or no difference in SLDR for the treatment groups. From this, we concluded that SLDR differences could not explain the difference in efficacy between Fol-RLNP- and RLNP-treated cells.

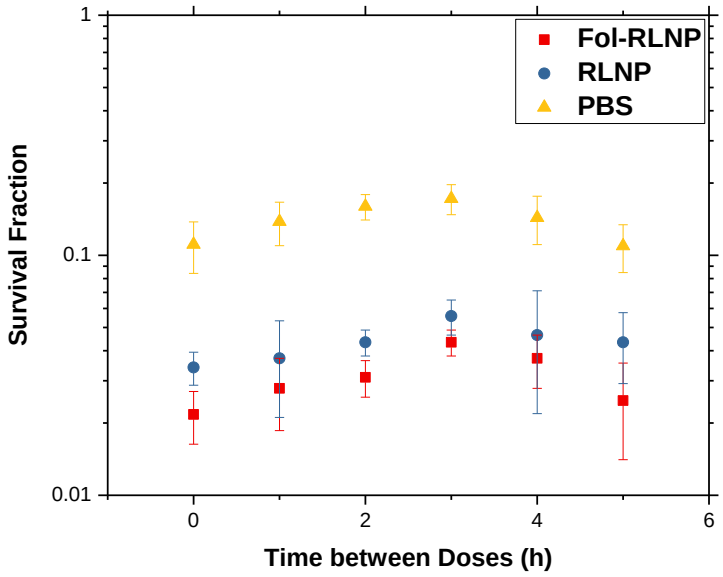

Figure 3.S 10. *Sub-lethal Damage Repair Measured by Clonogenic HN31 Survival after Split Dose X-ray*. HN31 cells were seeded in 6-well culture dishes at a density of 1.0 x 10^3 per well. After 4-hour incubation with PBS, RLNPs or Fol-RLNPs, cells were exposed to 2 doses of 2 Gy X-ray radiation separated by various times with a 320 keV X-ray irradiator at approximately 2 Gy/min. Irradiated cells were cultured for 14 days. Colonies of more than 50 daughter cells in culture were counted (N = 3 wells per group). Error bars represent standard deviations. Note: Experiment conducted using unfiltered particles.

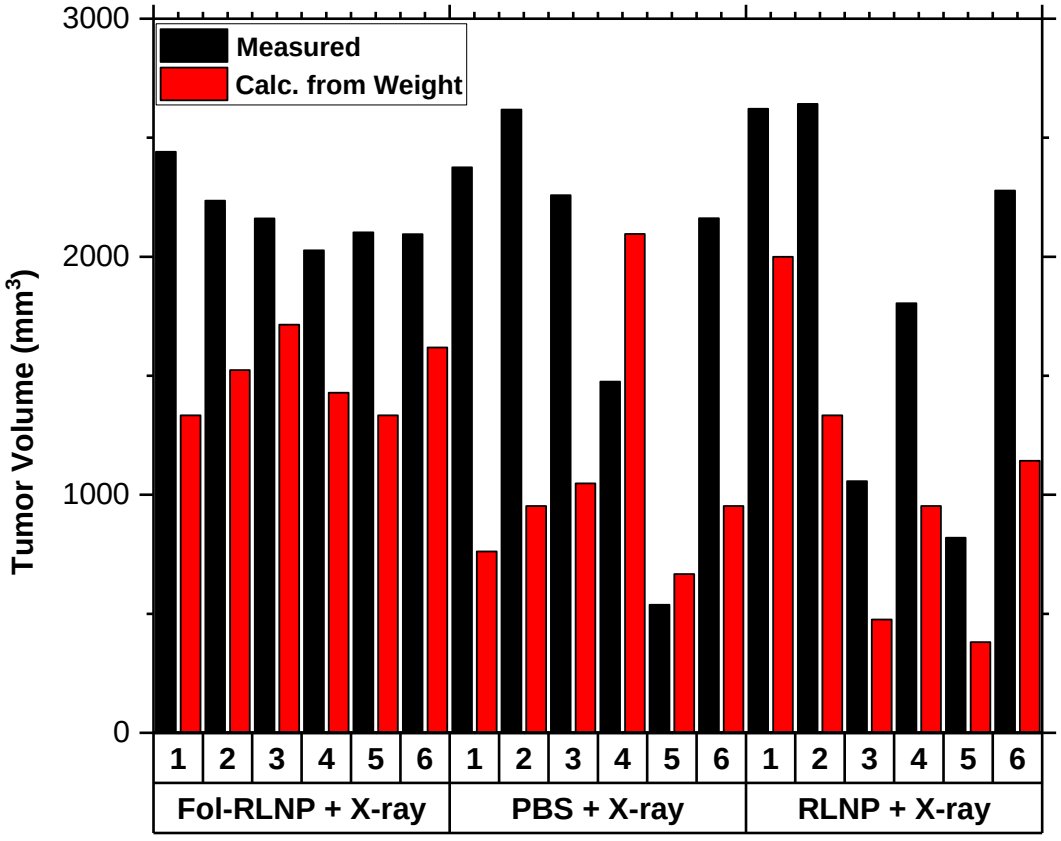

Figure 3.S 11. *Measured Tumor Volume vs. Weight-calculated Volume in Mouse Study.* In the mouse study reported, tumor volumes were measured with digital calipers for length (L) and width (W) in two dimensions. Volume was calculated as $V = (L \times W^2) \times \pi/6$. For tumor volume estimations from tumor weight, a density of 1.05 g/cc was used. Details of tumor volume calculations for the mouse study displayed in Figure 9 of the main text. The two-dimensional tumor measurements (with the assumption of ellipsoidal symmetry) overestimated the tumor volume considerably compared to weight-based estimates. The reason for this is the asymmetry of the tumors involved in these experiments. Some mice in the studies formed blisters on the tumor xenografts, which burst before euthanasia, and contributed to the discrepancy in tumor volume estimates due to the introduction of asymmetry caused by the apparent "larger" volume from the blister liquid.

APPENDIX B. SUPPLEMENTAL INFORMATION FOR CHAPTER 4

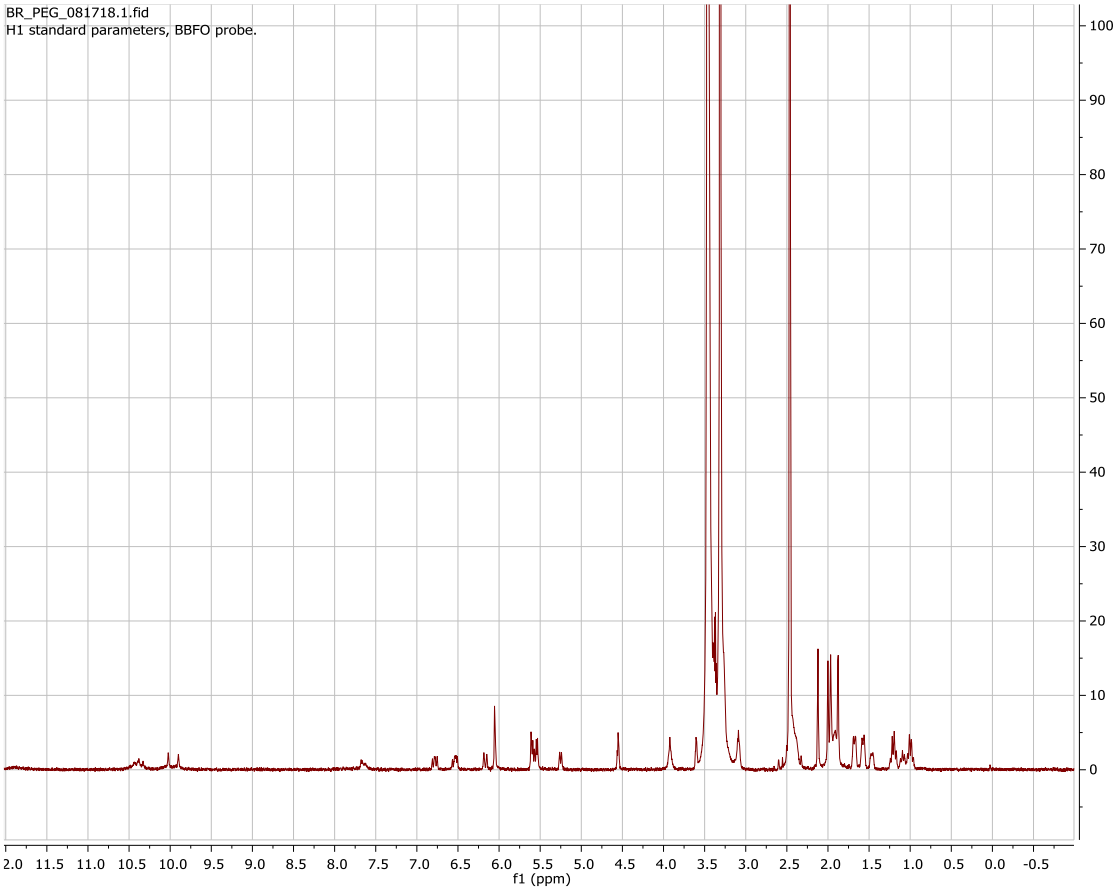

Figure 4.S 1. *^{1}H-NMR Spectrum of PEG-BR.* As-synthesized PEG-BR was dissolved in DMSO-d6 (5 mg/mL) and ^{1}H-NMR spectrum acquired. Note: peak at 2.5 ppm is DMSO-d6 and peak at 3.25 ppm is residual water. Spectrum confirms PEG and bilirubin molecules are present in final structure.

REFERENCES

1 Baskar, R., Yap, S. P., Chua, K. L. M. & Itahana, K. The diverse and complex roles of radiation on cancer treatment: therapeutic target and genome maintenance. *Am J Cancer Res* **2**, 372-382 (2012).

2 Sacco, A. G. & Cohen, E. E. Current Treatment Options for Recurrent or Metastatic Head and Neck Squamous Cell Carcinoma. *Journal of Clinical Oncology* **33**, 3305-3313, doi:10.1200/JCO.2015.62.0963 (2015).

3 Hall, E. J. & Giaccia, A. J. *Radiobiology for the radiologist*. (Wolters Kluwer Health/Lippincott Williams & Wilkins, 2012).

4 Wendt, T. G. *et al.* Simultaneous radiochemotherapy versus radiotherapy alone in advanced head and neck cancer: a randomized multicenter study. *Journal of Clinical Oncology* **16**, 1318-1324, doi:10.1200/JCO.1998.16.4.1318 (1998).

5 Chen, Y. *et al.* Phase I/II Clinical Study of Pulsed Paclitaxel Radiosensitization for Thoracic Malignancy. *Clinical Cancer Research* **9**, 969 (2003).

6 Bonvalot, S. *et al.* First-in-Human Study Testing a New Radioenhancer Using Nanoparticles (NBTXR3) Activated by Radiation Therapy in Patients with Locally Advanced Soft Tissue Sarcomas. *Clinical Cancer Research*, doi:10.1158/1078-0432.CCR-16-1297 (2016).

7 Willers, H., Dahm-Daphi, J. & Powell, S. N. Repair of radiation damage to DNA. *British Journal of Cancer* **90**, 1297-1301, doi:10.1038/sj.bjc.6601729 (2004).

8 Cohen–Jonathan, E., Bernhard, E. J. & McKenna, W. G. How does radiation kill cells? *Current Opinion in Chemical Biology* **3**, 77-83, doi:https://doi.org/10.1016/S1367-5931(99)80014-3 (1999).

9 Desouky, O., Ding, N. & Zhou, G. Targeted and non-targeted effects of ionizing radiation. *Journal of Radiation Research and Applied Sciences* **8**, 247-254, doi:https://doi.org/10.1016/j.jrras.2015.03.003 (2015).

10 Baskar, R., Lee, K. A., Yeo, R. & Yeoh, K.-W. Cancer and radiation therapy: current advances and future directions. *Int J Med Sci* **9**, 193-199, doi:10.7150/ijms.3635 (2012).

11 Haupt, S., Berger, M., Goldberg, Z. & Haupt, Y. Apoptosis - the p53 network. *Journal of Cell Science* **116**, 4077, doi:10.1242/jcs.00739 (2003).

12 van Hagen, P. *et al.* Preoperative Chemoradiotherapy for Esophageal or Junctional Cancer. *New England Journal of Medicine* **366**, 2074-2084, doi:10.1056/NEJMoa1112088 (2012).

13 DeAngelis, L. M., Seiferheld, W., Schold, S. C., Fisher, B. & Schultz, C. J. Combination Chemotherapy and Radiotherapy for Primary Central Nervous System Lymphoma: Radiation Therapy Oncology Group Study 93-10. *Journal of Clinical Oncology* **20**, 4643-4648, doi:10.1200/JCO.2002.11.013 (2002).

14 Miller, T. P. *et al.* Chemotherapy Alone Compared with Chemotherapy plus Radiotherapy for Localized Intermediate- and High-Grade Non-Hodgkin's Lymphoma. *New England Journal of Medicine* **339**, 21-26, doi:10.1056/NEJM199807023390104 (1998).

15 Pauwels, B., Korst, A. E. C., Lardon, F. & Vermorken, J. B. Combined Modality Therapy of Gemcitabine and Radiation. *The Oncologist* **10**, 34-51, doi:10.1634/theoncologist.10-1-34 (2005).

16 Lawrence, T. S., Blackstock, A. W. & McGinn, C. The mechanism of action of radiosensitization of conventional chemotherapeutic agents. *Seminars in Radiation Oncology* **13**, 13-21, doi:https://doi.org/10.1053/srao.2003.50002 (2003).

17 Adam, J. K., Odhav, B. & Bhoola, K. D. Immune responses in cancer. *Pharmacology & Therapeutics* **99**, 113-132, doi:https://doi.org/10.1016/S0163-7258(03)00056-1 (2003).

18 Zhang, H. & Chen, J. Current status and future directions of cancer immunotherapy. *J Cancer* **9**, 1773-1781, doi:10.7150/jca.24577 (2018).

19 Walle, T. *et al.* Radiation effects on antitumor immune responses: current perspectives and challenges. *Ther Adv Med Oncol* **10**, 1758834017742575-1758834017742575, doi:10.1177/1758834017742575 (2018).

20 Baptista, M. S. *et al.* Type I and Type II Photosensitized Oxidation Reactions: Guidelines and Mechanistic Pathways. *Photochemistry and Photobiology* **93**, 912-919, doi:10.1111/php.12716 (2017).

21 Foote, C. S. in *Light-Activated Pesticides* Vol. 339 *ACS Symposium Series* Ch. 2, 22-38 (American Chemical Society, 1987).

22 Mroz, P., Yaroslavsky, A., Kharkwal, G. B. & Hamblin, M. R. Cell death pathways in photodynamic therapy of cancer. *Cancers (Basel)* **3**, 2516-2539, doi:10.3390/cancers3022516 (2011).

23 Rastogi, R. P., Richa, Kumar, A., Tyagi, M. B. & Sinha, R. P. Molecular Mechanisms of Ultraviolet Radiation-Induced DNA Damage and Repair. *Journal of Nucleic Acids* **2010**, doi:10.4061/2010/592980 (2010).

24 Batista, L. F. Z., Kaina, B., Meneghini, R. & Menck, C. F. M. How DNA lesions are turned into powerful killing structures: Insights from UV-induced apoptosis. *Mutation Research/Reviews in Mutation Research* **681**, 197-208, doi:https://doi.org/10.1016/j.mrrev.2008.09.001 (2009).

25 Mehanna, H., Paleri, V., West, C. M. L. & Nutting, C. Head and neck cancer—Part 1: Epidemiology, presentation, and prevention. *BMJ* **341**, c4684, doi:10.1136/bmj.c4684 (2010).

26 Oksuz, D. C. *et al.* Recurrence patterns of locally advanced head and neck squamous cell carcinoma after 3D conformal (chemo)-radiotherapy. *Radiat Oncol* **6**, 54-54, doi:10.1186/1748-717X-6-54 (2011).

27 Lefebvre, J.-L. *et al.* Larynx Preservation in Pyriform Sinus Cancer: Preliminary Results of a European Organization for Research and Treatment of Cancer Phase III Trial. *JNCI: Journal of the National Cancer Institute* **88**, 890-899, doi:10.1093/jnci/88.13.890 (1996).

28 Tobias, J. S. *et al.* Chemoradiotherapy for locally advanced head and neck cancer: 10-year follow-up of the UK Head and Neck (UKHAN1) trial. *Lancet Oncol* **11**, 66-74, doi:10.1016/S1470-2045(09)70306-7 (2009).

29 Trotti, A. Toxicity in head and neck cancer: a review of trends and issues. *International Journal of Radiation Oncology*Biology*Physics* **47**, 1-12, doi:https://doi.org/10.1016/S0360-3016(99)00558-1 (2000).

30 Wang, G. D. *et al.* X-Ray Induced Photodynamic Therapy: A Combination of Radiotherapy and Photodynamic Therapy. *Theranostics* **6**, 2295-2305, doi:10.7150/thno.16141 (2016).

31 Bulin, A.-L., Broekgaarden, M., Simeone, D. & Hasan, T. Low dose photodynamic therapy harmonizes with radiation therapy to induce beneficial effects on pancreatic heterocellular spheroids. *Oncotarget* **10**, 2625-2643, doi:10.18632/oncotarget.26780 (2019).

32 Civantos, F. J. *et al.* A Review of Photodynamic Therapy for Neoplasms of the Head and Neck. *Advances in Therapy* **35**, 324-340, doi:10.1007/s12325-018-0659-3 (2018).

33 Nakano, A. *et al.* Treatment efficiency of combining photodynamic therapy and ionizing radiation for Bowen's disease. *Journal of the European Academy of Dermatology and Venereology* **25**, 475-478, doi:10.1111/j.1468-3083.2010.03757.x (2011).

34 Freitag, L. *et al.* Sequential photodynamic therapy (PDT) and high dose brachytherapy for endobronchial tumour control in patients with limited bronchogenic carcinoma. *Thorax* **59**, 790, doi:10.1136/thx.2003.013599 (2004).

35 Allison, R. R. & Moghissi, K. Photodynamic Therapy (PDT): PDT Mechanisms. *Clin Endosc* **46**, 24-29, doi:10.5946/ce.2013.46.1.24 (2013).

36 Kwatra, D., Venugopal, A. & Anant, S. Nanoparticles in radiation therapy: a summary of various approaches to enhance radiosensitization in cancer. *Translational Cancer Research* **2**, 330-342 (2013).

37 Xie, J. *et al.* Emerging Strategies of Nanomaterial-Mediated Tumor Radiosensitization. *Advanced Materials* **31**, 1802244, doi:10.1002/adma.201802244 (2019).

38 Chen, H. *et al.* Nanoscintillator-mediated X-ray inducible photodynamic therapy for in vivo cancer treatment. *Nano Lett* **15**, 2249-2256, doi:10.1021/nl504044p (2015).

39 Marill, J. *et al.* Hafnium oxide nanoparticles: toward an in vitro predictive biological effect? *Radiat Oncol* **9**, 150-150, doi:10.1186/1748-717X-9-150 (2014).

40 Nanobiotix. *Nanobiotix - Clinical Research*, <https://www.nanobiotix.com/_en/clinical-research/> (2019).

41 Maggiorella, L. *et al.* Nanoscale radiotherapy with hafnium oxide nanoparticles. *Future Oncology* **8**, 1167-1181, doi:10.2217/fon.12.96 (2012).

42 Hirano, S. & Suzuki, K. T. Exposure, metabolism, and toxicity of rare earths and related compounds. *Environ Health Perspect* **104 Suppl 1**, 85-95, doi:10.1289/ehp.96104s185 (1996).

43 Oksuz, D. C. *et al.* Recurrence patterns of locally advanced head and neck squamous cell carcinoma after 3D conformal (chemo)-radiotherapy. *Radiation Oncology* **6**, 54, doi:10.1186/1748-717x-6-54 (2011).

44 Begg, A. C. Predicting Recurrence After Radiotherapy in Head and Neck Cancer. *Seminars in Radiation Oncology* **22**, 108-118, doi:http://dx.doi.org/10.1016/j.semradonc.2011.12.002 (2012).

45 Matoscevic, K., Graf, N., Pezier, T. F. & Huber, G. F. Success of Salvage Treatment. *Otolaryngology–Head and Neck Surgery* **151**, 454-461, doi:10.1177/0194599814535183 (2014).

46 Vermorken, J. B. Head and neck cancer: Medical treatment in head and neck cancer. *Annals of Oncology* **16**, ii258-ii264, doi:10.1093/annonc/mdi735 (2005).

47 Barnett, G. C. *et al.* Normal tissue reactions to radiotherapy: towards tailoring treatment dose by genotype. *Nature reviews. Cancer* **9**, 134-142, doi:10.1038/nrc2587 (2009).

48 Koch, C. J., Parliament, M. B., Brown, J. M. & Urtasun, R. C. in *Leibel and Phillips Textbook of Radiation Oncology (Third Edition)* (eds Theodore Locke Phillips & Mack Roach) 55-68 (Content Repository Only!, 2010).

49 Kamkaew, A., Chen, F., Zhan, Y., Majewski, R. L. & Cai, W. Scintillating Nanoparticles as Energy Mediators for Enhanced Photodynamic Therapy. *ACS nano* **10**, 3918-3935, doi:10.1021/acsnano.6b01401 (2016).

50 Ormond, B. A. & Freeman, S. H. Dye Sensitizers for Photodynamic Therapy. *Materials* **6**, doi:10.3390/ma6030817 (2013).

51 Jo, S. D. *et al.* PEG–PLA-Coated and Uncoated Radio-Luminescent CaWO4 Micro- and Nanoparticles for Concomitant Radiation and UV-A/Radio-Enhancement Cancer Treatments. *ACS Biomaterials Science & Engineering* **4**, 1445-1462, doi:10.1021/acsbiomaterials.8b00119 (2018).

52 Panich, U., Sittithumcharee, G., Rathviboon, N. & Jirawatnotai, S. Ultraviolet Radiation-Induced Skin Aging: The Role of DNA Damage and Oxidative Stress in Epidermal Stem Cell Damage Mediated Skin Aging. *Stem Cells International* **2016**, 7370642, doi:10.1155/2016/7370642 (2016).

53 Lim, C.-K. *et al.* Nanophotosensitizers toward advanced photodynamic therapy of Cancer. *Cancer Letters* **334**, 176-187, doi:http://dx.doi.org/10.1016/j.canlet.2012.09.012 (2013).

54 Low, P. S. & Antony, A. C. Folate receptor-targeted drugs for cancer and inflammatory diseases. *Advanced Drug Delivery Reviews* **56**, 1055-1058, doi:http://dx.doi.org/10.1016/j.addr.2004.02.003 (2004).

55 Toffoli, G. *et al.* Overexpression of folate binding protein in ovarian cancers. *International Journal of Cancer* **74**, 193-198, doi:10.1002/(SICI)1097-0215(19970422)74:2<193::AID-IJC10>3.0.CO;2-F (1997).

56 Elnakat, H. & Ratnam, M. Distribution, functionality and gene regulation of folate receptor isoforms: implications in targeted therapy. *Advanced Drug Delivery Reviews* **56**, 1067-1084, doi:http://dx.doi.org/10.1016/j.addr.2004.01.001 (2004).

57 Hansen, M. F. *et al.* Folic acid mediates activation of the pro-oncogene STAT3 via the Folate Receptor alpha. *Cellular Signalling* **27**, 1356-1368, doi:https://doi.org/10.1016/j.cellsig.2015.03.020 (2015).

58 Cheung, A. *et al.* Targeting folate receptor alpha for cancer treatment. *Oncotarget* **7**, 52553-52574, doi:10.18632/oncotarget.9651 (2016).

59 Lalami, Y. *et al.* EORTC 24051: Unexpected side effects in a phase I study of TPF induction chemotherapy followed by chemoradiation with lapatinib, a dual EGFR/ErbB2 inhibitor, in patients with locally advanced resectable larynx and hypopharynx squamous cell carcinoma. *Radiotherapy and Oncology* **105**, 238-240, doi:http://dx.doi.org/10.1016/j.radonc.2012.08.006 (2012).

60 Lee, J., Rancilio, N. J., Poulson, J. M. & Won, Y.-Y. Block Copolymer-Encapsulated CaWO4 Nanoparticles: Synthesis, Formulation, and Characterization. *ACS Applied Materials & Interfaces* **8**, 8608-8619, doi:10.1021/acsami.6b00727 (2016).

61 Sherck, N. J., Kim, H. C. & Won, Y.-Y. Elucidating a Unified Mechanistic Scheme for the DBU-Catalyzed Ring-Opening Polymerization of Lactide to Poly(lactic acid). *Macromolecules* **49**, 4699-4713, doi:10.1021/acs.macromol.6b00621 (2016).

62 Xiong, J. *et al.* Folate-conjugated crosslinked biodegradable micelles for receptor-mediated delivery of paclitaxel. *Journal of Materials Chemistry* **21**, 5786-5794, doi:10.1039/C0JM04410E (2011).

63 Bolte, S. & CordeliÈRes, F. P. A guided tour into subcellular colocalization analysis in light microscopy. *Journal of Microscopy* **224**, 213-232, doi:10.1111/j.1365-2818.2006.01706.x (2006).

64 Ash, C., Dubec, M., Donne, K. & Bashford, T. Effect of wavelength and beam width on penetration in light-tissue interaction using computational methods. *Lasers in Medical Science* **32**, 1909-1918, doi:10.1007/s10103-017-2317-4 (2017).

65 Sung Duk Jo, J. L., Min Kyung Joo, Vincenzo J. Pizzuti,Nicholas J. Sherck, Slgi Choi, Beom Suk Lee, Sung Ho Yeom, Sang Yoon Kim, Sun Hwa Kim, Ick Chan Kwon , You-Yeon Won. PEG–PLA-Coated and Uncoated Radio-Luminescent CaWO4 Micro- and Nanoparticles for Concomitant Radiation and UV-A/Radio-Enhancement Cancer Treatments. *ACS Biomaterials Science & Engineering* **4**, 1445-1462 (2018).

66 Greinert, R. *et al.* UVA-induced DNA double-strand breaks result from the repair of clustered oxidative DNA damages. *Nucleic Acids Res* **40**, 10263-10273, doi:10.1093/nar/gks824 (2012).

67 Tang, D. *et al.* ERK Activation Mediates Cell Cycle Arrest and Apoptosis after DNA Damage Independently of p53. *Journal of Biological Chemistry* **277**, 12710-12717, doi:10.1074/jbc.M111598200 (2002).

68 Nakamura, A. J., Rao, V. A., Pommier, Y. & Bonner, W. M. The complexity of phosphorylated H2AX foci formation and DNA repair assembly at DNA double-strand breaks. *Cell Cycle* **9**, 389-397, doi:10.4161/cc.9.2.10475 (2010).

69 Misra, R. *et al.* Radioluminescent nanoparticles for radiation-controlled release of drugs. *Journal of Controlled Release* **303**, 237-252, doi:https://doi.org/10.1016/j.jconrel.2019.04.033 (2019).

70 Plavec, T., Kessler, M., Kandel, B., Schwietzer, A. & Roleff, S. Palliative radiotherapy as treatment for non-resectable soft tissue sarcomas in the dog – a report of 15 cases. *Veterinary and Comparative Oncology* **4**, 98-103, doi:10.1111/j.1476-5810.2006.00097.x (2006).

71 Stocker, R., Yamamoto, Y., McDonagh, A. F., Glazer, A. N. & Ames, B. N. Bilirubin is an antioxidant of possible physiological importance. *Science* **235**, 1043, doi:10.1126/science.3029864 (1987).

72 Deziel, M. R. & Girotti, A. W. Photodynamic action of bilirubin on liposomes and erythrocyte membranes. *Journal of Biological Chemistry* **255**, 8192-8198 (1980).

73 Zhou, X. F., Chen, F. Y., Zeng, Z. C. & Zheng, R. L. Photosensitization of bilirubin on proliferation and DNA synthesis in ascitic hepatoma cells. *Zhongguo yao li xue bao = Acta pharmacologica Sinica* **17**, 164-166 (1996).

74 Jarvi, M. T., Patterson, M. S. & Wilson, B. C. Insights into photodynamic therapy dosimetry: simultaneous singlet oxygen luminescence and photosensitizer photobleaching measurements. *Biophysical journal* **102**, 661-671, doi:10.1016/j.bpj.2011.12.043 (2012).

75 Dolmans, D. E. J. G. J., Fukumura, D. & Jain, R. K. Photodynamic therapy for cancer. *Nat Rev Cancer* **3**, 380-387 (2003).

76 Brown, S. B., Brown, E. A. & Walker, I. The present and future role of photodynamic therapy in cancer treatment. *The Lancet Oncology* **5**, 497-508, doi:http://dx.doi.org/10.1016/S1470-2045(04)01529-3 (2004).

77 Lovell, J. F., Liu, T. W. B., Chen, J. & Zheng, G. Activatable Photosensitizers for Imaging and Therapy. *Chemical Reviews* **110**, 2839-2857, doi:10.1021/cr900236h (2010).

78 Brian, C. W. & Michael, S. P. The physics, biophysics and technology of photodynamic therapy. *Physics in Medicine & Biology* **53**, R61 (2008).

79 van Straten, D., Mashayekhi, V., de Bruijn, H. S., Oliveira, S. & Robinson, D. J. Oncologic Photodynamic Therapy: Basic Principles, Current Clinical Status and Future Directions. *Cancers* **9**, 19, doi:10.3390/cancers9020019 (2017).

80 Agostinis, P. *et al.* PHOTODYNAMIC THERAPY OF CANCER: AN UPDATE. *CA: a cancer journal for clinicians* **61**, 250-281, doi:10.3322/caac.20114 (2011).

81 Yano, T. *et al.* Photodynamic therapy as salvage treatment for local failure after chemoradiotherapy in patients with esophageal squamous cell carcinoma: A phase II study. *International Journal of Cancer* **131**, 1228-1234, doi:10.1002/ijc.27320 (2012).

82 Kostron, H., Swartz, M. R., Miller, D. C. & Martuza, R. L. The interaction of hematoporphyrin derivative, light, and ionizing radiation in a rat glioma model. *Cancer* **57**, 964-970, doi:10.1002/1097-0142(19860301)57:5<964::AID-CNCR2820570515>3.0.CO;2-S (1986).

83 Sazgarnia, A., Montazerabadi, A. R., Bahreyni-Toosi, M. H., Ahmadi, A. & Aledavood, A. In vitro survival of MCF-7 breast cancer cells following combined treatment with ionizing radiation and mitoxantrone-mediated photodynamic therapy. *Photodiagnosis and Photodynamic Therapy* **10**, 72-78, doi:http://dx.doi.org/10.1016/j.pdpdt.2012.06.001 (2013).

84 Frame, F. M. *et al.* Mechanisms of growth inhibition of primary prostate epithelial cells following gamma irradiation or photodynamic therapy include senescence, necrosis, and autophagy, but not apoptosis. *Cancer Medicine* **5**, 61-73, doi:10.1002/cam4.553 (2016).

85 Lee, Y. *et al.* Multistimuli-Responsive Bilirubin Nanoparticles for Anticancer Therapy. *Angewandte Chemie International Edition* **55**, 10676-10680, doi:doi:10.1002/anie.201604858 (2016).

86 Sang Yong Jon, Y. H. L. BILIRUBIN NANOPARTICLE, USE THEREOF, AND PREPARATION METHOD THEREFOR. United States patent (2017).

87 Yun Dong Lee, S. Y. J., Yong Hyun Lee, Do Hyun Yoo, Won Sik Jung. Particles Comprising Bilirubin Derivative and Metal. (2018).

88 Lee, J., Rancilio, N., Poulson, J. & Won, Y. Block Copolymer-Encapsulated CaWO4 Nanoparticles: Synthesis, Formulation, and Characterization. *Acs Applied Materials & Interfaces* **8**, 8608-8619, doi:10.1021/acsami.6b00727 (2016).

89 Franken, N. A. P., Rodermond, H. M., Stap, J., Haveman, J. & van Bree, C. Clonogenic assay of cells in vitro. *Nature Protocols* **1**, 2315, doi:10.1038/nprot.2006.339 (2006).

90 Vincenzo J. Pizzuti , R. M., Jaewon Lee , Sandra E. Torregrosa-Allen, Melanie P.Currie,Scott R. Clark , Anish P. Patel , Christopher R. Schorr, Yava Jones-Hall, Michael O.Childress, Jeannie M. Plantenga , Nicholas J. Rancilio , Bennett D. Elzey ,You-YeonWon. *Folic Acid-Conjugated Radio-Luminescent Calcium Tungstate Nanoparticles as Radio-Sensitizers for Cancer Radiotherapy* (2018).

91 Goel, S., Ni, D. & Cai, W. Harnessing the Power of Nanotechnology for Enhanced Radiation Therapy. *ACS Nano* **11**, 5233-5237, doi:10.1021/acsnano.7b03675 (2017).

92 Wang, H., Mu, X., He, H. & Zhang, X.-D. Cancer Radiosensitizers. *Trends in Pharmacological Sciences* **39**, 24-48, doi:https://doi.org/10.1016/j.tips.2017.11.003 (2018).

93 Huang, F., Dempsey, C., Chona, D. & Suh, J. Quantitative nanoparticle tracking: applications to nanomedicine. *Nanomedicine (Lond)* **6**, 693-700, doi:10.2217/nnm.11.42 (2011).

94 Durymanov, M. O., Rosenkranz, A. A. & Sobolev, A. S. Current Approaches for Improving Intratumoral Accumulation and Distribution of Nanomedicines. *Theranostics* **5**, 1007-1020, doi:10.7150/thno.11742 (2015).

95 Gao, Y. *et al.* Predictive models of diffusive nanoparticle transport in 3-dimensional tumor cell spheroids. *AAPS J* **15**, 816-831, doi:10.1208/s12248-013-9478-2 (2013).

96 Bailey, L. B. *et al.* Biomarkers of Nutrition for Development—Folate Review. *The Journal of Nutrition* **145**, 1636S-1680S, doi:10.3945/jn.114.206599 (2015).

97 Laftah, A. H. *et al.* Haem and folate transport by proton-coupled folate transporter/haem carrier protein 1 (SLC46A1). *British Journal of Nutrition* **101**, 1150-1156, doi:10.1017/S0007114508066762 (2008).

98 Oppenheim, E. W., Adelman, C., Liu, X. & Stover, P. J. Heavy Chain Ferritin Enhances Serine Hydroxymethyltransferase Expression and de Novo Thymidine Biosynthesis. *Journal of Biological Chemistry* **276**, 19855-19861, doi:10.1074/jbc.M100039200 (2001).

99 Woeller, C. F., Fox, J. T., Perry, C. & Stover, P. J. A Ferritin-responsive Internal Ribosome Entry Site Regulates Folate Metabolism. *Journal of Biological Chemistry* **282**, 29927-29935, doi:10.1074/jbc.M706264200 (2007).

100 Berlin, N. I., Neuberger, A. & Scott, J. J. The metabolism of δ-aminolaevulic acid. 1. Normal pathways, studied with the aid of ¹⁵N. *Biochemical Journal* **64**, 80-90, doi:10.1042/bj0640080 (1956).

101 Berlin, N. I., Neuberger, A. & Scott, J. J. The metabolism of δ-aminolaevulic acid. 2. Normal pathways, studied with the aid of ¹⁴C. *Biochemical Journal* **64**, 90-100, doi:10.1042/bj0640090 (1956).